Università degli Studi di Padova

Dipartimento di Fisica e Astronomia ‘Galileo Galilei’

Corso di Laurea Magistrale in Fisica

OPERATIONAL LIMITS AND DISRUPTIONS IN RFX-MOD

Supervisor:
Dott. Tommaso Bolzonella

Candidate:
Matteo Vallar
1079188

Anno Accademico 2014-2015

Alla mia famiglia

Abstract

This work can be framed in the purview of hot plasma magnetically confined in the configuration called Reversed Field Pinch. This configuration shares some physical aspects with astrophysical plasma phenomena, such as the solar flares. The common element that lies behind these two systems is the magnetic relaxation, which allows the plasma to reach a more favourable state in terms of energy minimisation.

In the tokamak magnetic configuration for plasma confinement a phenomenon called *disruption* has been interpreted as a critical relaxation event that tends to reorganise the magnetic configuration in order to reach the minimum energy state but instead leads the plasma to a sudden loss of confinement and current. In the Reversed Field Pinch, phenomena similar to disruptions, called *fast terminations*, have been recently recorded but never systematically analysed.

In this thesis, the phenomenology of fast terminations in the Reversed Field Pinch configuration is systematically studied for the first time in the RFX-mod device. Some particular disruptive discharges are presented and typical quench times, magnetic instability behaviour and some statistical analysis are shown. The main operational parameters bounded by disruptions are investigated. Finally, an analysis of the halo currents in a RFX-mod Reversed Field Pinch disruption is presented.

Keywords: plasma, fusion, RFP, tokamak, disruption, fast termination, halo currents

Sommario

Il lavoro presentato in questa tesi riguarda l'ambito dei plasmi caldi confinati magneticamente nella configurazione *Reversed Field Pinch*. In queste condizioni, il plasma ha dei comportamenti che assomigliano ad alcuni fenomeni astrofisici, come le eruzioni solari. L'elemento che accomuna questi due sistemi è il rilassamento magnetico, che permette al plasma di raggiungere uno stato più favorevole in termini di minimizzazione dell'energia.

Nella configurazione magnetica denominata *tokamak* un evento chiamato *disruption* è stato interpretato come un fenomeno critico di rilassamento che cerca di riorganizzare la configurazione magnetica per raggiungere la minima energia ma invece porta il plasma a un'improvvisa perdita di confinamento e di corrente. Nel *Reversed Field Pinch* dei fenomeni simili alle *disruptions*, chiamati *fast terminations* sono stati recentemente osservati ma mai analizzati in modo sistematico.

In questa tesi, la fenomenologia delle *fast terminations* nel *Reversed Field Pinch* è studiata sistematicamente per la prima volta nell'esperimento RFX-mod. Alcune scariche disruttive sono state analizzate e sono mostrati i tipici tempi di sviluppo del fenomeno, il comportamento delle instabilità magnetiche e alcune analisi statistiche. I principali parametri operativi sono studiati per vedere i limiti oltre i quali si sviluppa una *fast termination*. Infine viene presentata un'analisi delle correnti di *halo* generate dalle *fast terminations* in RFX-mod.

Keywords: plasma, fusione, RFP, tokamak, disruption, terminazione veloce, correnti di halo

Acknowledgements

This thesis would not have been possible without the presence of many people in my life.

First of all, I want to thank my family for their long and unconditioned support, for giving me the possibility and opportunity to be free and make independently my choices. This work and what I will do in my future won't have been possible without you.

I wish to thank my supervisor Tommaso Bolzonella for the kindness and willingness he had in guiding me during this thesis and in going beyond the difficulties I met. I am grateful for the suggestions and hints he gave me and for the humanity and the respect he reserves me and to the people he works with.

I have been very lucky doing the thesis at the Consorzio RFX for the people I had the opportunity to know. I want to thank Paolo F., Gianluca S., Fulvio A., Paolo I., Cesare T., Luisa M. for the technical support and the interesting and useful things you taught me. My presence at RFX would have not had the same flavour without the people I shared the office with, I laughed with and I ate with: thank you all Leonardo, Matteo, Nisarg, Daniele, Pietro, Oisín, Ondrej, TJ, Yhang, Marco B., Marco G., Marco M., Carlo, Nicolò, Vadim!

There are some people I met in my life that gave me the most deep and trustful friendship I could ever get. I say thank you to the people from Maniago, who made me feel home every time I returned and they supported me with their sincere interest and our funny free time.

In Padova I found people that made my second family. I would really to thank all the people from the Collegio don Nicola Mazza, where I found a formative environment which helped me being a better person and students like me that taught me the best way to pass over all the difficulties. I would in particular thank all the 'Secondo Piano' for our study sessions, our meals and all the moments we enjoyed together.

Last but the most important, I would thank the person who taught me what love is, where we can find the best of ourselves and how to truly help the people around us. Thank you for everything, Denise.

Matteo Vallar

Contents

List of Figures

'Io stimo più il trovar un vero, benché di cosa leggiera, che 'l disputar lungamente delle massime questioni senza conseguir verità nissuna.'

G. Galilei

Introduction

The lack of energy is a problem that humanity could face in a century from now due to the exhaustion of the fossil fuels that granted the evolution of the present human lifestyle.

A resource that could be able to solve this problem is nuclear fusion, the phenomenon opposed to nuclear fission, that can produce energy by merging two light nuclei. At present, fusion can't be used for electric power generation but there are studies devoted to find a way to exploit it in this way.

Hot plasmas ($T \approx 10^7\,\mathrm{K}$) can be confined with strong magnetic fields in order to study their behaviour and capability to produce energy through nuclear fusion.

The tokamak is a magnetoplasma configuration deeply studied since the late '50s thanks to its applicability to controlled thermonuclear fusion. A *disruption* is a fast and sudden loss of thermal energy (called thermal quench TQ) and current (current quench CQ) that can occur in the tokamak. This loss is also associated with the appearance of plasma instabilities that can be framed in the magneto-hydrodynamic (MHD) model. In the tokamak, this phenomenon has been widely studied but a full comprehension has still to be achieved. The importance of studying disruptions has two aspects: first, disruptions can be harmful for the device because of the high heat fluxes, electric currents and high mechanical forces (due to the coupling of magnetic fields with the induced currents) which stress the mechanical structure; second, they are due to a combination of several physical phenomena which have not a full theoretical comprehension and thus need further studies in terms of characterisation, prediction and avoidance. In addiction to that, when the plasma hits the wall, part of the plasma current can flow through the support structure, generating the so-called halo currents that can be harmful for the device. Tokamak operational limits have been found in terms of global plasma parameters, such as the safety factor q, the β parameter and the density. When one of those limits is overpassed, the instabilities triggering the disruption appear and hence a sudden confinement loss happens.

The Reversed Field Pinch (RFP) is another magnetic configuration studied to confine hot plasmas and in this case disruptions have not been seen although sudden losses of confinement may occasionally happen. This phenomenon is often called *fast termination* (FT). The density operational space has been explored in the RFP, but a defined limit (as the ones mentioned above for the tokamak) couldn't be found. The main objective of the thesis is to perform a systematic analysis of FT in RFX-mod (Major radius $R_0 = 2\,\mathrm{m}$, minor radius $a = 0.46\,\mathrm{m}$, maximum plasma current $I_{max} = 2\,\mathrm{MA}$) at present the largest RFP facility in operation.

Tokamak disruptions and RFP FT could be linked because of the underlying physics: in the tokamak, a disruption can be seen as a dramatic relaxation event and in the RFP such relaxation events are at the basis of the sustainment of the configuration itself.

The thesis will be developed in the structure that follows.

In ***Chapter 1***, an overview of the methods used for thermonuclear fusion is given, in order to introduce the RFP and the physical mechanism that allows it to survive for times longer than the resistive decay time. The dynamo action and its application to the RFP is studied and an explanation of the relaxation process is given, studying in detail the energy redistribution between the magnetic fluctuation modes that allow the magnetic field to reverse. In the end, the RFX-mod experiment is presented in its general features.

After presenting the RFP behaviour, in ***Chapter 2*** tokamak disruptions are shown, describing the operational limits, the typical phases and time scales over which they develop and the effects they have on the devices. In the end the density limit for the RFP is briefly analysed.

Chapter 3 is devoted to study the diagnostics used in RFX-mod. The limits and the physical principles are studied, in order to describe how the plasma is controlled and to highlight the technical challenges of diagnostic measurements during a FT.

After this first review part, the original part of the work is presented. In ***Chapter 4***, using the framework and the behaviour of disruptions in tokamaks as reference, the FT in the RFP is characterised and studied. Critical aspects in doing an automatic analysis and creating a FT database are presented, along with the method to find this particular shots. Some discharges are studied in detail in order to highlight reproducible features of RFP FT. In order to do that, the behaviour of some critical quantities (e.g. plasma density, average magnetic parameters, 2D Fourier spectrum of magnetic fluctuations) are studied.

In ***Chapter 5***, a statistical analysis has been carried out over a database of more than 330 discharges, finding correlations between different parameters, in particular regarding the times over which a disruption develops. An interesting trend has been found regarding the thermal quench time and the current quench time, opposite with respect to the tokamak. The MHD activity has also been studied, in particular considering the magnetic modes, their interaction and the macroscopic effect that they can have on the plasma discharge. The path that some physical quantities of the discharges follow in the operational space has been studied, in order to find if there are some limits that should not be overpassed for the sustainment of the discharge.

Lastly, in ***Chapter 6*** halo currents have been analysed as a consequence of a RFP FT in RFX-mod. Their magnitude distribution in the poloidal section at fixed toroidal angles and the correlation that these quantities have with the position of the phase locking of the MHD magnetic modes have been studied. In the end, the toroidal peaking factor and the halo fraction have been defined and studied also for RFX-mod.

1

Controlled thermonuclear fusion and magnetic confinement

In this chapter an overview of the current nuclear fusion scenario is given, with an explanation of its basic principles and its advantages compared to other energy sources. The methods to achieve controlled nuclear fusion will be discussed, focusing on the magnetic confinement and the two main *pinch* configuration at present developed. Finally, the basic physic principles of the Reversed Field Pinch and the RFX-mod experiment will be presented.

1.1 Nuclear fusion

In the last century the structure of the nucleus has been discovered, analysed and characterised. Since that time, scientists have applied their knowledge about the nucleus in order to improve the human lifestyle. In particular, nuclear fission has been widely used to produce electrical energy and it still is. This is possible because there is a difference between the mass of the nucleus and the mass of its components, due to the binding energy. The total rest mass of a nucleus obeys the following formula:

$$M({}^{A}_{Z}X) = ZM_p + (A - Z)M_n - \chi \tag{1.1}$$

where M is the mass, A the mass number, Z the atomic number, the pedices p and n indicate the proton and the neutron and χ is the binding energy of the nucleus. The binding energy is due not to electromagnetic fields, but it's the result of the strong force acting between neutrons and protons. It's not equal for each nucleus, in fact it follows the trend shown in figure 1.1.

By moving to the mass number of 60 we can see that the binding energy χ per nucleon increases. This means that if we make a reaction using as reagent nuclei that are further than the products from the maximum of χ, we have an exothermic

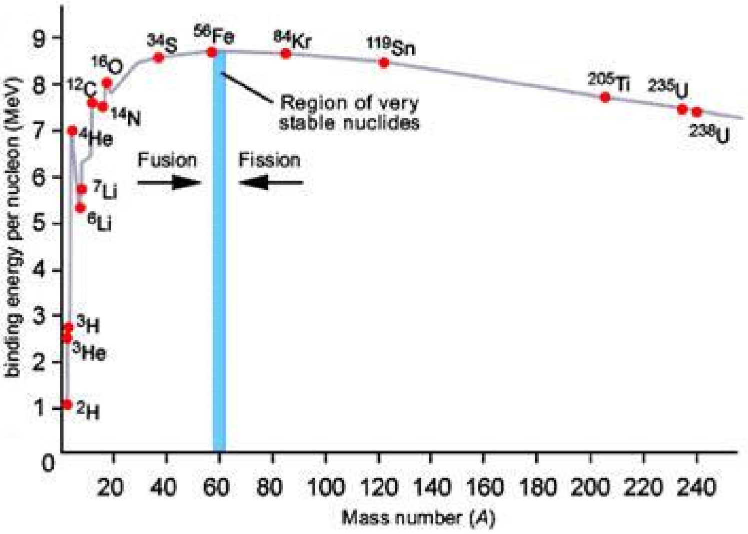

Figure 1.1: Trend of the average binding energy per nucleon as function of the mass number

reaction and hence an energy gain. One of such reactions moving from right to left is called *fission* while the one moving in the other direction is called *fusion*.

The former is easier to obtain than the latter. By injecting a neutron in a heavy nucleus (the most used is $^{235}\mathrm{U}$), that one becomes unstable and spontaneously splits into two lighter nuclei, producing energy. If this reaction produces neutrons, it can start a chain reaction and thus carry on until the fuel expires. This is the actual process used in nuclear electric power stations.

Fusion is, at present, much harder to obtain and it can't be used for electricity production. Overcoming the coulomb barrier between the two nuclei is necessary in order to put two atoms together and this is achievable only at high energy. Considering all the exothermic fusion reactions that selection rules allow, the most promising one (in terms of feasibility and availability of reagents) is the one involving deuterium ($^{2}\mathrm{H}$ or D) and tritium ($^{3}\mathrm{H}$ or T)

$$\mathrm{D} + \mathrm{T} \rightarrow {}^{4}\mathrm{He}(14.1\,\mathrm{eV}) + \mathrm{n}(3.5\,\mathrm{eV}) \tag{1.2}$$

In fact, at the kinetic energy of $100\,\mathrm{keV}$ this reaction has a cross section significantly higher than the others, as shown in figure 1.2. The energies between parenthesis indicate the products energy.

Energy balance argumentations and operational limits restrict the laboratory experiments to energies in the range $10 \div 20\,\mathrm{keV}$. Because of the energies involved and the statistical distribution of the particles speed in the phase space, only the fastest will produce fusion reactions.

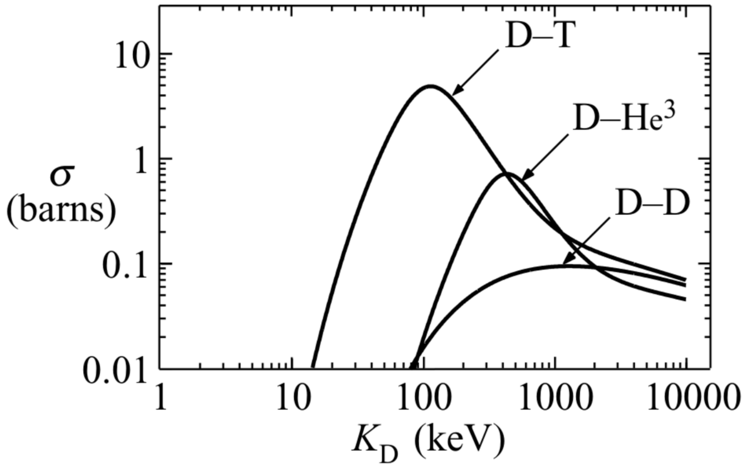

Figure 1.2: Cross section as function of the relative energy for three significant fusion reactions (Source [1]).

Nuclear fusion is intrinsically safer than fission and radioactive wastes (for the fusion, the T and the materials activated by the neutron flux) have a lifetime many orders lower than the ones produced by fission. This implies that nuclear fusion is a much more sustainable energy source than fission and thus it's really important to achieve it before the expiration of fossil fuels.

1.2 Magnetic confinement

Making fusion shooting a beam of D on a target of T at $100\,\mathrm{keV}$ won't have a remarkable gain because the fusion cross section is much lower than the elastic scattering cross section in that energy range. In order to overcome this problem, confining the particles is necessary, thus augmenting the number of collision a single particle can do. Two ways for making fusion are at present under studies: *inertial* confinement and *magnetic* confinement.

The former aims at obtaining fusion reactions using systems with high density and bringing these to high temperature for a short time, while the latter tends to confine the particles using a magnetic field for a sufficient time at a sufficient energy. Magnetic confinement is the one treated in this work.

The basic principle of magnetic confinement is the trajectory that charged particles follow in a magnetic field. The force ruling the motion is the well-known Lorentz force which has the expression

$$\mathbf{F} = q\mathbf{v} \times \mathbf{B} + q\mathbf{E} \tag{1.3}$$

where q is the charge of the particle, $\mathbf{v}$ its velocity, $\mathbf{B}$ the magnetic field and $\mathbf{E}$ the electric field. This one is globally lower than the magnetic field (the quasi-neutrality of the plasma grants this condition) and it has only local effects that won't be considered in the next paragraphs. The solution for equation 1.3 without the electric field is, in general, a spiral wrapping the field lines with radius ρ_L and frequency ω respectively

$$\rho_L = \frac{m|\mathbf{v}_\perp|}{q|\mathbf{B}|} \qquad \omega = \frac{q|\mathbf{B}|}{m} \tag{1.4}$$

where the subscript $\perp$ indicates the direction with respect to the magnetic field and m is the mass of the particle.

This gives a spatial confinement in the direction orthogonal to the field lines. In order to confine along the field lines, it is sufficient to close them, forming periodic structures.

The *drift motions* arise from configurations where the magnetic field is coupled to other forces or has a spatial gradient. After some calculations (see e.g. [2]) the following result for the drift motion of a particle can be obtained

$$\mathbf{v} = \frac{1}{q}\frac{\mathbf{F}\times\mathbf{B}}{|\mathbf{B}|^2} + \frac{1}{2}\frac{|\mathbf{v}_\perp|^2}{\omega}\frac{\mathbf{B}\times\nabla\mathbf{B}}{|\mathbf{B}|^2} \tag{1.5}$$

where $\mathbf{F}$ is a generic force and ∇ is the spatial gradient.

The toroidal coordinates, sketched in figure 1.3, can be introduced, calling ϕ *toroidal* angle, θ *poloidal* angle, R major radius and r minor radius. The maximum length for r is commonly indicated as *a*, while the average major radius is indicated as R_0.

If the magnetic field is only toroidal (thus it has only circular field lines) and it is induced by a current flowing in the 'hole' of the torus, following the Maxwell equation (neglecting the displacement current and assuming axis symmetry, hence $\frac{\partial}{\partial\phi} = 0$) this field will be inversely proportional to the radius:

$$\nabla\times\mathbf{B} = \mu_0\mathbf{j} \quad \Rightarrow \quad 2\pi R|B_\phi(R)| = \mu_0 I \quad \Rightarrow \quad |B_\phi(R)| = \frac{\mu_0 I}{2\pi R} \tag{1.6}$$

and this gradient in the radius direction will induce a force on the charged particles confined, following equation 1.6, orthogonal to the magnetic field. This force depends on the charge and then there will be charge separation and an electric field orthogonal to the magnetic field. This will induce another drift force on the particles but this time it will be independent from the charge, hence losing the particles on the wall.

This effect implicates that the magnetic field cannot be only toroidal, but it should have also a poloidal component in order to grant a better confinement. A

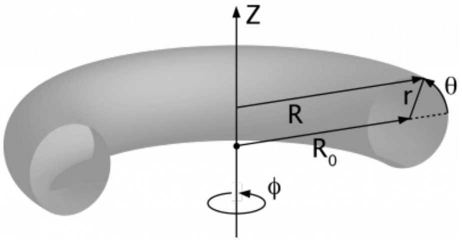

Figure 1.3: Sketch of the toroidal coordinates commonly used (source [3])

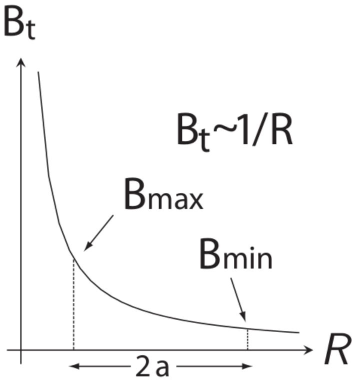

Figure 1.4: Dependence of the toroidal field B_ϕ on the major radius

graphical idea is given in figure 1.5. This is the *rotational transformation*, which is commonly indicated by the letter $\iota(r) = 1/q(r)$, where $q(r)$ is the *safety factor* and it is a measure of how tightly the field lines wrap in their helical motion:

$$q(r) = \frac{1}{\iota(r)} = \frac{\Delta\phi}{2\pi} \tag{1.7}$$

where $\Delta\phi$ is the toroidal angle that the lines need to do in order to return to the same poloidal position. The rotational transformation can be obtained in different ways.

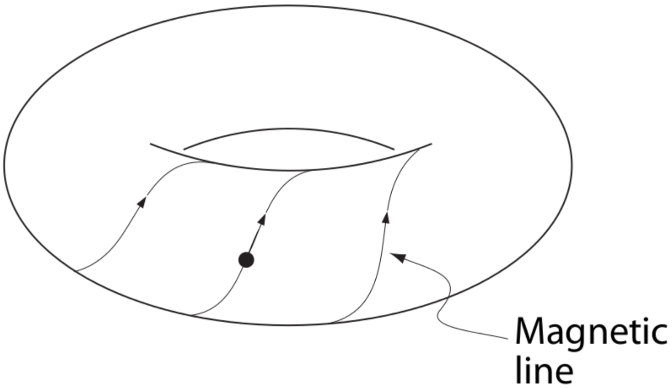

Figure 1.5: Graphical sketch of the rotational transformation (Source [1]).

In general, a given magnetic configuration can be obtained in infinite ways and the most used for magnetic confinement of thermonuclear plasmas are the following:

- **stellarator**: the rotational transformation is given by the peculiar shape of the coils;
- **pinch**: the toroidal component of the magnetic field is given by the coils while the poloidal component is produced by the plasma itself (a toroidal current is induced in the plasma).

In figure 1.6, a pinch design can be seen on the left while a stellarator one can be seen on the right.

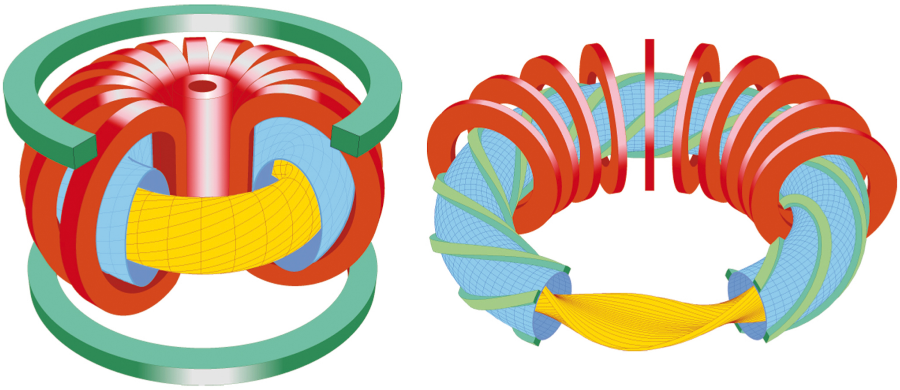

Figure 1.6: A design of a pinch (on the left) and of a stellarator (on the right). The red coils are the toroidal coils, the blue surface is the 'container' of the plasma (*vessel*), the yellow surface represents a magnetic surface (place where the magnetic field has the same value). In the pinch, the green coils are responsible for the position of the plasma, while in the stellarator they are responsible for the rotational transform.

1.2.1 Tokamak and Reversed Field Pinch

The work here presented focuses on the pinch configuration. This one (in particular the tokamak) is at present the most promising for the fusion reactors. An experimental tokamak (called ITER) is under construction and its effectiveness in terms of power gain will be crucial for the future magnetic fusion scenario.

As said before, in the pinch configuration the plasma itself generates the poloidal field which gives rise to the rotational transformation. This result can be obtained in two different ways, which are called *tokamak* and *Reversed Field Pinch* (RFP).

In both the configurations there is a set of coils enfolding the plasma container (*vessel*) and generating the toroidal field. Using the plasma as the secondary winding of a transformer, toroidal current can be induced in it, generating the poloidal magnetic field. The difference between the two configurations lies mainly in the relative intensity of the magnetic field used. In the tokamak, the toroidal field is much higher with respect to the poloidal field induced in the plasma (fig. 1.7). On the other side, in the RFP the intensity of the two is comparable and this (solving the equation of magneto-hydrodynamics (MHD), as will be done in the next section) leads to the reversed direction of the toroidal magnetic field near the plasma edge, as shown in figure 1.8.

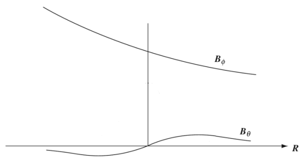

Figure 1.7: Components of the magnetic field for a tokamak

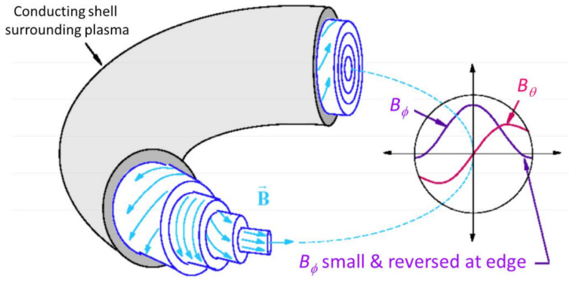

Figure 1.8: Sketch of the magnetic surfaces and components of the magnetic field for a RFP (image taken from [4])

This implies clearly some differences between the two configurations. For a torus with circular section the safety factor q can be expressed as

$$q(r) = \frac{rB_\phi(r)}{R_0 B_\theta(r)} = \frac{2\pi r^2 B_\phi(r)}{\mu_0 R_0 I_\phi(r)} = \frac{2B_\phi(r)}{\mu_0 R_0 j_\phi(r)} \tag{1.8}$$

The safety factor of a tokamak is positive while for a RFP it passes through the zero and becomes negative near the edge, as sketched in figure 1.9. The q profile of a RFP has negative consequences for ideal MHD stability: given that $q < 1$ everywhere, the Kruskal-Shafranov stability criterion ($q > 1$) [5] [6] is not satisfied and current-driven instabilities can arise. Moreover, when $q < 1$ the magnetic curvature is dominated by the poloidal field and this feature can encourage pressure-driven instabilities to develop, according to the energy principle [7]. On the other hand, the strong *magnetic shear* $s = \frac{r}{q}\frac{dq}{dr}$ implies that bending the field lines induces a strong restoring force, thus stabilising the system. Despite these limits, the RFP has a strong advantage with respect to the tokamak, in fact it needs a far lower toroidal magnetic field to sustain the discharge ($\sim 10\,\mathrm{T}$ for the tokamak and $\sim 0.6\,\mathrm{T}$ for the RFP), thus the toroidal field coils don't need to be made with super conductive materials and they can be closer to the plasma, reducing substantially the complexity of the device.

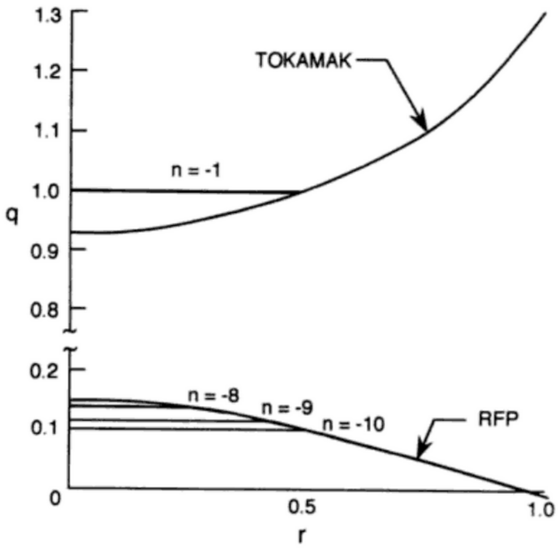

Figure 1.9: Comparison between the safety factor for a tokamak and a RFP (Source [8]). For the RFP, the value $q(0)$ is about $\frac{a}{2R_0}$.

Apart from these discussions, the RFP is an optimal configuration to study the plasma relaxation. Its features will be described in next section.

1.3 Physics of the RFP

The peculiarities of the RFP can be framed in the non-linear dynamo theory. Linear dynamos are useful to explain, at first order, the generation of the magnetic field of astrophysical objects by conversion of the poloidal magnetic flux in toroidal magnetic flux and vice-versa; in the RFP the poloidal flux is continuously supplied by the external circuit, hence there is no need for the toroidal flux to be converted but the reversed field must be maintained by the system and in this sense a dynamo effect is in act. In this section, the calculations describing the physics of the RFP are carried out. Further informations about plasma relaxation can be found at [8].

1.3.1 Resistive MHD

The plasma has a behaviour that couples the fluid motion and the electromagnetic field, thus the equations of fluid mechanics must be connected to the electromagnetic ones. The following calculations will be carried out for a non-relativistic system. Assuming the plasma has a current density **j**, the first set of equations is the following:

$$\frac{\partial \rho}{\partial t} = -\nabla \cdot (\rho \mathbf{v}), \tag{1.9a}$$

$$\rho \frac{d\mathbf{v}}{dt} = -\nabla p + \frac{1}{c}\mathbf{j} \times \mathbf{B} + \rho \mathbf{g}, \tag{1.9b}$$

$$\frac{\partial}{\partial t}\rho e = -\nabla \cdot (\rho e \mathbf{v}) - p \nabla \cdot \mathbf{v} + \eta J^2 \tag{1.9c}$$

where ρ is the density, p the pressure, e the energy density and η the plasma resistivity. The first equation represents the mass conservation, the second is the momentum conservation (assuming that the forces acting on the fluid are only the Lorentz force without electric field and the gravity) and the third is the energy conservation. In all these equations, the effect of thermal conduction and the sources of anisotropic pressure are neglected. The last equation can be simplified adding a state equation. The plasma behaves as a perfect gas with $\gamma = c_p/c_V = 5/3$, hence

$$\rho e = \frac{p}{\gamma - 1} \qquad \Rightarrow \qquad \frac{\partial \rho}{\partial t} = -\gamma p \nabla \cdot \mathbf{v} - \mathbf{v} \cdot \nabla p + (\gamma - 1)\eta j^2 \tag{1.10}$$

The electromagnetic field follows the well-known Maxwell equations and it influences the particles dynamic through the Lorenz force.

$$\frac{1}{c}\frac{\partial \mathbf{B}}{\partial t} = -\nabla \times \mathbf{E}, \tag{1.11a}$$

$$\frac{4\pi}{c}\mathbf{j} = \nabla \times \mathbf{B}, \tag{1.11b}$$

$$\nabla \cdot \mathbf{B} = 0, \tag{1.11c}$$

$$\mathbf{E} + \frac{1}{c}\mathbf{v} \times \mathbf{B} = \eta \mathbf{j} \tag{1.11d}$$

The equation resulting from the Gauss theorem is excluded due the quasi-neutrality of the plasma. Equation 1.11c has to be intended as an initial condition, because equation 1.11a implies that $\nabla \cdot \mathbf{B}$ does not change in time. The set of fourteen equations 1.9, 1.10, 1.11 describes the spatial and temporal evolution of the quantities ρ, p, $\mathbf{v}$, $\mathbf{B}$, $\mathbf{E}$ and **j**. They are the basic equations of resistive MHD. The equations of ideal MHD are obtained by putting the resistivity η to 0.

1.3.2 Energy minimisation in ideal and resistive MHD

It is well known that a physical system tends to seek a state of minimum potential energy. The states of minimum energy are called *relaxed* and are independent of initial conditions. In the case of a plasma with a perfect conductor as boundary (thus the electromagnetic energy can't enter or leave the system, because $\mathbf{E}_{\|}$ and $\mathbf{B}_{\perp}$ are 0) and thermally isolated the potential energy is in the form

$$W = \int_{V_0} \left(\frac{B^2}{8\pi} + \frac{p}{\gamma - 1} \right) \mathrm{dV} \tag{1.12}$$

A simple minimisation would lead to the state $W = 0$, thus some constraints must be included. Due to the boundary condition, the toroidal flux $\Phi = 2\pi \int_0^a B_z r dr$ must be fixed. In this case, the energy minimisation yields zero current. If we consider a closed unknotted curve C describing a surface S, then the flux through S is defined as

$$\Phi = \int_S \mathbf{B} \cdot \mathbf{n} dS = \oint_C \mathbf{A} \cdot d\mathbf{l} \tag{1.13}$$

where $\mathbf{A}$ is the potential vector. Since $\nabla \cdot \mathbf{B} = 0$, the *flux tubes* (the volume swept by all the lines passing through C) should close on themselves or fill all space ergodically. Thus on the lateral surface of each flux tube $\mathbf{B} \cdot \mathbf{n} = 0$. Clearly, Φ is constant along each flux tube. Let's consider now, as done by Woltjer in 1958 [9], the infinite set of integral

$$K_l = \int_{V_l} \mathbf{A} \cdot \mathbf{B} dV \quad , \quad l = 1, 2, \ldots, \infty \tag{1.14}$$

where l is the index of the closed flux tube of volume V_l and closed surface S_l. K_l is called helicity and somehow it measures the magnetic field topology. By calculating the time derivative of K_l and using $\partial \mathbf{A}/\partial t = -\mathbf{E}$, $\mathbf{B} = \nabla \times \mathbf{A}$, Gauss theorem and the assumption that $\mathbf{E} = -\mathbf{v} \times \mathbf{B} + \nabla \phi$ (satisfied by ideal MHD), the invariance of K_l can be found.

$$\frac{dK_l}{dt} = 0, \qquad l = 1, 2, \ldots \infty \tag{1.15}$$

This condition implies that the topological complexity of the field, once established, is fixed: flux tubes cannot be broken or reconnected.

Ideal MHD

The minimisation of the energy with the condition 1.15 should be done with the Lagrange multipliers technique. Anyway, Freidberg [10] demonstrated that it is equivalent to minimise the unconstrained energy in ideal MHD, approach which is mathematically simpler. In order to perform the minimisation, we consider an arbitrary displacement ξ of the plasma, which gives rise to a change in velocity $\delta \mathbf{v} = \partial\xi/\partial t$ and thus, with $\eta = 0$,

$$\delta \mathbf{B} = \nabla \times (\xi \times \mathbf{B}) \tag{1.16}$$

which implies

$$\delta W = \int \mathbf{B} \cdot \nabla \times (\xi \times \mathbf{B}) dV = \int \xi \cdot (\mathbf{B} \times \nabla \times \mathbf{B}) dV \tag{1.17}$$

and W is minimised ($\delta W = 0$) only if $\mathbf{B} \times \nabla \times \mathbf{B} = 0$, hence

$$\nabla \times \mathbf{B} = \mu(\mathbf{r})\mathbf{B}, \tag{1.18a}$$

$$\mathbf{B} \cdot \nabla\mu = 0 \tag{1.18b}$$

(the second equation is obtained by applying the divergence to the first equation) μ is a scalar function constant along each field line, following equation 1.18b, and, being each flux tube associated to K_l, we can associate each value of μ to a value of K_l, its value being determined by the initial conditions. Note that, using equations 1.11b and 1.18a, we can write

$$\mu(r) = \frac{\mathbf{j} \cdot \mathbf{B}}{B^2} \tag{1.19}$$

In the calculations above, the pressure has been neglected but if we consider it, this leads to the well-known equilibrium $\nabla p = \mathbf{j} \times \mathbf{B}$. In ideal MHD the system has memory of how it was prepared but this contradicts the property of relaxed state to be independent of the starting conditions. A smaller set of constraints must be sought.

Resistive MHD

If we consider also the resistivity, the electric field can be expressed as

$$\mathbf{E} = -\mathbf{v} \times \mathbf{B} + \frac{\eta}{S}\mathbf{j} + \nabla\phi \tag{1.20}$$

where S is an important dimensionless parameter called Lundquist number, defined as $S = \mu_0 a V_A/\eta$. μ_0 is the magnetic permeability of the vacuum, $V_A = B/\sqrt{\mu 0 n_i m_i}$ the Alfvén velocity (with n_i the ion density and m_i the ion mass) and η the resistivity. Calculating the time derivative of K_l, the result is that it doesn't vanish, thus the flux tubes can be broken and reconnected. It seems that there are no more constraints on W except for the total flux. Taylor [11] proposed a way out of this dilemma with the assumption that the *sum* of all the K_l is invariant. The only constraint that should be considered is thus the *total magnetic helicity*

$$K_0 = \int_{V_0} \mathbf{A} \cdot \mathbf{B} dV \tag{1.21}$$

The gauge invariance is resolved if the boundary condition $\mathbf{B} \cdot \mathbf{n} = 0$ on the surface is satisfied. In this case, the minimisation yields to a solution similar to equation 1.18 but with a significant difference:

$$\nabla \times \mathbf{B} = \mu \mathbf{B} \tag{1.22}$$

where μ is now a constant. In the case of toroidal geometry, the definition of K_0 must be changed in order to take account of the linkage between the magnetic flux through the center of the torus, due to the applied voltage, and the toroidal flux interior to the plasma. So the helicity can be written as

$$K = \int_{V_0} \mathbf{A} \cdot \mathbf{B} dV - \oint \mathbf{A} \cdot d\mathbf{l}_1 \oint \mathbf{A} \cdot d\mathbf{l}_2 \tag{1.23}$$

where the subscripts (1,2) indicate the two direction of the torus (poloidal and toroidal). The possibility of the field lines to break and reconnect allows the pressure to equilibrate over the entire plasma volume and thus formally, upon performing a separate minimisation, the condition $\nabla p = 0$ is obtained in the fully relaxed state [11].

1.3.3 Magnetic Modes

Before studying the solutions to the minimisation process in resistive MHD, it is useful to introduce the entity that will be called *magnetic mode*. In general, the toroidal magnetic field in toroidal geometry can be decomposed in a mean part and in a fluctuating part:

$$\mathbf{B}^T(r, \theta, \phi) = \mathbf{B_0}^T(r) + \sum_{m,n} \mathbf{b}^T_{(m,n)}(r) \exp(i(m\theta + n\phi)) \tag{1.24}$$

Where $\mathbf{B_0}(r)$ is the constant part (we will assume it depends on the radius), i is the imaginary unity, n and m are integers, θ is the poloidal angle and ϕ is the toroidal angle. An example of a $m = 0$ mode and a $m = 1$ mode is given in figures 1.10 and 1.11, where the vertical axis is the ϕ direction and the lines wrapping the flux tube represent the θ direction. Important macroscopic quantities used in the characterisation of a RFP plasma modes behaviour are listed below:

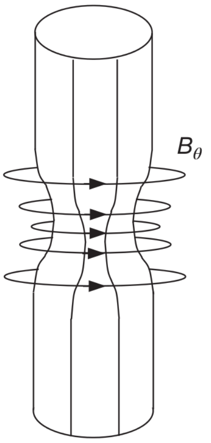

Figure 1.10: Graphic of a $m = 0$ instability, called commonly *sausage* (source [12])

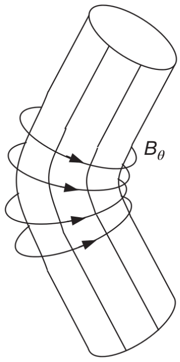

Figure 1.11: Graphic of a $m = 1$ instability, called commonly *kink* (source [12])

- *spectral width*: this quantity gives an indication on the modes spectral spread, i.e. how many modes are interacting. Usually this quantity is calculated for the $m = 1$ modes because these are the most important in the RFP, as will be explained later. Given $W_n = \dfrac{B_n^2}{2\mu_0}$ the energy of a magnetic mode with poloidal number n, the spectral width N_s is defined in equation 1.25. The lowest is this value, the highest is the 'peaking' of the spectrum, that is there is a mode higher than the others. In figure 1.12 two examples of the modes amplitude are shown. Usually, the modes amplitude is normalised to the poloidal field at border, as done in the figure. In the upper figure, the modes present lower value of the spectral width and thus the spectrum is broader compared to the other.

- *locking strength (LS)*: another important feature that should be quantified is the macroscopic deformation of the plasma column due to the interaction between the modes. This structure is given by a phase-locking of the MHD modes and it can lock to the wall, causing a preferential plasma-wall interaction [14]. The toroidal and poloidal position can be reconstructed using using some numerical codes [15]. The 'locking strength' is defined as the normalised sum of the cosine of the interacting modes phase difference

$$\mathrm{LS} \propto \sum_{n1,n2=n_{\min}}^{n_{\max}} \cos(\phi_{n1} - \phi_{n2}) \tag{1.26}$$

This value is upper bounded and if it reaches the maximum this means that

$$N_s = \left[\sum_n \left(\frac{W_n}{\sum_{n'} W_{n'}}\right)^2\right]^{-1} \qquad (1.25)$$

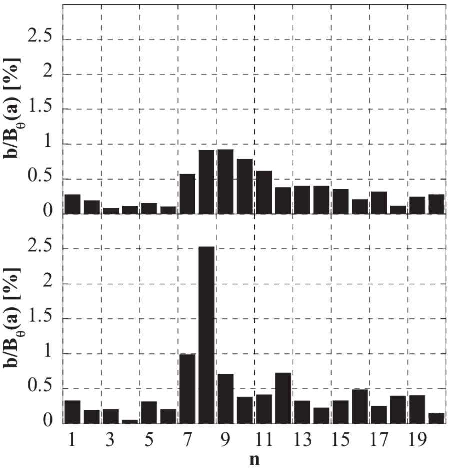

Figure 1.12: Example of the spectral width for two different shots. (source [13])

the modes are locked, otherwise the minimum value means random phase difference. In figure 1.13 a strong mode interaction can be seen.

- *locking position (LP)*: this is the position where the maximum value of LS is reached. The modes can move during the discharge evolution or lock at a specific position and this event can case a high interaction with the wall at that position.

From now on, referring to a (m, n) mode will be a short notation for the modes number in expression 1.24. The sign of m is always positive, while the sign of n can be both positive or negative if $m = 1$. The sign is an indication of the sense followed by the helical distortion induced by the mode. Usually the internal modes have $n < 0$ while the external have $n > 0$. In a magnetic configuration (both tokamak or RFP), the presence of magnetic modes is really important and the presence of these modes at particular surfaces of the plasma (called $resonant$, that is where $q = -m/n$) can lead to instabilities. In the RFP in particular, the modes are fundamental for the self-sustainment of the discharge, as will be described later.

1.3.4 Application of Taylor's theory to a toroidal geometry

The results are applied to a toroidal geometry, with minor radius *a* and major radius R_0. Consistently with the condition $\mathbf{B} \cdot \mathbf{n} = 0$, $B_r(a) = 0$ is considered. By applying the curl to equation 1.22 and using the condition $\nabla \cdot \mathbf{B} = 0$, the following

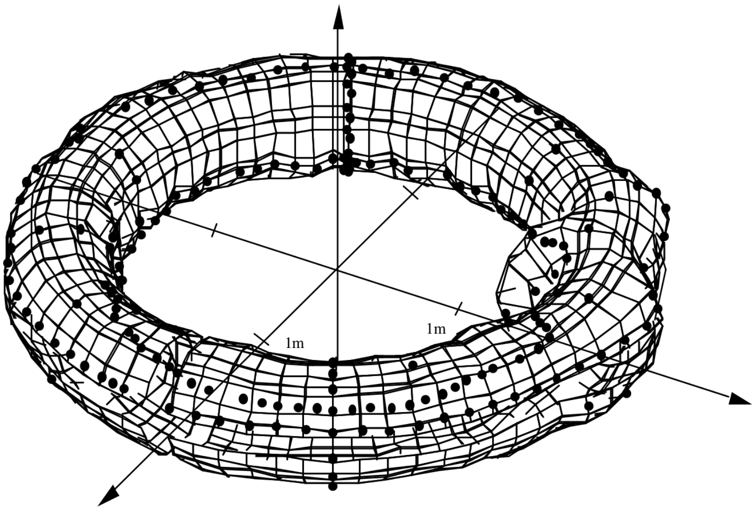

Figure 1.13: Magnetic reconstruction of the edge magnetic field. The strong deformation induced by the modes interaction can be seen.

equation for the axial component of $\mathbf{B}$ can be found:

$$\nabla^2 B_z + \mu B_z = 0 \tag{1.27}$$

which general solution is the real part of

$$B_z = \sum_{m,k} a_{m,k} J_m(\alpha r) \text{exp}[i(m\theta + kz)] \tag{1.28}$$

where $\alpha^2 = \mu^2 - k^2$, m and k are (positive) integers, J_m is a Bessel function and the quantisation introduced by the periodic conditions has been neglected. The other components of $\mathbf{B}$ can now be found with equation 1.22. Over all the possible solutions, only two have the absolute minimum energy:

- cylindrically symmetric solutions with $m = 0$ (called also Bessel Function Modes (BFM))

$$B_z/B_0 = J_0(\mu r), \tag{1.29a}$$
$$B_\theta/B_0 = J_1(\mu r), \tag{1.29b}$$
$$B_r/B_0 = 0 \tag{1.29c}$$

- helically symmetric solutions with $m = 0$ and $m = 1$

$$B_z/B_0 = J_0(\mu r) + a_{1,k} J_1(\alpha r)\cos(\theta + kz), \tag{1.30a}$$

$$B_\theta/B_0 = J_1(\mu r) + \frac{a_{1,k}}{\alpha}\left[\mu J_1'(\alpha r) + \frac{k}{\alpha r}J_1(\alpha r)\right]\cos(\theta + kz), \tag{1.30b}$$

$$B_r/B_0 = -\frac{a_{1,k}}{\alpha}\left[k J_1'(\alpha r) + \frac{\mu}{\alpha r}J_1(\alpha r)\right]\sin(\theta + kz) \tag{1.30c}$$

An important relation between the helicity, the toroidal flux and the normalised parallel current density μa is the following:

$$\frac{K}{\Phi_z^2} = \frac{L}{2\pi a}\left[\frac{\mu a\left[J_0^2(\mu a) + J_1^2(\mu a)\right] - 2J_0(\mu a)J_1(\mu a)}{J_1^2(\mu a)}\right] \tag{1.31}$$

and it can be shown that the ratio K/Φ_z is proportional to the volt-seconds available from an external circuit used to drive the discharge, thus it is experimentally controllable and this feature has been observed. It is useful to introduce the field reversal parameter F and the pinch parameter Θ:

$$F = \frac{B_z(a)}{\langle B_z\rangle} = \pi a^2\frac{B_z(a)}{\Phi_z} \overset{BFM}{=} \frac{\mu a J_0(\mu a)}{2J_1(\mu a)}, \tag{1.32a}$$

$$\Theta = \frac{B_\theta(a)}{\langle B_z\rangle} = 2\pi a\frac{I_z}{c\Phi_z} \overset{BFM}{=} \frac{\mu a}{2} \tag{1.32b}$$

thus the theory predicts $F < 0$ (the RFP configuration) when $\Theta > 1.2$. The helically distorted states exist for discrete values of μ, obtained when $B_r(a) = 0$. The lowest value of Θ for which such solutions exist is 1.56 and in this case the quantity K/Φ_z^2 no longer express μ, but the amplitude of the helical distortion. Θ cannot be raised above 1.56, in fact when this is tried by augmenting the external circuit volt-seconds, the helical distortion increases the plasma inductance and additional voltage is absorbed without augmenting the current. The state above 1.56 has $m = 1$ and an axial mode number $ka = 1.25$.

1.3.5 Phenomenology of relaxation in the RFP

The theory exposed above is interesting and gave many explanation to a large variety of phenomena, but the theory couldn't fully prescribe the profiles due to the pressure gradients, induced by the temperature gradients related to keep the hot thermonuclear plasma away from the cold edge. The pressure gradient has two negative effects: firstly, it induces a perpendicular current density that, although small, contributes to the total current density; secondly, the temperature gradient corresponds to a resistivity gradient because of the Spitzer law for plasma resistivity

($\eta \sim T^{-3/2}$), causing a higher dissipation in the outer region. In order to have more realistic profiles, it is necessary to separate the contribution of perpendicular and parallel components and this is done by separating the pressure contribute from the larger force-free parallel current one. The fully relaxed state is obtained by posing $\mu = constant$ and $\nabla p = 0$.

In cylindrical geometry, the nondimensional equations are the following:

$$\frac{\beta_0}{2}\nabla p = \mathbf{j} \times \mathbf{B} \tag{1.33}$$

$$\nabla \times \mathbf{B} = \mathbf{j} = \mathbf{j}_{\parallel} + \mathbf{j}_{\perp} \tag{1.34}$$

where

$$\mathbf{j}_{\parallel} = \frac{\mathbf{j} \cdot \mathbf{B}}{B^2}\mathbf{B} = 2\Theta_0 \mu \mathbf{B} \tag{1.35}$$

$$\mathbf{j}_{\perp} = -\frac{\mathbf{j} \times \mathbf{B}}{B^2} \times \mathbf{B} = -\frac{\beta_0}{2}\frac{\nabla p \times \mathbf{B}}{B^2} \tag{1.36}$$

and

$$\Theta_0 = \frac{\mu(0)a}{2} \qquad \beta_0 = \frac{8\pi p(0)}{B_0^2} \tag{1.37}$$

Specifying now $\mu(r)$ and $\nabla p(r)$ we can find $\mathbf{B}(r)$ as:

$$\frac{\partial B_z}{\partial r} = -2\Theta_0 \mu B_\theta - \frac{\beta_0}{4}\frac{\partial p}{\partial r}\frac{B_z}{B^2} \tag{1.38}$$

$$\frac{\partial B_\theta}{\partial r} = -\frac{B_\theta}{r} + 2\Theta_0 \mu B_z - \frac{\beta_0}{4}\frac{\partial p}{\partial r}\frac{B_\theta}{B^2} \tag{1.39}$$

Now, specifying the values of Θ_0, β_0 and the profiles of μ and p the field profiles B_z and B_θ can be found by integration. The usual profile of μ is described by the following equation:

$$\mu = \frac{2\Theta_0}{a}\left[1 - \left(\frac{r}{a}\right)^{\alpha}\right] = \mu(0)f(r) \tag{1.40}$$

It must be noted that for the force-free part of the profile (thus neglecting the contribution of β), Θ_0 and α completely describe the profiles, with α representing the width of the current channel. A parametric MHD stability analysis can be performed [16], we report here only the results concerning the work for this thesis, that can be displayed in the graph of figure 1.14: the ideal and MHD analysis for the $m = 1$ case are there summarised. The region where the RFP is stable is bounded by the $F = 0$ curve, which corresponds to a transition to a non-reversed profile, and the curve $F = \infty$, that corresponds to a vanishing toroidal flux. Inside this region, the curves that bound the complete MHD stability for the modes are reported.

In this α-Θ_0 space the trajectories of diffusing profiles due purely to resistive diffusion can be easily seen (see e.g. figure 1.15). Keeping a constant value of Θ, during the temporal evolution α tends to decrease and Θ_0 to increase, thus peaking the current distribution on the axis.

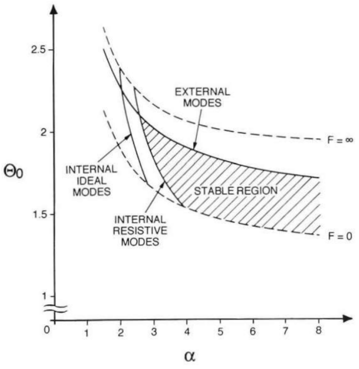

Figure 1.14: Stability diagram in the α-Θ_0 space (Image taken from [8])

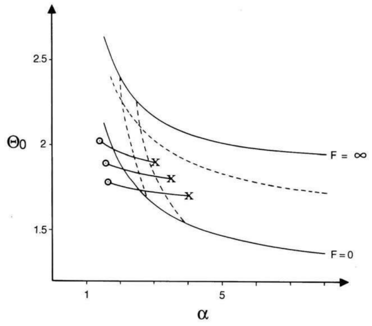

Figure 1.15: Path of resistive diffusion profiles in the α-Θ_0 space. X is the initial condition while $\odot$ is the final one. (Image taken from [8])

1.3.6 Resistive diffusion

If we consider that the classical resistive diffusion is the main actor in the RFP configuration, the following equation should be added

$$\frac{\partial \mathbf{B}}{\partial t} = \eta \nabla^2 \mathbf{B} \tag{1.41}$$

where η is the uniform nondimensional resistivity for a static conductor. This equation has the cylindrically symmetrical solution

$$B_\theta = B_0 J_1(\mu r) e^{-t/\tau}, \tag{1.42a}$$

$$B_z = B_0 J_0(\mu r) e^{-t/\tau} \tag{1.42b}$$

where $\tau = a^2/4\eta\Theta^2$. When $\nabla p = 0$ the BFM profile preserves its radial structure while decaying and thus τ represents an upper limit in the discharge time. This is in high contrast with the experiments, as shown in figure 1.16. Assuming an anisotropy in the resistivity (necessary due to the anisotropy given by the magnetic field), the solutions will rapidly decay in time thus losing the reversed field. To maintain a steady-state RFP profile some field generation mechanism is necessary and this mechanism can be explained as a dynamo.

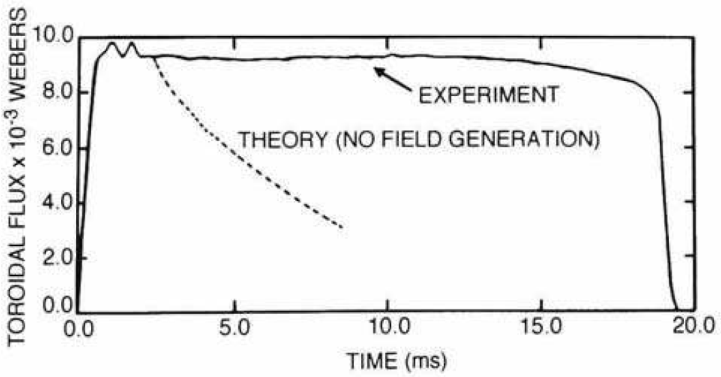

Figure 1.16: Comparison between the theoretical and experimental magnetic flux (proportional to the current) (Image taken from [8])

1.3.7 Dynamo Theory

The dynamo theory explains the long lasting existence of the astrophysical magnetic fields. This field is generated by the motion of the plasma, thus there is a coupling between the velocity field and the magnetic field. The *kinematic dynamo theory* finds the solution to the MHD field equations in a condition where the velocity field is *prescribed* and satisfies the motion equation. This theory applies only if we can assume that the Lorentz force can be dropped from the momentum equation, which is true if the energy density of the magnetic field is much smaller than the internal and kinetic energy density of the fluid.

The steady solution to this problem leads to the phenomenon that the toroidal field must be generated by the toroidal field and *vice versa*. The toroidal field can be created from poloidal field through differential rotation (as sketched in figure 1.17) but the generation of poloidal field from the toroidal one is much more complicated. The Cowling's Theorem states that magnetic field that are symmetric about an axis cannot be maintained by symmetric motions. Heuristically, this explains the impossibility of a field-reversed symmetric state: considering a symmetric cylindrical equilibrium with finite resistivity, in the RFP the $B_z = 0$ surface must lie within the plasma. Here a field line is only poloidal and closes on itself and the loop voltage around this surface is $\oint \mathbf{E} d\mathbf{l} = \oint \eta J_\theta r d\theta \neq 0$. The total toroidal flux inside the surface must then change in time, in contradiction with the equilibrium hypothesis. Hence a symmetric RFP cannot be maintained and some sort of dynamo must sustain the discharge.

If we consider a *turbulent dynamo*, considering that $\mathbf{B}$ and $\mathbf{v}$ are composed by a mean part (with the subscript 0) and a random fluctuating part (in small letters),

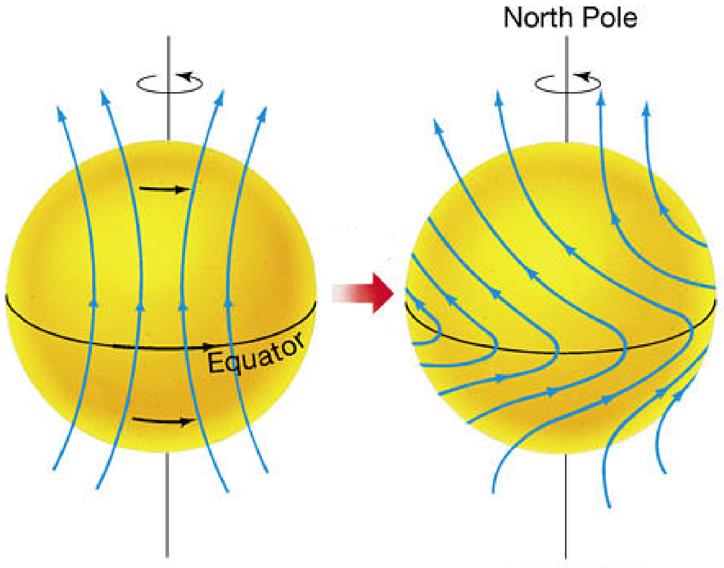

Figure 1.17: Sketch of the generation of toroidal field from poloidal field through differential rotation

the temporal evolution of the magnetic field is as follows:

$$\frac{\partial \mathbf{B_0}}{\partial t} = \nabla \times (\mathbf{v}_0 \times \mathbf{B}_0) - \nabla \times \mathbf{E}_f - \nabla \times \frac{\eta}{S} \nabla \times \mathbf{B}_0 \tag{1.43}$$

where

$$\mathbf{E}_f = -\langle \mathbf{v} \times \mathbf{b} \rangle \tag{1.44}$$

This electric field can compensate the resistive diffusion effects and thus sustain the magnetic field for longer times than the diffusion time.

In the RFP, the condition that the magnetic energy density is small compared to other energy densities is not satisfied. This implies that the RFP dynamo is inherently non-linear. In this configuration, the poloidal flux is supplied by the external applied voltage and there's no need for a reconversion system. If this voltage is set to zero, the RFP ceases to exist. The dynamo here implies that the reversed magnetic field is self-sustained and regenerated. Nonetheless, the turbulent dynamo theory seems to apply to the RFP because of the long field lifetimes and thus there is something that counteracts the resistive dissipation. In this configuration, there is no small scale turbulent but rather a superposition of long wave laminar motions.

1.3.8 Energy interchange between the modes

The basic process generating the field has been identified, the problem is now describing how it reveals in the plasma. It will be shown that there is an energy exchange between the magnetic modes inside the plasma which allows the field generation.

Firstly, the $m = 1$ modes grow. To understand why this happens, let's consider the forces acting to alter the RFP. The edge is usually colder and thus, following the Spitzer resistivity formula $\eta \sim T^{-3/2}$, more resistive. The current flows more in the core of the plasma, thus augmenting the temperature and lowering the resistivity in the center. Simultaneously, the resistive diffusion in the edge starts destroying the RFP profile. This enhancement of current in the center leads to a fall in $q(0) \sim B_z(0)/J_z(0)$, which results in a flattening of the q profile in the central region and a lowering of the shear stabilising effect. As a result, a global MHD kink mode ($m = 1$) develops in the core of the plasma, at a surface where $0 < q(= -m/n) < q(0)$. This mode grows faster than the thermal instability driven by transport and thus a reconnection occurs, lowering $q(0)$ up to the condition $q(0) < -m/n$. This condition is more unfavourable for the plasma but the kink mode continues its growth, leading to a second reconnection that raises $q(0)$ to a higher value than the beginning. This restores a stable RFP state and then the chain is free to repeat in a cyclical manner.

It has been demonstrated that such state would be able to sustain the RFP alone in a steady state, but it has never been experimentally seen. The closest condition to it is the so-called Quasi-Single Helicity (QSH), where a mode is highly dominant with respect to the others (see as an example [17], [18] and [19]). Usually, the behaviour of a RFP plasma is highly dynamical. The magnetic fluctuations are due to the fact that there is no $(1, n)$ state which is preferred thus each one is able to produce its own helical deformation and the plasma oscillates between various states. This idea of coupling between various states, with different m and n, is the basis of the relaxation event that lowers the energy of the plasma and maintains the RFP.

Ho and Craddock [20] were able to simulate a non-linear process that occurs in the relaxation event. *Firstly* the energy is transferred from the mean poloidal field to the $(1, n)$ modes as described above. This modes non-linearly generate the $m = 0$ modes, which act as intermediaries for the energy exchange between the inner modes and the ones closer to the *reversal* surface (the surface where $q = 0$). This non-linear process has also been observed, because the power input is much more than the one required to sustain the inner mode. *Finally* the energy is quasi-linearly transferred from the external modes to the mean toroidal field, thus sustaining the discharge. In the end, this process enables the poloidal flux to be converted in toroidal flux in a non-linear way.

All the results reported above have been experimentally observed (see as an example [21]). These relaxation events can be related to the condition called *mode locking* (LM), where both the $m = 1$ and $m = 0$ modes lock in phase and create a toroidally deformation that occupies around 50 toroidal degrees. The LM region is characterised by an enhancement of the plasma-wall interaction. In figure 1.18 the evolution of some plasma parameters is shown during a reconnection event.

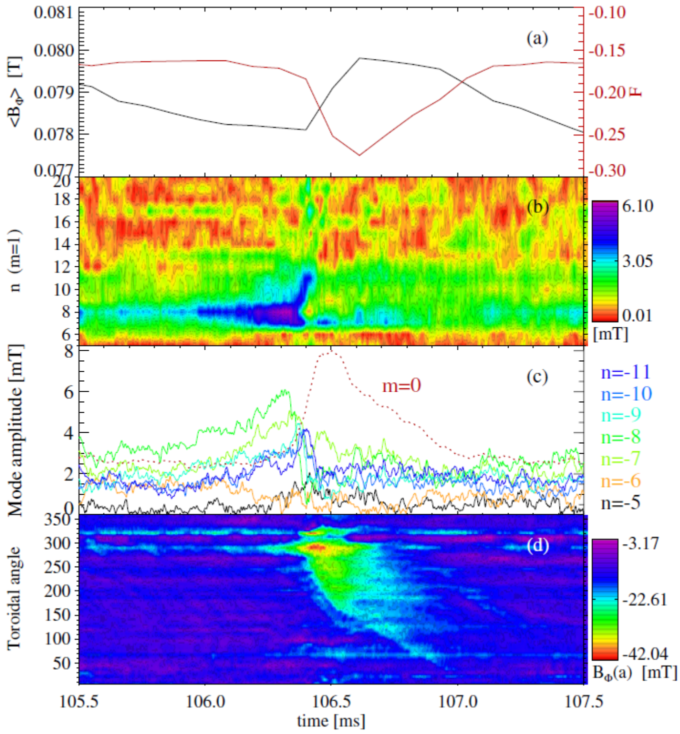

Figure 1.18: The evolution of some plasma parameters during a relaxation event. As can be seen, the internal modes $m = 1$ lose their amplitude and simultaneously the outer n and the $m = 0$ modes grow. This causes a drop in F and the field maintains the reversal. The growth of the $m = 0$ modes is associated to a phase locking of the modes. (image taken from [21])

1.3.9 Thermal transport

We treated the relaxation analysing the magnetic modes, but a substantial part is also linked to the transport of the particles. In the RFP discharges the phenomenology of so-called Discrete Relaxation Events (DRE) is usually seen: a cyclical asymmetric behaviour characterised by a slow rise phase in which the plasma core is heated, followed by a fast lost of thermal energy from the center. Such an example can be seen in figure 1.19.

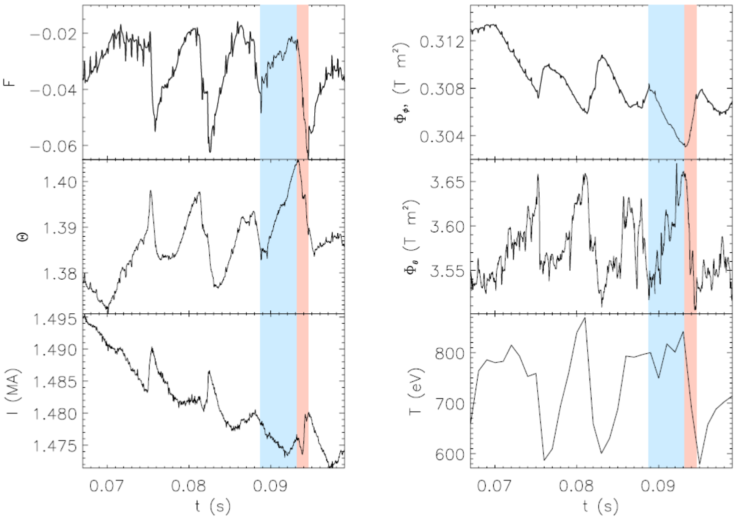

Figure 1.19: Evolution of some plasma parameters during a DRE in the RFX-mod device (shot $\#29891$). (Image taken from [22])

The rising phase can be easily explained by the central resistivity growth following the cooling of the edge, as explained in subsection 1.3.8. We expect also the linear growth of the magnetic modes, and this hypotheses have been verified. During the crash phase, dynamo activity has been observed, with the generation of the toroidal flux starting from the fluctuations of the $m = 0, 1$ modes.

In the steady phase, the safety factor is a function only of the radius thanks to the axis-symmetry of the configuration. This permits to imagine the magnetic field surfaces as nested, each one characterised by a value of q. The high thermal transmission over the axial direction results in the constancy of the temperature on a flux surface, although the inner surfaces are hotter. The low thermal conductivity orthogonal to the flux surfaces is the result of the good confinement. During the crash phase, the RFP dynamo is active and thus the modes grow, with the result that some magnetic islands can form on the resonant surfaces (where $q = -m/n$). These islands can grow and overlap, thus the magnetic field lines become *stochastic*: they are no more fixed to a particular surface and fill ergodically the space. The ergodisation begins in the core and can eventually fill the complete volume. This leads to a drop in the radial confinement and thus a lost of energy to the wall. Simultaneously, the dynamo restores the relaxed state profile and thus the confinement is restored. This phenomenon is common in the RFP dynamic and has been observed in many RFP experimental devices.

1.4 Reversed Field eXperiment - RFX

The Reversed Field eXperiment (RFX), located in Padova (IT) is the biggest RFP device active at present. It was built in 1991 and produced its first plasma in 1992. RFX is extremely flexible because it can be used either as a RFP or a tokamak. In the years 2000 it was upgraded to RFX-mod (modified) [23] by making the shell thinner and adding an active system in the vacuum vessel designed to control the plasma instabilities. The system mounted on RFX-mod is the most complex and most flexible of its type, in fact there are (192) coils and each one is independently alimented. This feature highly enhances the stability of the RFP plasma.

In table 1.4, the main technical characteristics of RFX-mod are summarised

Major radius, R	$2\,\mathrm{m}$
Minor radius, a	$0.46\,\mathrm{m}$
Total plasma volume	$\sim 10\,\mathrm{m}^3$
Maximum plasma current	$2\,\mathrm{MA}$ (RFP) $200\,\mathrm{kA}$ (tokamak)
Maximum applied toroidal field	$0.7\,\mathrm{T}$
Maximum pulse length	$500\,\mathrm{ms}$ (RFP) $1\,\mathrm{s}$ (tokamak)

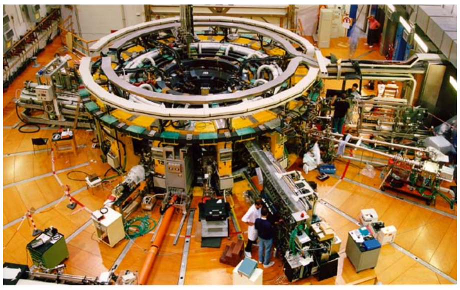

Figure 1.20: Photo of the RFX-mod experiment (Source [24])

In the 1990, a really important result was achieved with RFX, showing the existence of the QSH. RFX-mod is important because it can study both the RFP and the tokamak configuration in a similar environment (same geometry) and, in particular, with the same materials facing the plasma. A comparison between these magnetoplasma configuration can be thought and this characteristic is unique in the world.

1.5 Conclusion

In this chapter, the basic principles of the thermonuclear fusion with magnetic confinement have been presented. The most used magnetoplasma configuration (tokamak and RFP) have been shown and studied in their main features, analysing the differences between them. A deeper treatment of the RFP configuration was necessary because the work of this thesis mainly focuses on this type of device. The basic equations of MHD were used to treat the energy minimisation (both in ideal and resistive case) and this leads to the equilibrium of the RFP as a function of different parameters (in particular Θ and F). This theory alone was unable to explain the reversed field configuration, thus the dynamo theory has been introduced to explain how the magnetic field reorganises in order to reverse the field at the edge. The thermal transport and the DRE have shortly been explained. Lastly, the RFX-mod experiment has been presented in its main features.

2

Operational limits and disruptions

In this chapter, critical events that lead to the abrupt termination of the plasma discharge are presented. Operational limits are well-known in the tokamak configuration and within this limits the confinement is good. Exiting from these limits leads to a phenomenology called *disruption*, which is at present under studies. This phenomenon is really harmful because it can lead to deterioration of the materials facing the plasma and to mechanical stress on the vessel and conducting in-vessel components. In the RFP scenario, disruptions have never been experienced but similar type of current shut down, usually called *fast termination* has been recently seen in RFX-mod. The only operational limit deeply studied is the one concerning density.

2.1 Operational limits for a tokamak

There are three main limits that a tokamak must not overpass in order to maintain both the thermal and particle confinement. These are called *operational limits* and can be characterised in terms of plasma quantities.

2.1.1 Density and q limits

Two of the quantities that define the operational limits are the density and the safety factor. The density limit has been described by Greenwald [25] and it can be expressed in terms of a normalised plasma density:

$$\bar{n}(10^{20}\mathrm{m}^{-3}) < \frac{I(\mathrm{MA})}{\pi a(m)^2} = n_G \qquad (2.1)$$

where $\bar{n}$ is the average density, a is the minor radius of the plasma and n_G is called Greenwald density. This limit depends on the heating power injected in the plasma, as can be seen in figure 2.1, that displays the so-called Hugill diagram. The x-axis represents the Murakami parameter $\frac{\bar{n}R}{B_\phi}$. The density limit is strictly connected to the radiation coming from the outer layers. When the density it too high, the power losses by radiation carry away energy from the plasma and thus a loss of confinement occurs. The higher is the power injected with auxiliary power, the better is the response of the plasma to high edge losses by radiation. The theme of density limit for toroidal plasmas has been largely discussed by Greenwald in [26].

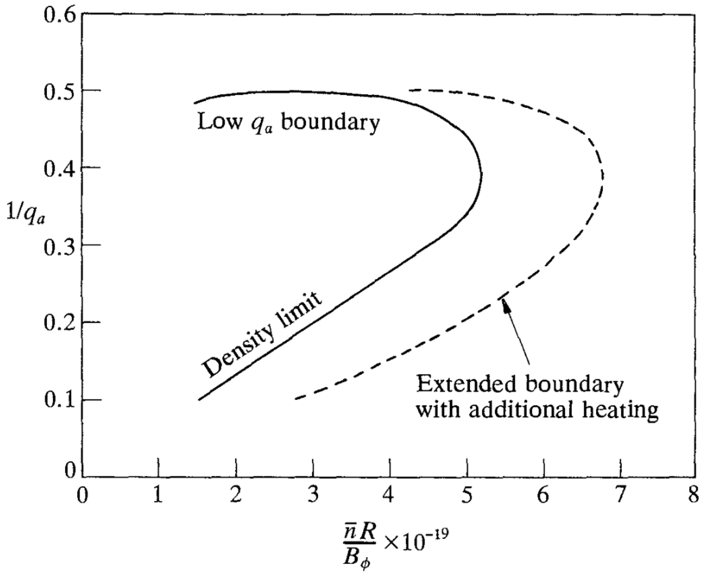

Figure 2.1: Hugill diagram for a tokamak. It can be clearly seen the dependence of the density limit from the additional heating (Source [2])

The safety factor is another parameter to keep under control in order to avoid strong MHD instabilities. q on axis is bounded to be greater than 1 (otherwise a benign instability called *sawtooth* can develop [5] [6]) and thus, following equation 1.8, the current density on axis is limited. Fixed the toroidal field, augmenting the toroidal current will give rise to steeper current density profiles at the edge of the plasma. As the value $q_a = 2$ is approached, the $q = 2$ surface moves outward and the instability modes developing in this resonant surface can grow to a catastrophic level because of the high destabilising effect of the current gradient. Given that the q profile in a tokamak is increasing with the radius, the common experimental set-up is to maintain the value of q_a higher than 3 in order to keep the $q = 2$ surface sufficiently inside that plasma and avoid this problem. This limit can be thought also as a current limit. In figure 2.2, a plot representing the evolution of some properties of the plasma shows that the discharge ends when $q_a = 2$.

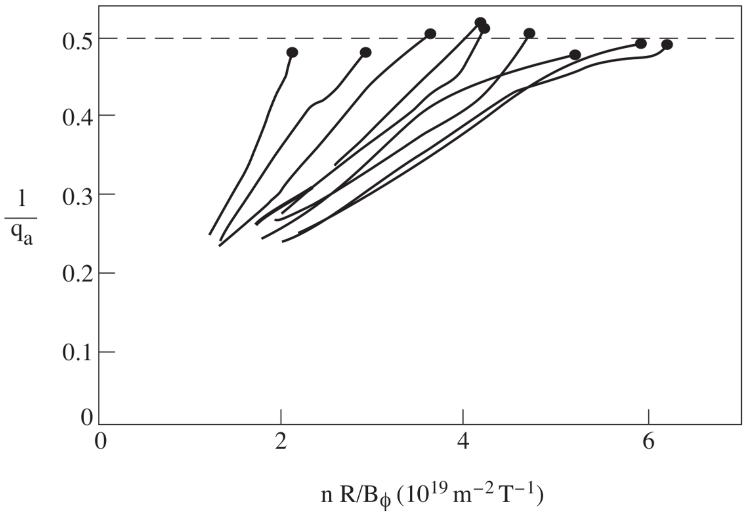

Figure 2.2: Evolution of some parameters in JET disruptions, showing the q limit (Source [27])

2.1.2 β limit

The last parameter that can be source of instabilities is the pressure. In plasma physics, the parameter tightly bound to the pressure is the parameter β, which can be expressed as follows

$$\beta = \frac{\bar{p}}{\frac{B^2(a)}{2\mu_0}} \tag{2.2}$$

where the bar indicates the average over the section. The most known limit of β has been written by Troyon [28] [29] as

$$\beta(\%) < g\frac{I(\mathrm{MA})}{a(\mathrm{m})B_\phi(\mathrm{T})} \tag{2.3}$$

where $g \sim 3$. This expression can be written in function of the safety factor:

$$\beta(\%) < g\frac{a}{R_0}\frac{1}{q(a)} = g\beta_N \tag{2.4}$$

The negative influence of this limit is given by the fact that the power obtained with nuclear fusion is dependant from the β parameter. In fact the following relation can be written:

$$P_F \propto \beta^2 B^4 \frac{<\sigma v>}{T^2} \tag{2.5}$$

where P_F is the power obtained by nuclear fusion, σ is the cross section of the nuclear reactions, the angled parenthesis indicate the average over the energy of the particles and T is the temperature. Since reaching high values of β is not possible due to this limits, this implies that P_F cannot be raised by augmenting it.

Overpassing one of the limits expressed above would lead to instabilities and, in the worst case scenario, to a disruption.

2.2 Disruptions

A disruption is the sudden loss of the energy stored in the plasma, followed by the very fast termination of the discharge. It's really harmful for a device and it must be avoided, or at least mitigated, in the future tokamak experiments and fusion reactors. The disruption is the extreme consequence of a series of instabilities that can develop when the control of the main operational parameters is lost. However, the physics of a disruption doesn't vary with the different instability triggering it. Kadomtsev [30] has interpreted this phenomenon as a dramatic relaxation event, similar to the DRE described in Chapter 1 but different because it doesn't imply a cyclical nature. The plasma could try to reach a more stable (thus less energetic) state by reorganisation of its magnetic configuration with a sudden relaxation which is not sustainable by a tokamak. This interpretation of the disruption event, that makes it similar to the relaxation events in the RFP, is the main reason for the work exposed in this thesis.

For further information about the disruptions, please look at [31], [32], [33], [34].

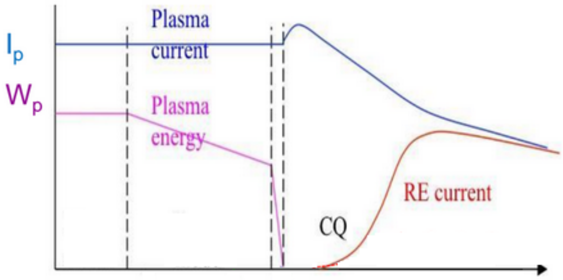

Figure 2.3: Main quantities for a disruption. As can be seen, the energy of the plasma is lost, then there is the current quench and the current of runaway electrons increases. (Source [35])

2.2.1 Development of a disruption

Pre-disruptive phase

The causes of the disruption are strictly bounded to the length and the physics of the first phase, called pre-disruptive phase. It can last from a ms to $100\,\mathrm{ms}$, depending on the cause and on the size of the machine. The causes of a disruption will be treated in detail later.

Thermal quench

This is the phase where the thermal energy of the plasma is lost to the wall by conduction and/or convection and radiation. It's the fastest phase of the disruption and its typical times are from $10\,\mu\mathrm{s}$ to some ms, depending on the device dimension and on the causes of the disruption. For the largest tokamak at present active, called JET, these times are around ms and likely the times for ITER will be between $1\,\mathrm{ms}$ and $10\,\mathrm{ms}$ [32]. The total plasma energy is given by two contributions: thermal and magnetic. In the thermal quench, only the first is lost but the second cannot be lost in such short times. The plasma tends to maintain all the energy enhancing the magnetic contribution, raising the current with a shrink of the current channel. Typically, the growth of the plasma current is in the order of $5-20\%$ of the initial current [2]. The magnetic energy of the plasma can be expressed as:

$$\varepsilon = \frac{1}{2}\mathrm{L}\mathrm{I}^2 \tag{2.6}$$

where L is the inductance and I the current. Given that the energy remains constant, a growth of the current implies the lowering of the inductance and thus the flattening in the current profile [33]. The thermal quench can occur in various phases, but typically two of them can be clearly seen [32], [34]: the first one is the energy redistribution within the plasma in the $q=2$ surface and then, after a delay $\tau_{(1-2)}$ the energy barrier breaks and thus the energy flows out of the plasma within a time τ_2. Usually these two phases overlap, but calculations and experimental data show that the $\tau_2 \sim \mathrm{O(ms)}$. In figure 2.4 a plot of the times $\tau_{(1-2)}$ and τ_2 for some devices. During the thermal quench, the main problem is given by the heat loads on the wall facing the plasma.

Current quench

This phase is the most harmful for the device stability. It's the time when the magnetic energy is lost through the current shut down. This is due to the rise in the plasma resistivity, given by the cooling of the plasma after the thermal quench ($\eta \propto \mathrm{T}^{-3/2}$). The current quench times are in the order of ms to $100\,\mathrm{ms}$ and are

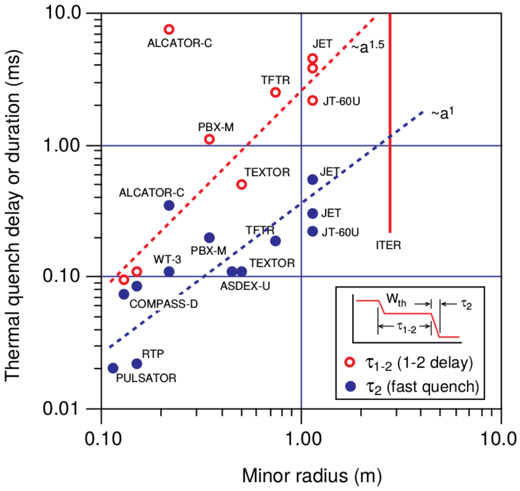

Figure 2.4: Thermal quench times for some devices. (Source [31])

linked to the time constant $\mathrm{L/R}$ of the plasma and to the device dimensions. This energy is lost by radiation and by currents in the vessel.

Halo currents Among the currents flowing through the vessel, they are mainly of two kind. The first type are the induced currents generated by the sudden variation of the magnetic flux. The other type is a peculiar feature of plasma magnetically confined and are due to the contact between the plasma and the first wall: if the resistivity of the plasma is higher than the surrounding structure, the current will flow preferentially here (see e.g. figure 2.5). These currents are mostly in the poloidal direction and are commonly called *halo currents*. They highly enhance the $\mathbf{j} \times \mathbf{B}$ forces.

Runaway electrons The current variation induces a strong toroidal electric field that can decouple electrons, accelerating them to relativistic velocities. These are called *runaway electrons*. As can be seen from figure 2.3, during the current quench there is still a good fraction of the pre-disruption current and this is maintained by the runaway electrons. The problem of this occurrence is that the cross section of the decoupling events increases with the velocity, thus they rapidly increase during time. The best way to avoid this problem is to suppress the first decoupled electrons and avoid the multiplication.

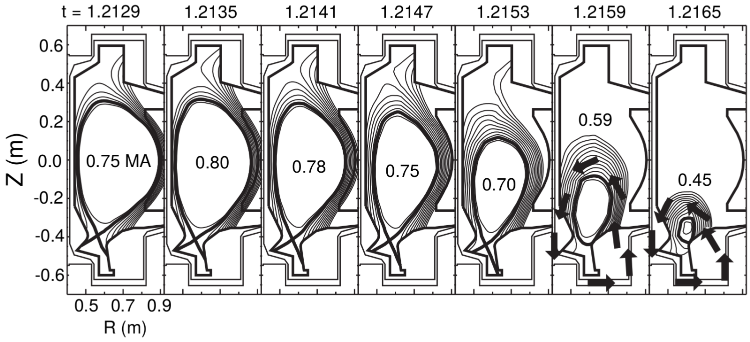

Figure 2.5: Magnetic flux reconstruction during a disruption in Alcator C-mod. The halo currents start developing at $1.2159\,\mathrm{s}$ and flow poloidally in the arrow direction (image taken from [31])

2.2.2 Precursor events

As said before, many instabilities can trigger a disruption but these can be grouped using the quantities describing the operational limit for a tokamak: n,q and β.

Density limit disruption

When the density is too high, the plasma edge can cool down through radiation and this implies a shrink in the current channel because the plasma resistivity rises where the temperature drops, as said before. Since the plasma current in the center is bounded to a certain value (limited by benign instabilities called *sawteeth*), the plasma profile will steepen and when this current gradient meets a rational surface a *tearing mode* is produced. This mode is really harmful for the confinement because magnetic islands are created, the magnetic lines reconnect and the particles can move more easily in the radial direction, thus the confinement drops. These islands move with a certain frequency around the surface where they originated from. For the stabilisation of this mode the currents induced in the vessel are really important. When the wall stabilisation falls and there are errors in the toroidal magnetic field, a *mode locking* can occur, the islands cease to rotate and there is no way to stabilize this mode, thus the discharge will shut down [31], [27]. The topology of a magnetic island is presented in figure 2.6. The mode where $q = 2$ is the one that usually trigger the instability.

q limit disruption

The q limit disruption is similar to the one started by the density limit. The main difference between the two is the precursor time: for density limit disruptions, the time is higher and thus the prediction can be done in advance. For the q

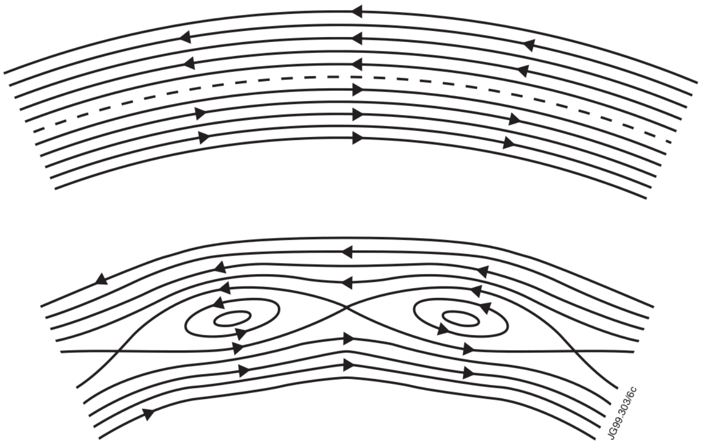

Figure 2.6: Topological view of a magnetic island (Source [27])

limit, the disruption begins when the value $q_a = 2$ is reached and an ideal kink is destabilised. When the mode locking starts, the thermal quench begins.

β limit disruption

This kind of disruption has been studied e.g. in reference [36]. The limit in β is given by a variety of phenomena that can develop, and each one is linked to a particular zone of the plasma. The limiting factors are the Mercier stability, the edge balooning stability and stability to external kink [28]. The Mercier limit is linked to the central current and pressure gradients [37] and is usually expressed using the curvature of the poloidal section, the balooning modes limit the plasma pressure in the outer half of the plasma radius [38] but the most restrictive is the limit due to the $n = 1$ external kink onset. All these limits can be written using the Troyon limit (eq. 2.3). When overpassed, there is initially an increase of edge activity, similarly to the density caused disruption and there are some modes that develop in cascade. As an example, when a *balooning mode* starts there is high mixing between the hot and the cold zones of the plasma and this supports the lost of thermal content by the core and thus the thermal and current quench occur.

Vertical displacements

Another condition that can start a disruption is the loss of the vertical position of the plasma, due to errors in the magnetic field control. In this case, the currents induced in the vessel tend to slow down the plasma movement but this isn't sufficient to stop it and when the $q = 2$ surface hits the wall a disruption starts. This events are called Vertical Displacement Events (VDE) and, if they occur before the thermal

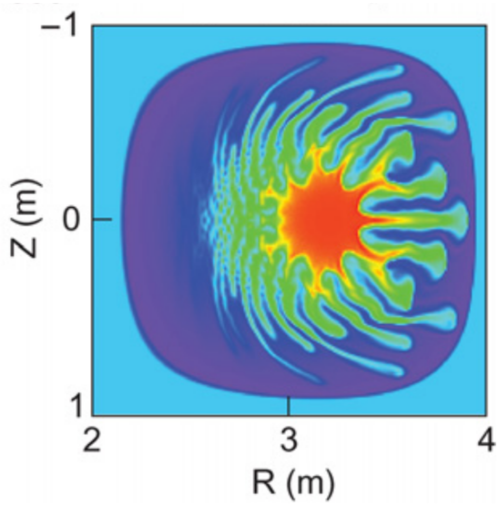

Figure 2.7: Poloidal section of a plasma where a balooning mode is developing. (Source [32])

quench, they are identified as 'hot VDEs', in fact the plasma still has all its energetic content. If the VDE begins during or after the thermal quench, it is called 'cold VDE' since the thermal energetic content has already been lost.

2.2.3 Effects

It's important to understand disruptions not only for their intrinsic physical interest, but also because of the effects that they have on the wall facing the plasma and on the vessel mechanical integrity. In a tokamak (and in the future fusion reactors) there are particular features that allow to focus the thermal deposition on restricted areas. During the thermal quench, most of the thermal plasma content will be deposited in a small area and in a short time, hence the materials won't withstand the heat load and then melt (see e.g. figure 2.8), causing clearly technical problems.

During the current quench, the induced and halo currents in the vessel would lead to strong forces on the vessel, since it is immersed in the magnetic field and hence a $\mathbf{j} \times \mathbf{B}$ force (in the radial direction) will stress the conductive components damaging them (see e.g. figure 2.9). Since changing the vessel is an unthinkable operation to do, it is necessary to avoid this kind of problem.

Another problem of the disruption are the runaway electrons. These are a problem since they grow in a cascade and, by colliding with the vessel, they cause high localised thermal deposition on the first wall. In figure 2.10 the impact of runaway electrons on carbon is shown.

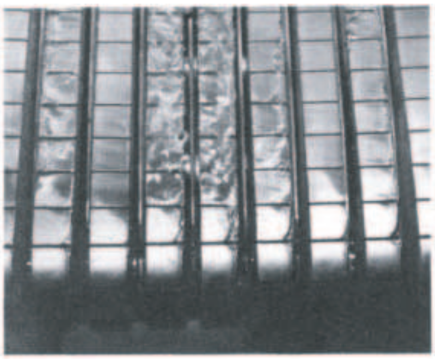

Figure 2.8: Effects of the thermal load on the beryllium first wall in JET (figure taken from [33])

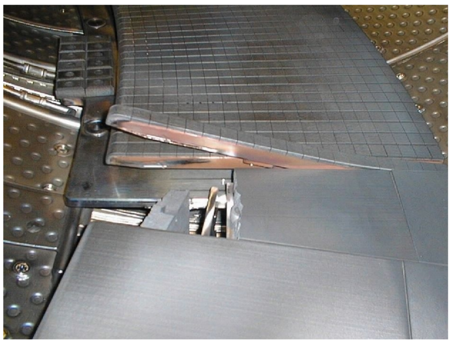

Figure 2.9: Effect of the $\mathbf{j} \times \mathbf{B}$ force on the vessel of Tore-Supra (figure taken from [33])

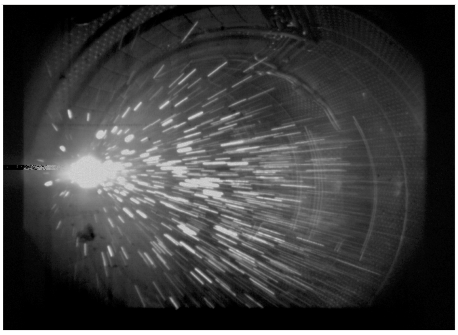

Figure 2.10: Impact of runaway electrons on carbon in Tore-Supra (figure taken from [33])

2.2.4 Causes

Identifying the initial cause of a disruption, the source of the instabilities described above that trigger a disruption, is not an easy task. This has been done in JET [39] and in ASDEX-Upgrade [40], firstly identifying the precursor activity that led to a disruption and then searching for what started this activity. This has been done analysing the data obtained from a single plasma *shot*, checking various real-time control systems and, if necessary, reading the experimental reports by the operators. Manual diagnosis was found out to be the better method, given that an automated analysis would have been unable to find control or sub-system failures.

In the end, the disruption were clustered with the precursor instability (table 2.1) and with problem that triggered them (table 2.2). The pattern followed by the discharges is shown in figure 2.11.

Type of physics problem	Label
General (rotating) $n = 1$ or 2 MHD	MHD
Mode lock	ML
Low q or $q_{95} \sim 2$	LOQ
Edge q close to rational (>2)	QED
Large sawtooth crash	SAW
Neo-classical tearing mode	NTM
Internal kink mode	KNK
Reconnection	REC
Radiative collapse ($P_{\mathrm{rad}} > P_{\mathrm{in}}$)	RC
MARFE	MAR
Greenwald limit (n_{GW})	GWL
High density operation (near n_{GW})	HD
Too low density (and low q)	LON
H-to-L back-transition	HL
Strong density peaking	NPK
Too strong internal transport barrier (ITB)	ITB
Strong pressure profile peaking	PRP
Negative central magnetic shear	MSH
Large edge localized mode (ELM)	ELM
Vertical displacement event	VDE

Table 2.1: Phenomena precursor to a disruption as found out in JET (Source [39])

Type of technical problem	Label
Impurity control problem	IMC
Influx of impurities	IMP
Density control problem	NC
Too much gas from gas injection module	GIM
No (effective) pumped divertor	DIV
Shape control problem	SC
Plasma too close to the wall	WAL
High recycling	RCY
Other real-time control problem	RTC
Emergency shut-down	STOP
Manual emergency stop by operator	SL
Wrong validated density for feedback	PDV
Magnetic signal(s) error	MAG
Reciprocating probe	PRO
Na influx by lithium beam diagnostic	LIB
Other diagnostic problem	DIA
Too little auxiliary power	AUX
Too little torque/rotation	ROT
Problem with neutral beam injection	NBI
Impurity release due to LHCD	LHC
Impurities from ICRH antennae	ICH
Problem with vertical stability control	VS
(Intentional) vertical kink	VSK
Temperature too high in VS amplifier	VST
Over-current in VS amplifier	VSI
Other failure of VS amplifier	VSA
Human error	HUM
Too fast a current ramp-up	IP
Other power supply problem	PS
Unidentified impurity influx (flying object)	UFO
Problems due to pellet injection	PEL
Impurity influx by laser ablation	ABL
No clear cause	NON

Table 2.2: Triggers for the disruption in JET (Source [39])

After this characterisation, some other physical quantities have been grouped as function of the disruption type. The typical time passing between the root-

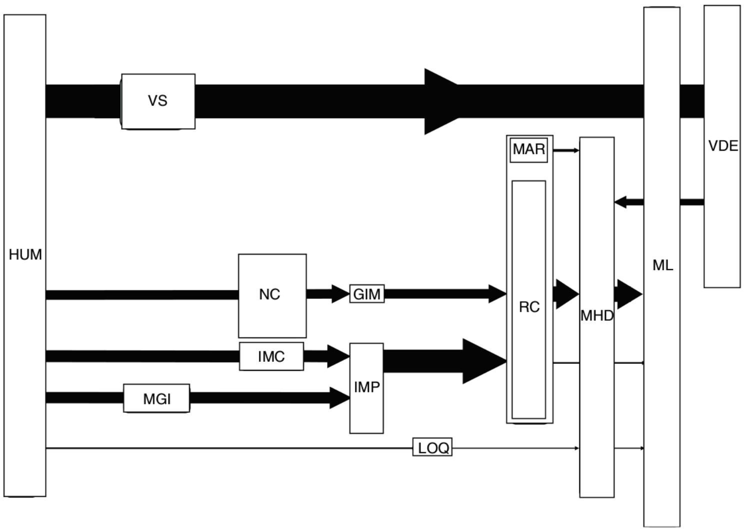

Figure 2.11: Schematic overview showing the path from the triggering cause to the disruption. The more the arrow is large, the higher is the probability of that path. The labels correspond to those in tables 2.1 and 2.2. (Source [39])

cause to the disruption has been evaluated and a particular fact has been found: fast disruptions classes provoke the highest forces. Concerning the heat loads, those depends on the disruption type. The three classes with the highest energy content are the ITB (Internal Transport Barrier), VDEs and also a number due to too fast a current rise, and the same three classes have the highest values of energy at the disruption times with respect to the maximum energy stored in the plasma. Disruptions at the Greenwald limit (GWL) are not well detected and tend to lower the plasma energy prior to the disruption, hence they have a smaller heat load. Differently, disruptions caused by the current rise are detected early, but the energy fraction remains high.

That work was carried out in order to improve the detection system of disruptions: if the system could tell not only whether the plasma might disrupt, but also which would be the root cause, then this would differentiate the mitigation systems and, nonetheless, a system able to detect only a peculiar type of disruption will be much stronger and simpler than a system able to detect all types of disruptions.

2.2.5 Avoidance and Mitigation of disruptions

Avoiding and mitigating a disruption is fundamental in order to increase the lifetime of a device. The best way to avoid a disruption is to slow down the evolution of MHD instabilities or stop them. This can be done heating the plasma around the rational surface [41] or controlling the plasma current ramp down in a proper way. Another method to identify an instability, involving neural network, is at present under studies.

Unluckily, some disruptions can't be avoided and thus mitigation becomes fundamental. In this way, the thermal and current quench are softened, reducing the heat load and the induced currents in the vessel. The ways currently under study are the mitigation using solid pellets, massive gas injection and also liquid injection. These methods are promising, also in reducing the runaway electrons current.

2.3 Operational limits for the RFP

In the RFP configuration, operational limits as described in section 2.1 have not been found. Some works have been carried out to characterise a density limit for the RFP configuration, and the results are summarized in reference [42] and, more recently, in [43]. In the following section, the term *fast termination* will be used, indicating a sudden and unpredicted termination of an RFP experiment.

In the RFP configuration, a real limit has never been found, although the points in the (n_G, n) plane seem to follow a Greenwald law. As can be seen in figure

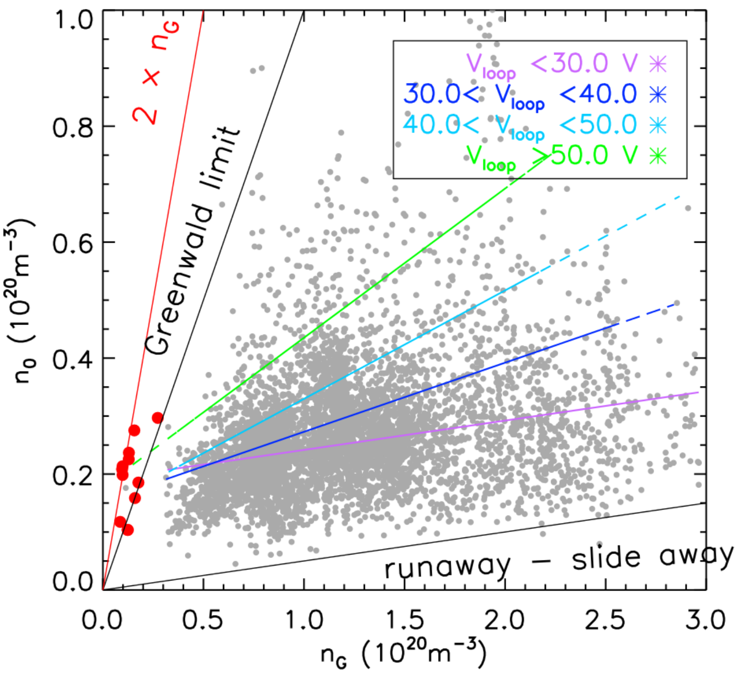

Figure 2.12: Data points in the (n_G, n_0) plane (Source [43])

2.12, the higher the loop voltage is applied, the steeper is the slope of n versus

n_G, thus with enough loop voltage the Greenwald limit can be overpassed. The points overpassing that limit are the ones in red. There is a difficulty in reaching this condition with high current and high density discharges, but no clear fast termination is seen and thus it is quite difficult to define a 'critical' density for the RFP. Since at present the RFP heating is ohmic, it can be shown that with larger input power larger densities can be accessed.

New results [43] supports a new interpretation of the density limit as due to critical MHD condition at the edge of the plasma. In that paper, the critical edge density value is $n_{\mathrm{edge}} \sim 0.35 n_{\mathrm{G}}$ while the central density follows the law $n_0 \propto B^{1.5}$. In the RFP, the edge limit has been extensively studied and it has been shown to be strictly related to a particular convective cell (associated to a formation of a particular configuration of radiation from the edge).

2.4 Conclusion

In this chapter, an overview of the *disruption* phenomenon in the tokamak configuration has been given. A set of operational limits (in density, q and β) has been treated, giving an overview of the freedom in the parameter choice and a brief explanation of what results in overpassing them. The development of a disruption has been explained, with its temporal subdivision, the effects, the causes and the methods to avoid and mitigate a disruption. Finally, a brief overview of the operational limits in the RFP has been given. The lack of an organic description of the fast terminations for the RFP and the strong analogy between a disruption and a relaxation event are the fundamental motivations for this work.

3

Diagnostic in RFX-mod

In this chapter an outline of the main diagnostic techniques and instruments used in RFX-mod will be presented. For the characterisation of the fast terminations, the measurements should have a high temporal resolution, given the time scales over which this phenomenon occurs. The relevant quantities are the temperature, the total radiation of the plasma, the density and the magnetic field (both mean field and its fluctuations). The techniques used in RFX-mod are all non invasive and consist in detecting and analysing the light coming out from the plasma in the case of the temperature and radiation, while an interferometer is used for the plasma density. The magnetic field (both mean and local) is measured using different set of particular coils.

3.1 Radiation

In order to measure the radiation of the plasma, an emission tomography system is used. Over different lines of sight (in the same toroidal position, but different poloidal positions), identified by the angle with the horizontal axis δ and the impact parameter p, the brightness is measured. The brightness $f(p, \delta)$ is defined as follow:

$$f(p, \delta) = \int_{LoS} g(r, \theta) dl \tag{3.1}$$

where LoS indicates the line of sight, dl is its differential element and g is the emissivity (the effectiveness of a material in emitting energy as thermal radiation). This last quantity is strongly dependent on the physical properties of the plasma, such as density and temperature. Measuring the brightness, it is possible to reconstruct the emissivity on the line of sight and then, making some physical assumptions (like assuming certain magnetic and pressure profiles), the profile of the quantities

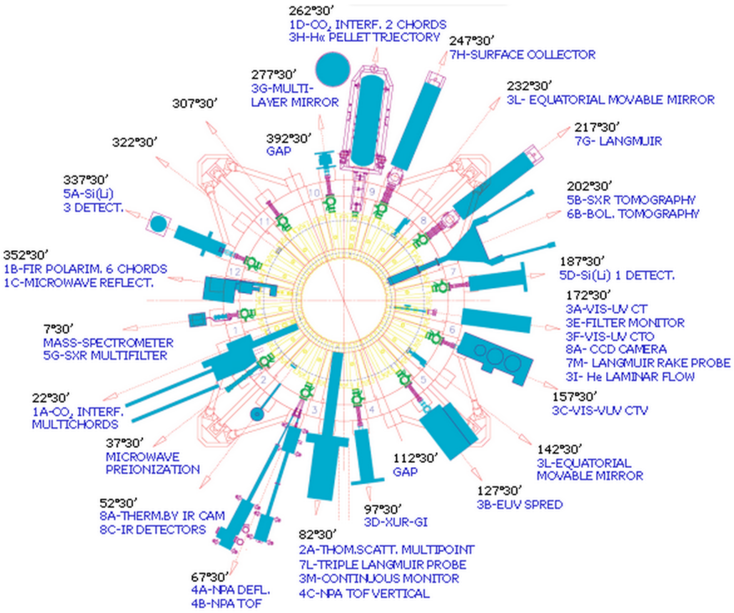

Figure 3.1: Image of the diagnostics installed in RFX-mod. (Source [24])

of interest. This method has a low spatial resolution: we have informations over the total LoS and not in each single point. Moreover, the detector has a finite 'cone' of sight and its axis is considered as the line of sight. The advantage of this system is the high temporal resolution which, for RFX-mod, is around $10\,\mathrm{kHz}$ for the bolometric system and $200\,\mathrm{kHz}$ for the soft x-rays (SXR).

By interposing filters between the plasma and the detector, different wavelength ranges can be detected. The filters used are made of beryllium and have different thickness, thus different bandwidths.

For further information about the radiation detection system, please look at [44] (the bolometric system of RFX-mod is the same of RFX).

3.2 Temperature

The temperature diagnostic (called DSXM) is basically a radiation detection system similar to the one presented above. It is composed by four ion implanted Si diodes which are covered by $4\ \mathrm{Be}$ absorbers of nominal thickness $55\,\mu\mathrm{m}$, $84\,\mu\mathrm{m}$, $146\,\mu\mathrm{m}$ and $299\,\mu\mathrm{m}$. These dimensions are chosen in order to filter the light from the plasma, in particular the radiation due to the C and O radiation lines. The four LoSs of the diodes see the center of the plasma and even if they don't overlap perfectly the results proved to be very reliable since in the core of RFX the profiles change on a longer spatial scale [45].

By combining the SXR brightness from pair of lines of observation (which are overlapped) and using the two-foil technique, electron temperature can be deduced [47]. If we consider two brightness signals coming from two filters with different thickness (t_1 and t_2, with $t_1 < t_2$), the ratio R of these signals is strongly dependent from the temperature:

$$R = \frac{f(T_e, n_e, t_1)}{f(T_e, n_e, t_2)} = R(T_e) \tag{3.2}$$

Since the impurity radiation lines are filtered, R depends mainly on the highest electron temperature along the LoS. A first approximation is to locate this temperature in the middle of the LoS, but more accurate localisation can be done knowing the geometry of the equilibrium magnetic surfaces, assuming that the temperature is constant along a flux surface, the surfaces are axisymmetric and circular and the temperature decreases monotonically from the core to the edge. By comparison with the Thomson scattering diagnostic [46] (not detailed here), which has a higher spatial localisation but a lower temporal resolution, it is seen that the DSXM diagnostic smooths the electron temperature for small structures. The acquisition frequency is some kHz. The temperature measurements unit will be eV, following the following conversion law:

$$T(\mathrm{K}) = \frac{e}{k_B} T(\mathrm{eV}) \tag{3.3}$$

The details presented here are mainly extracted from [45].

3.3 Density

The density measurement system is fundamentally different from the radiation and temperature ones. It consist of a couple of two-color $\mathrm{CO_2}$ interferometer with a total of 16 chords (the analogue of the LoS). The main wavelength is $\lambda = 10.6\,\mu\mathrm{m}$, the one of a $\mathrm{CO_2}$ laser. The two interferometer will be called module A and B. The diagnostic has a bandwidth of more than $1\,\mathrm{MHz}$ and an accuracy of $1.3 \times 10^{18}\,\mathrm{m^{-2}}$ for module A and $4 \times 10^{18}\,\mathrm{m^{-2}}$ for module B. These measurements are on a chord and this justifies the fact that the density is measured in $\mathrm{m^{-2}}$.

For further informations about the density diagnostic of RFX-mod, please look at [48], [49] and [50].

3.4 Magnetic measurements

The electromagnetic measurements are one of the most important set of diagnostics of RFX-mod and they are displaced all over the vacuum chamber, as shown in figure

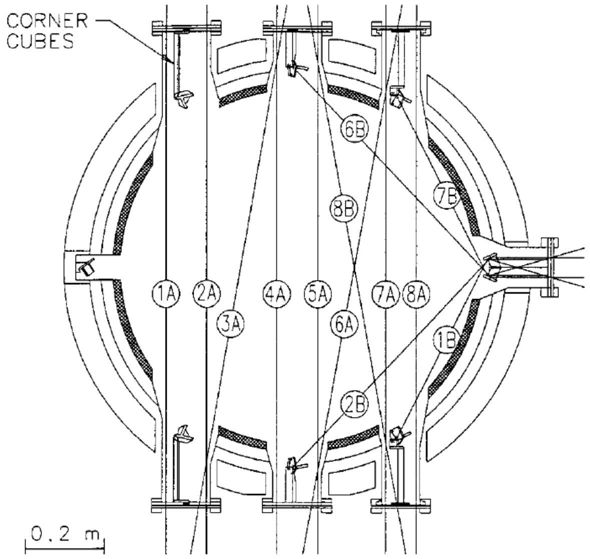

Figure 3.2: Design of the density interferometer for RFX-mod. The chords not working are not displayed (Source [50])

3.3. These are based mainly on the physical principle of induction: the voltage measured at the extremes of a coil can give informations about the current on the coil and hence on the magnetic flux variations over time. With an integration, the magnetic field can be calculated. The bandwith ranges from the steady state to hundreds of MHz, depending on the system.

There are many kinds of coils used in RFX-mod to measure the electromagnetic quantities:

- $\mathrm{V}_{\mathrm{loop}}$: these are coils with a single winding wrapping the vacuum vessel both around toroidal and poloidal direction. Integrating the signal, the magnetic flux inside the coils is measured. In RFX-mod 8 toroidal coils and 5 poloidal coils are installed;

- *Rogowski coil*: this type of coils is made of a high number of windings with a small section with respect to the total length (see e.g. figure 3.4). A conductor that short-circuits the two ends is needed in order to avoid the influence of the flux variation orthogonally to the coil. These are usually used to measure the current with formula 3.4, where μ is the resistivity and n the number of windings). RFX-mod is equipped with 6 Rogowski coils;

- *partial poloidal coils*: these are used to measure the flux variation in a partial poloidal sector. In RFX-mod there are eight poloidal coils in four toroidal positions (see figure 3.5) and with these the halo currents can be measured;

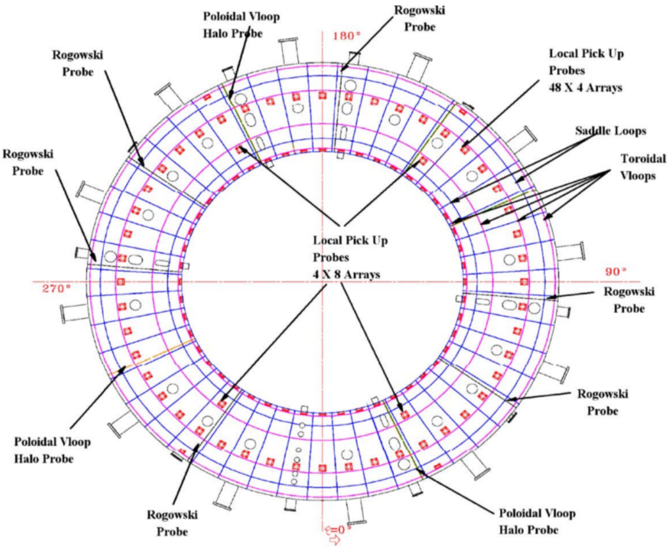

Figure 3.3: Sketch of the electromagnetic diagnostics in RFX-mod (Source [51])

$$I = -\frac{1}{n\mu A}\int_{\mathrm{t}} \mathrm{Vdt} \qquad (3.4)$$

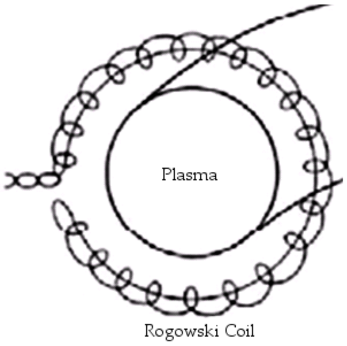

Figure 3.4: Sketch of a Rogowski coil

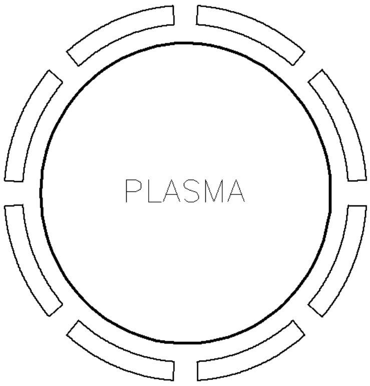

Figure 3.5: Sketch of the partial poloidal coils in a single toroidal position

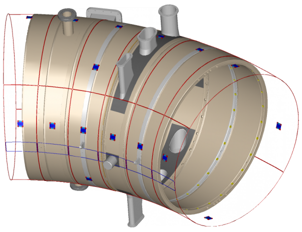

Figure 3.6: Image showing the radial magnetic sensors (in red in the figure)

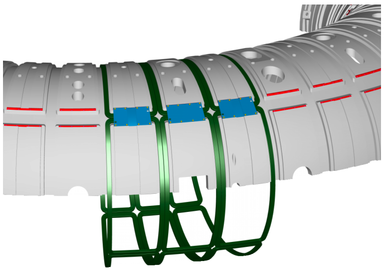

Figure 3.7: Sketch of the active saddle coils design

- *radial sensors*: in order to measure the radial component of the magnetic field, that, in a perfect axis-symmetric condition, should be zero everywhere due to the condition $\nabla \cdot \mathbf{B} = 0$ applied in a toroidal geometry, a set of saddle coils are used. There are a total of 4×48 coils (four in the poloidal direction). These coils are designed in order to show no area in the poloidal and toroidal section, thus measuring only the radial one. The importance of this measurement system is related to the feedback-control system of RFX, that has been developed to control the radial magnetic field all over the plasma surface. Figure 3.6 shows the coils installed in RFX-mod and 3.7 the graphical design of the active saddle coils, the main components of the feedback-control system;

- *local field coils*: this system is composed of a set of small-sized probes with two orthogonal solenoids. The dimensions are important because the inside field should be assumed as constant. These are quite difficult to build because they should be included in amagnetic materials and with a really small mechanic tolerance, in order to have a high precision in their position. In figure 3.8 a photo of one of such coil is shown. There are a total of 192 coils all over the vessel and 32 coils near selected diagnostics. This particular type of probes is used in RFX-mod to measure the toroidal and poloidal magnetic field fluctuations. A particular note should be made about the periodicity of these coils: the magnetic field in the RFP and tokamak configurations are subjected to particular Fourier modes over the toroidal and poloidal positions, characterised respectively by the numbers (m, n) (as explained in section 1.3.3). According to the Sampling theorem [53], if a number of probes lower than half the Fourier mode number is used, aliasing phenomena occur. In addiction, the intrinsic periodicities of the machine can give origin to aliasing phenomena, thus not all the diagnostic location periodicities are acceptable.

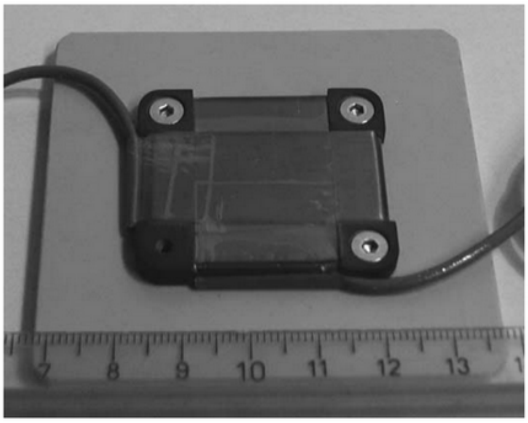

Figure 3.8: Photo of a local coil mounted in RFX-mod(Source [52])

> For RFX-mod, 48 probes in the toroidal direction and 4 probes in the poloidal direction are used, such as the modes with $0 < |n| < 23$ and $m = 0, 1$ can be correctly measured. For further technical details of the local coils, please look at [52]

In the end, there are 739 signals from the magnetic measurement system.

SGPR (*Sistema Generale di Protezione Rapida*) In order to avoid damages to the electrical implant of RFX-mod, a system called SGPR has been developed and is always active on RFX-mod experimental session. It has five protection levels, ranging from a condition where the electric supply is not stopped but the subsequent shot cannot be executed if the problem is not solved and arriving to a condition where all the supplies are shut down instantaneously. A real time system is responsible for the controlled shut down of the power supplies. SGPR is in communication with many system (the toroidal system, the poloidal system, etc.) and when one among these has a supply problem, SGPR sends signal to the others in order to shut them down.

3.5 Conclusion

In this chapter an overview of the main diagnostics used in the rest of the thesis can be found. The methods to measure the most important parameters of the plasma have been given: for the radiation detection, the emission tomography system has been shown and the electron temperature calculation has been explained; an overview of the interferometer used to estimate the density has been carried out and the magnetic measurement system has been shown in its main features, focusing on the mean field diagnostics (which are the so-called V_{loop} and the Rogowski coils) and on the local field diagnostics, both radial with the saddle coils system and on the other two directions with the local field coils. Particular attention is given to the magnetic modes fluctuations and the signal analysis necessary to correctly interpret the data. In the end, a brief explanation of the SGPR system of RFX-mod is given.

4

Studies of single disruptive discharges

All the work have been done following at first the description of how a tokamak disruption develops and searching for similar events in the RFP, that are usually called fast terminations. Due to the similarity between the two phenomena in the two different configuration, the same term will be used in the following for both the configurations.

In this chapter some shots taken as references for a disruptive discharge and their properties are shown. In the first part the method to create a database and an explanation of the problems encountered in doing an automatic analysis is presented. These problems and the need to understand how a disruption develops resulted in a study of some shots with robust measurements before going further with all the shots classified as disruption. Along with the temporal evolution of the parameters, operational spaces for the shots are shown and commented.

4.1 Creation of a disruption database

The range of shots from which extract the disruptions started from number 15308 and arrived to 38200. The former number labels the first shot of the rebuilt RFX-mod device and with the active control system, while the latter is the last pulse run at the time of the database creation (June 2015). The most important parameter in choosing whether a shot is a disruption or not is the current: this is a trustful value always measured during a shot, thus it can be used with less concern with respect to others parameters used, such as the electron temperature T_e.

The parameters calculated and studied in order to find the disruptions were the following:

- Maximum current (I_{max}): the shots with a current lower than $300\,\mathrm{kA}$ have not been considered. In this work, the purpose was to do a first analysis of the disruptions in RFX-mod, thus only the more interesting one (at higher currents) were studied. This range is quite broad anyway, in fact the shots found have the current that ranges from $300\,\mathrm{kA}$ to $2\,\mathrm{MA}$ (the maximum for a RFP discharge in RFX-mod). Moreover, the device can be operated also as a tokamak and these kind of discharges were avoided using this lower limit because the currents of the tokamak are lower than the threshold used;

- Poloidal voltage (V_θ^{max}): the limit on the poloidal voltage was a way to remove, at first order, all the shots which didn't end with a disruption. Because of the well-known Lenz law, the current quench induces a poloidal voltage rise. If this value is lower than a given limit, this means the quench wasn't so fast and thus this discharge wasn't interesting for this work. The lower limit in V_θ^{max} was put to $15\,\mathrm{V}$;
- Quench parameter (τ): before doing a study over all the discharge range, a look at single disruptive discharges has been taken. It has been noted that, for the disruptions with the highest currents ($\sim 2\,\mathrm{MA}$), the current quench (evaluated as the time the current needs to fall from 70% to 10% of the maximum current and indicated as Δt_{70-10}, see figure 4.1) had values lower than $12\,\mathrm{ms}$. It has been decided that all the discharges with a scaled time of the current quench lower than that value could be identified as disruptions. In the end, the following relation must be fulfilled:

$$\Delta t_{70-10} < \frac{I_{max}}{2\,\mathrm{MA}} * 12\,\mathrm{ms} \tag{4.1}$$

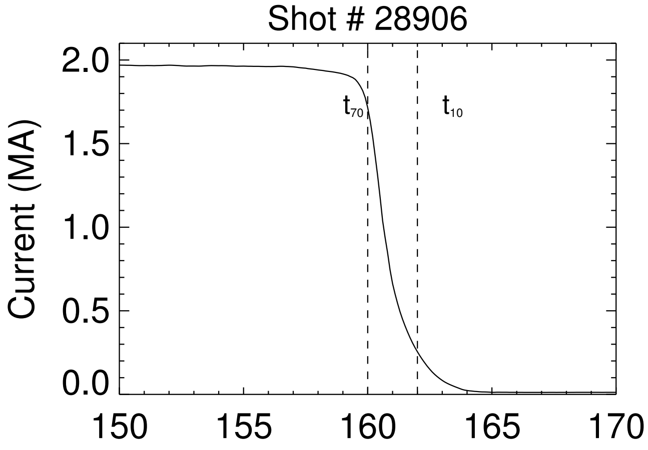

Figure 4.1: Zoom on a disruption CQ, where the t_{10} and t_{70} times are labelled

A look at the discharges logbook has also been taken, in order to understand the conditions under which a disruptive shot runs. This work can be useful for studying a single shot (as will be done later) but it wasn't used for the statistical study. Obtained the disruptive discharges with the method described above, sometimes one of them wasn't recognised as a disruption by the operator. This implies that an independent identification of the disruptions on the logbook couldn't be done.

With the criteria exposed above, a total of more than 330 disruptions have been found.

4.2 Parameters of the disruption

A set of fundamental properties of the disruption has been found, in order to characterise these particular shots and understand their general behaviour.

Pre-disruption (PD) current I_{PD} The current before the disruption (in this work called I_{PD}) is an important parameter in the study of the disruption. It is often used in the characterisation of a tokamak disruption [54]. It was quite complex to find automatically this parameter because of some cases where the current was widely oscillating and thus a good determination of the desired value was hard to find. The current signals of the selected shots have been singularly seen, in order to determine I_{PD} and the time where this happens. Generally, from now on, the time t_γ is the one where the current has the $\gamma\,\%$ of the I_{PD} during the ramp down.

Current quench (CQ) An important parameter that classifies a disruption is the quench rate, defined as follows:

$$\mathrm{QR}_{70-10} = 0.6 \cdot \frac{I_{PD}}{\Delta t_{70-10}} \tag{4.2}$$

it is a quantity which identifies the current variation during the current quench;

Temperature quench (TQ) In the case of the tokamak, the temperature is really stable and has no high fluctuations. In the RFP, this is no more true because of the DREs and the relaxation events, that make the temperature oscillating (up to 50% of the maximum) and hence the thermal quench is no clearly seen as in the tokamak. The idea in the thermal quench determination is the following: either the temperature has a clear thermal quench either the 'last fall' of a DRE event is considered as the quench. In some cases, after the last DRE from the flattop, the temperature fell slowly but still oscillating as if some relaxation events were occurring. All this variability and type of events brought to the decision of doing a manual analysis of the shots, looking at the temperature signals and finding manually the thermal quench.

Relevant times the three quantities described above allowed to find six important times in the characterisation of the disruption, which are labelled as follows:

pre TQ TQ start pre CQ TQ end start CQ CQ end

these times are not necessarily in this order,but for every shot the pre TQ was at the beginning and the CQ end at the end. The pre TQ is $10\,\mathrm{ms}$ earlier than the TQ start, the pre CQ is the time where the pre-disruption current is found. For the shots where the thermal quench couldn't be found, there are no TQ start, TQ end and pre TQ but the others are present. For each shot, these time values were used as reference to evaluate the meaningful quantities and these six times have to been taken as references for the results that will be presented. The decision of considering these times not in the sequential order but in this order is due to the fact that the study aimed to analyse how a discharge behaved in similar conditions, not in a sequential time order.

4.3 Problems in doing an automatic analysis

An explanation of the problems involved in doing an automatic analysis of a shot must be given. A lot of signals flow out from the diagnostic system of RFX-mod and a large temporal range has been evaluated (there is a difference of ~ 20000 between the last plasma shot considered and the first one and this implies that the oldest has been done more than 10 years ago).

The signals used for the analysis are the one validated by the responsible of the diagnostic. Unfortunately sometimes all the signals are not valid and thus one has to be chosen, whilst it can't be useful, hence this is not a warranty of the signal goodness. For the temperature, the signals coming from the filters couple $37 - 75$ (whose filters dimension is respectively $55\,\mu\mathrm{m}$-$84\,\mu\mathrm{m}$) were preferentially used, above all for their capability of detect the SXR light also with low intensities (at the end of the thermal quench). If those signals were not useful or could not be used, the couple $150 - 300$ (whose filters dimension is respectively $84\,\mu\mathrm{m}$-$146\,\mu\mathrm{m}$) was considered. For the density, the signal of the chord 4 is usually the one validated, but sometimes also the chord 5 is used.

The magnetic system is really stable and, apart from mode calculations problem, the signals were always valid.

Failure of the diagnostic This large temporal range implies that some diagnostic could have had some problems and thus some data could not be retrieved. In figure 4.2 the temperature is presented, as an example for the cases where the thermal quench could not be found because of a failure of the diagnostic. As the figure shows, the signals are too low and, since the electron temperature is found with a ratio between the two, the measure are not trustful.

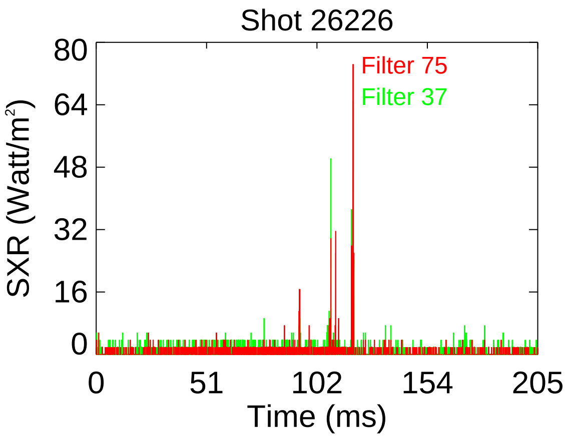

Figure 4.2: Bad signals coming from the DSXM diagnostic system, that prevent the thermal quench determination.

Saturation Another problem that sometimes occurs is the saturation of the signal. Taking in consideration the temperature again, one of the two signal can saturate and thus the ratio of the signals is no more trustful. This saturation is due to the high quantity of SXR radiation which of course does no only depend on the temperature but also on the density.

Fringe jump A problem that concerns density is the so-called *fringe jump*. The density is measured with an evaluation of the phase difference between two rays. The interferometer is highly sensible to mechanical movements and these can occur during a disruption, due to the $\mathbf{j} \times \mathbf{B}$ coupling. This implies a wrong measurement of the phase difference and thus a wrong density estimation. This is easily seen in figure 4.4. As can be seen, there are problems in setting the zero of the signal. Usually, the zero is at the end because of the fact that the density without the plasma is surely zero. In other cases, due to the jump, the zero has to be taken at the beginning. The main problem for the work done is that the density measurement is no longer valid where the disruption occurs.

Apart from these problems that are relative to the diagnostic system, in the case of the temperature sometimes it was impossible to find a thermal quench. The

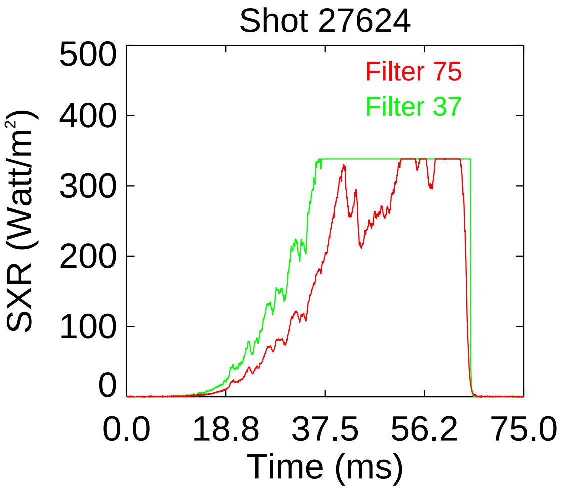

Figure 4.3: An example of the saturated signal from the DSXM diagnostic system.

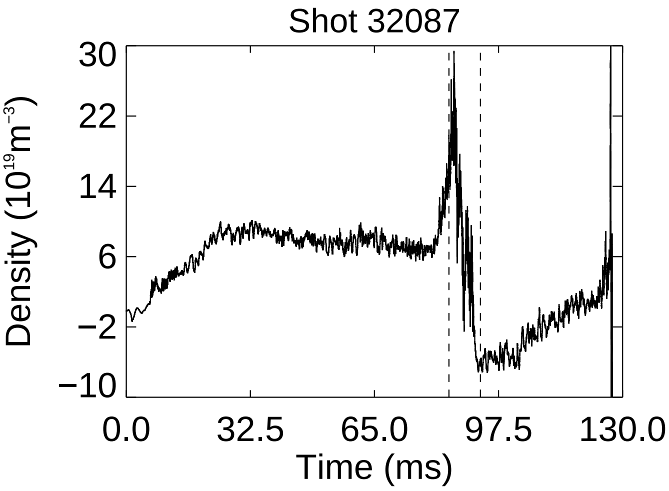

Figure 4.4: Density signal where the fringe jump occurred (inside the dotted lines).

temperature wasn't decreasing and thus a thermal quench couldn't be found. This is due to a failure in the evaluation of the temperature because a thermal quench should be seen every time, also if contemporary to the current quench. There are cases (like figure 4.5) where a thermal quench couldn't be found even if the signals were available. A total of 133 discharges have no thermal quench signals.

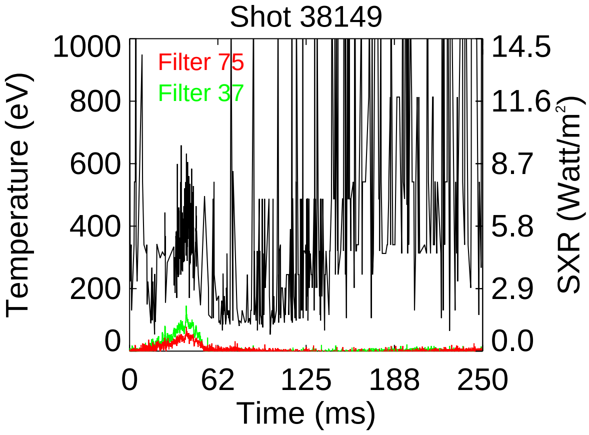

Figure 4.5: Shot were a thermal quench was impossible to find although the signals were available. On the left there is the temperature axis, on the right the SXR axis

4.4 Single shot analysis

Before studying the statistical behaviour of the discharges, a set of 8 shots have been selected and singularly studied, in order to see how a typical RFP disruption behaves and its general trends. In table 4.1 the relevant parameters of the selected discharge are presented:

Shot #	I_{max} (MA)	I_{PD}/I_{max}	Length (ms)	QR (MA/ms)	TQ time (ms)
28906	1.981	0.991	164.90	0.620	3.003
29137	1.826	0.784	114.2	0.277	12.268
29155	1.734	0.840	107.7	0.213	10.126
32414	0.573	0.835	131.15	0.198	1.307
36204	1.541	0.859	169.00	0.429	6.923
36522	1.607	0.957	163.40	0.528	9.861
36739	0.979	0.996	39.202	0.354	1.766
37504	1.334	0.919	212.76	0.420	3.581

Table 4.1: Table with the main parameters of the selected shots.

In the plot that will be shown, when in the legend the symbol * appears it means that the relative value is out of the range used in the plot. These points have not been included because meaningless and because enlarging the used ranges would have had the effect of making the too little to be seriously studied.

In this thesis, the density will be presented normalised to the Greenwald density n_G. This one is evaluated with formula 2.1: $n_G = \frac{I_P}{\pi r^2}$, where I_P is the plasma current and r the radius of the last closed surface. As figure 4.6 shows, during a disruption the plasma shape isn't constant and thus the Greenwald density has to be calculated at each time.

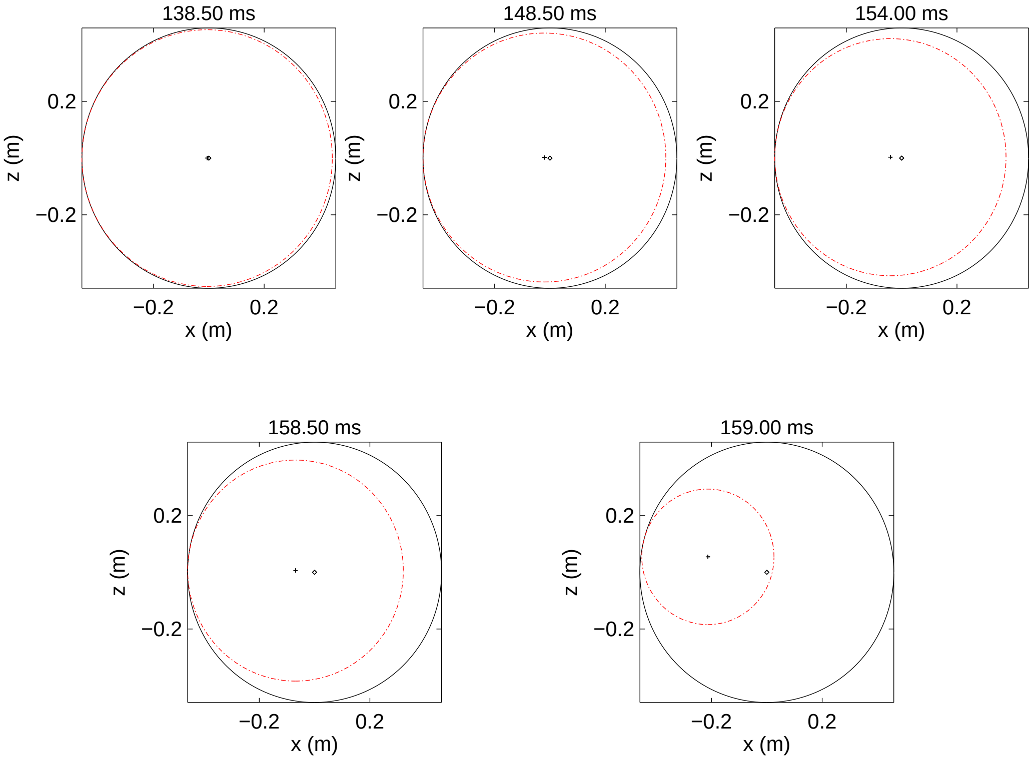

Figure 4.6: Section of the plasma during a disruption. The red and dotted line is the position of the last closed flux surface.

The colors that will be found in the plot can be read with the legend below:

Pre TQ Start TQ Pre CQ End TQ Start CQ End CQ

28906 This shot has the highest current among all the selected shots. It had a really good flattop, with a really stable current, and then suddenly at $160\,\mathrm{ms}$ the disruption occurred, as can be seen from figure 4.7. The discharge developed a QSH with definite DREs. At time $78\,\mathrm{ms}$ a pellet was shot inside the plasma and it changed a little the growth of the magnetic modes. After this injection, the plasma changed its properties: the Θ parameter decreased and the α parameter increased, flattening the current profile, and the change of the plasma properties was probably responsible of the degradation of the plasma confinement . In fact, at around $146\,\mathrm{ms}$ the TQ started, the density rapidly increased and then a little later the SGPR protection system shut down the plasma in order to protect the device, causing the CQ. In figure 4.8 we can see that after the start of the TQ the density raised to dangerous values and probably induced the disruption. From the figure 4.12, the stop of the LP around position $\approx 110\,°$ seems to be connected with the growth of the density, thus an enhanced plasma wall interaction can be the cause of this density puff. The magnetic parameters, such as F and q_a (figure 4.9, 4.10 and 4.11) show that up to the end of the TQ they weren't in a critical area, but with the end of the current quench the field reversal has been lost. From figure 4.13 we can see that the path followed after the pre TQ had a lower Θ_0 parameter compared to the path followed before the disruption and the α parameter increases, broadening the plasma current channel during the disruption.

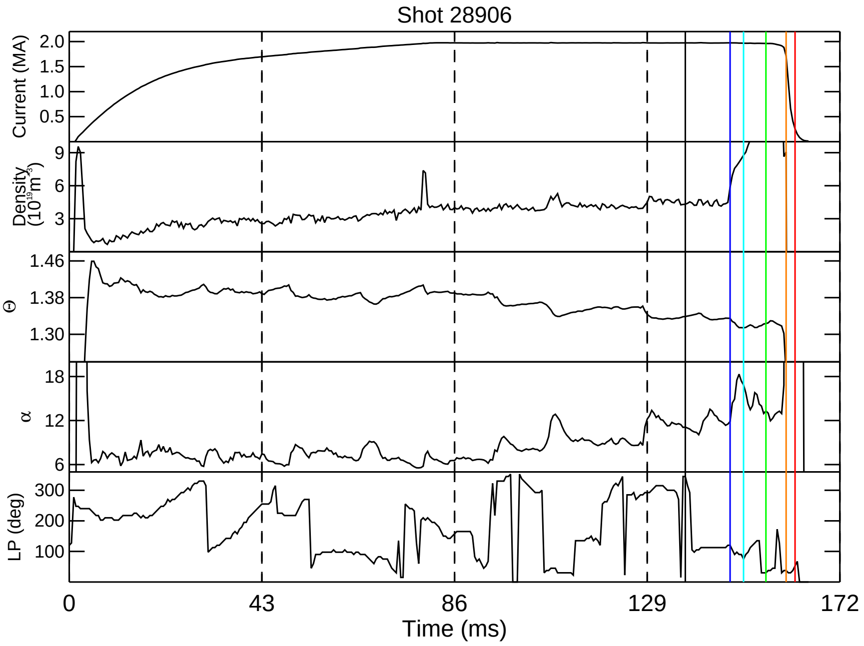

Figure 4.7: Relevant quantities for shot 28906

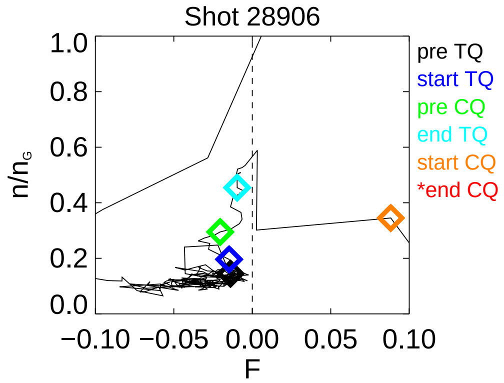

Figure 4.8: Path in the space (F,n/n_G) for the shot # 28906

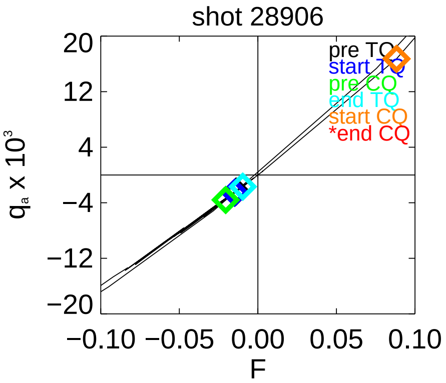

Figure 4.9: Path in the space (F,q_a) for the shot # 28906

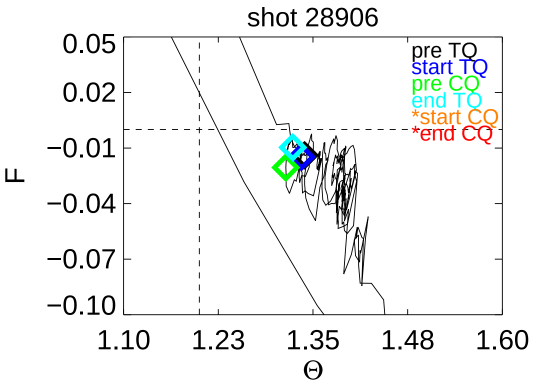

Figure 4.10: Path in the space (Θ,F) for the shot # 28906

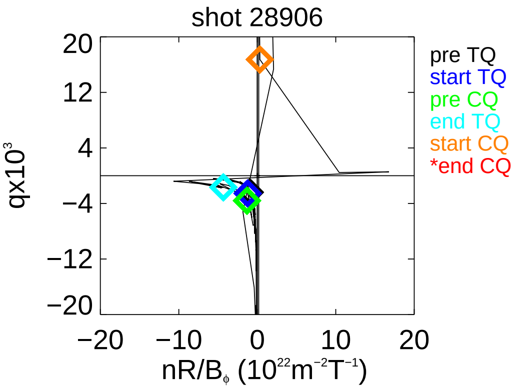

Figure 4.11: Path in the space ($\frac{nR}{B_\phi}$,q_a) for the shot # 28906

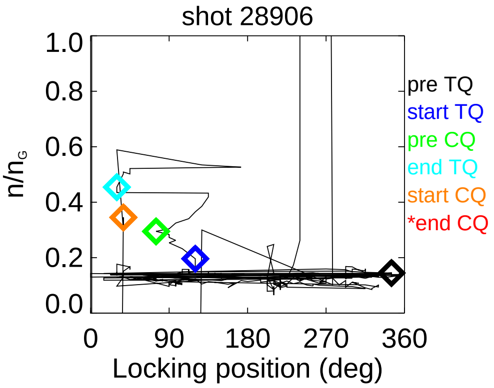

Figure 4.12: Path in the space (LP,n/n_G) for the shot # 29806

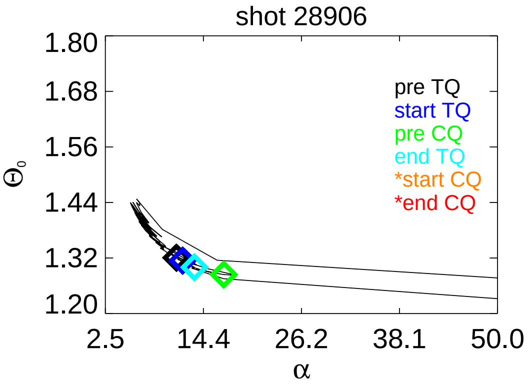

Figure 4.13: Path in the space (α,Θ_0) for the shot # 29806

29137 The experiments in this session were devoted to study high performances discharges and the F parameter was feedback controlled.

Looking at image 4.14, it can be noted that the discharge run a good ramp-up and flattop phase (although a small current increasing is always present up to the maximum). The LP is constantly moving, thus indicating that there is no wall locking of the MHD modes (except for the last part, at around $100\,\mathrm{ms}$. A QSH state was beginning but, at $70\,\mathrm{ms}$ a dramatic event occurred, in fact a lot of parameters had a sudden change in their behaviour. The temperature drops, the Θ parameter control is lost, α start increasing enlarging the current channel, F and q grow up to a positive value but then they go back below 0. The most dramatic change is the density, in fact from $70\,\mathrm{ms}$ on the normalised density keeps a value of 0.5 until the end of the discharge. When the density increased, the $\mathrm{V}_{\mathrm{loop}}$ dropped but the poloidal voltage increased. After this critical event, the discharge continued anyway for $40\,\mathrm{ms}$, having weak relaxation events and keeping the F parameter below 0. The current never keeps constant, after the event at $70\,\mathrm{ms}$ the current decrease and consequently also the magnetic energy decreases, incurring in the CQ at around $110\,\mathrm{ms}$.

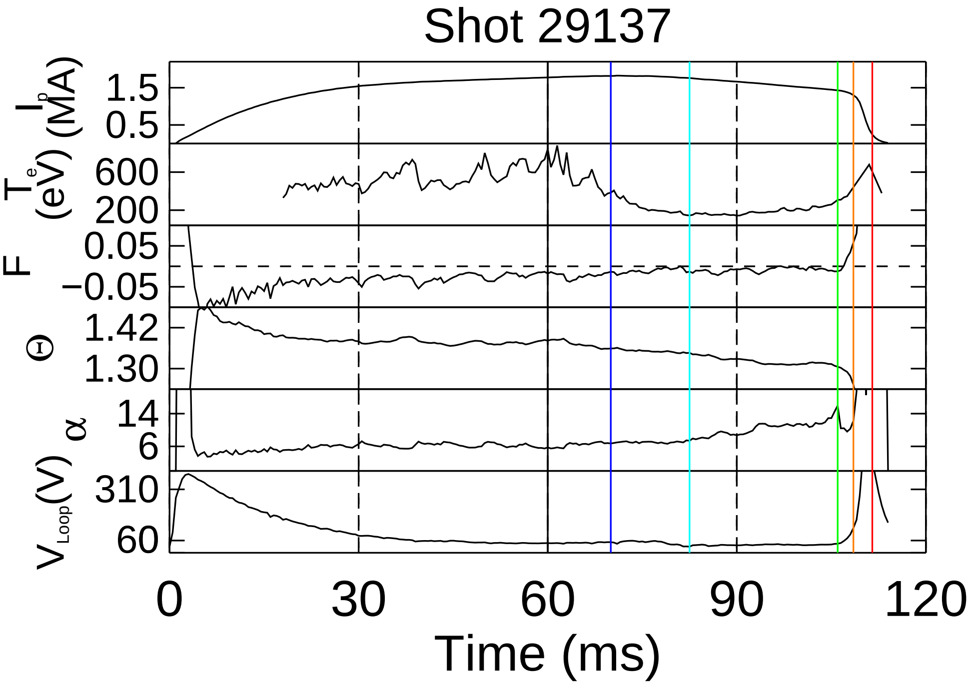

Figure 4.14: Relevant quantities for shot 29137

As in the case before, from figure 4.15 it can be seen that at the pre TQ the density starts increasing up to values of $0.5\,n_G$ at the end of the TQ without losing the reversal of the magnetic field. This lost is apparently not dependant on the LP, as figure 4.19 shows and happens at the start of the current quench, as in the case before (as can be seen in figures 4.16 and 4.18), while the trend of the α parameter is quite strange, as figure 4.20 displays: α initially increases up to the end of the TQ, then it decreases and at the start of the CQ begins an uncontrollable growth. This enlargement and shrinking of the current channel is a particular feature of this discharge. In figure 4.17, we can see that the Θ parameter starts decreasing at the beginning of the disruption.

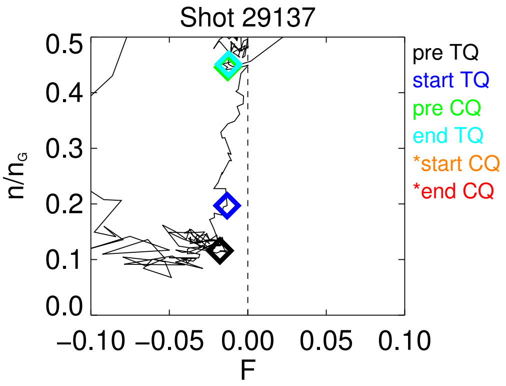

Figure 4.15: Path in the space (F,n/n_G) for the shot $\#29137$

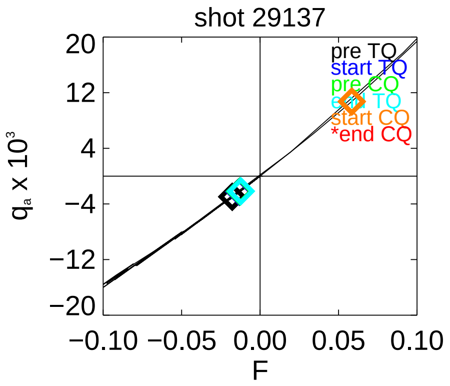

Figure 4.16: Path in the space (F,q_a) for the shot $\#29137$

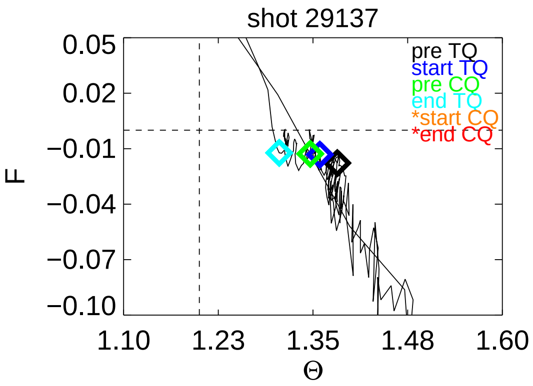

Figure 4.17: Path in the space (Θ,F) for the shot $\#29137$

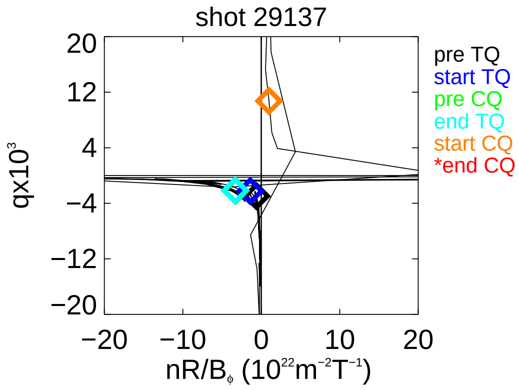

Figure 4.18: Path in the space ($\frac{nR}{B_\phi}$,q_a) for the shot $\#29137$

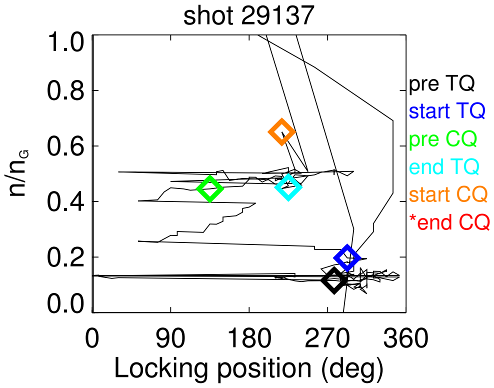

Figure 4.19: Path in the space (LP,n/n_G) for the shot #29137

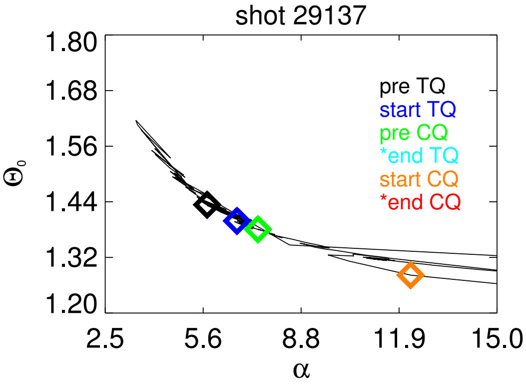

Figure 4.20: Path in the space (α,Θ_0) for the shot #29137

29155 In this session, as in the one for the shot 29137, the aim was to study high performance discharges. Along with a feedback control of the F parameter, there was gas puffing during the flattop phase.

Similarly to the previous discharge, the TQ is quite early, at around $50\,\mathrm{ms}$ and it happens simultaneously with the development of a QSH state and a DRE event, as figure 4.21 shows. As in the other cases, with the DRE event there is a growth in T,K,Θ and a decrease in α but with the high loss of the thermal content it seems that the magnetic configuration is no more optimal to the discharge, the density and the SXR grow but the discharge carries on for other $40\,\mathrm{ms}$. At around $85\,\mathrm{ms}$ another drop in the $B_T(a)$ and in F is seen but the density doesn't stop increasing. The position of the mode locking doesn't seem to be linked to the density increase, although when the thermal energy is lost the LP seems to slow down its motion. In the end, the decrease of the current and the lowering of the magnetic energy bring to the CQ. Looking at the operational spaces, from figure 4.22 the high value of the density parameter is seen well before the the disruption start, in fact the density increases up to an apparent sudden decrease. This is not a trustful measure of the density, it is a result of a fringe jump that occurred in this shot, in fact in figure 4.11 a point lies in the second quadrant, a zone possible only if the density is negative and this has obviously no physical meaning. From figures 4.23 and 4.24 we can see that the reversal is lost already at the pre CQ time. The α parameter at the pre TQ time is already quite high and it rapidly continues its growth, as figure 4.27 shows.

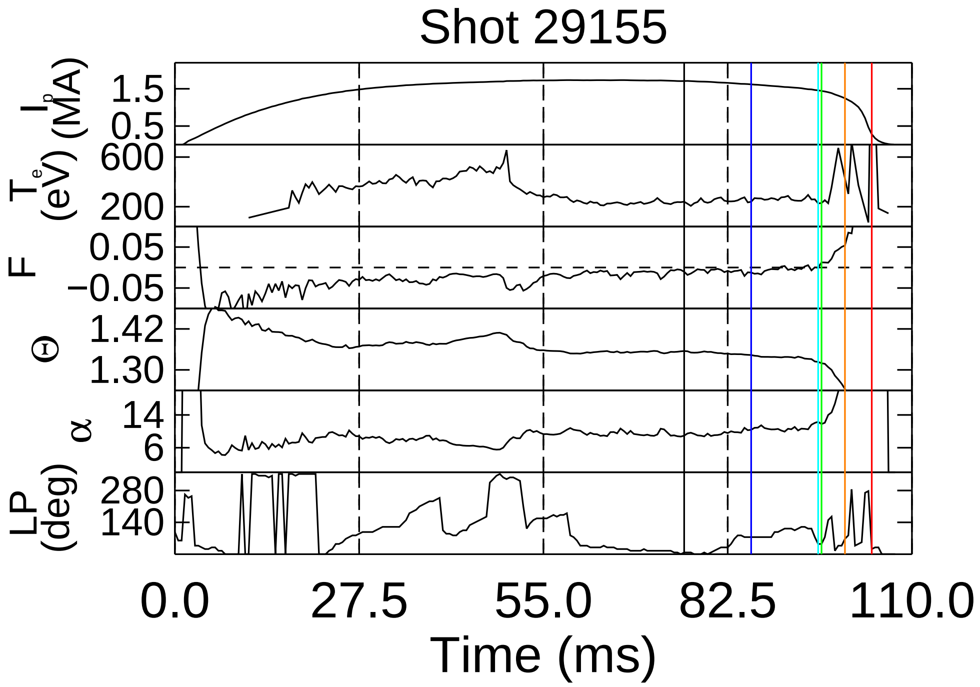

Figure 4.21: Relevant quantities for shot 29155

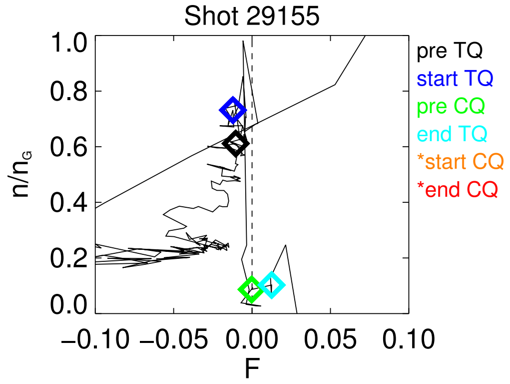

Figure 4.22: Path in the space (F,n/n_G) for the shot #29155

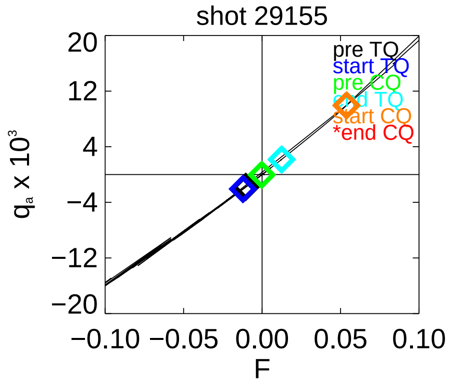

Figure 4.23: Path in the space (F,q_a) for the shot #29155

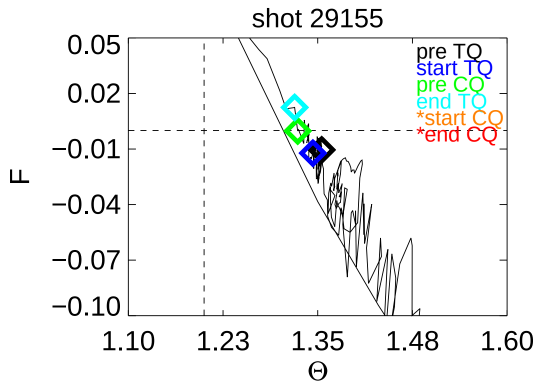

Figure 4.24: Path in the space (Θ,F) for the shot $\#29155$

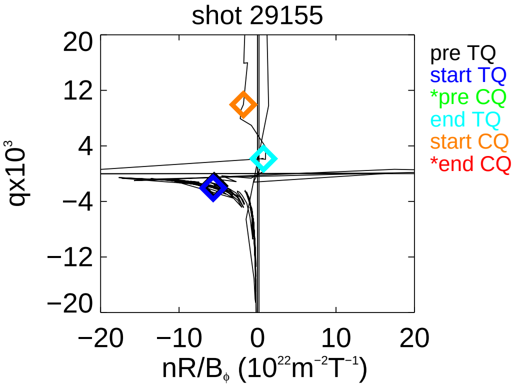

Figure 4.25: Path in the space ($\frac{nR}{B_\phi}$,q_a) for the shot $\#29155$

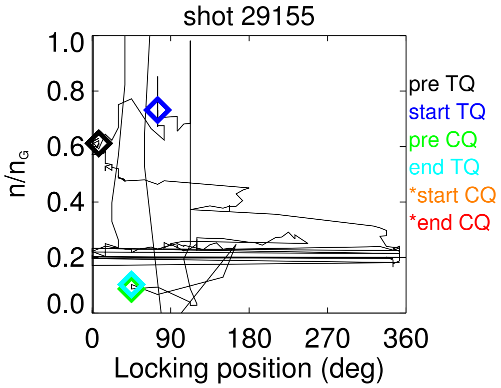

Figure 4.26: Path in the space (LP,n/n_G) for the shot $\#29155$

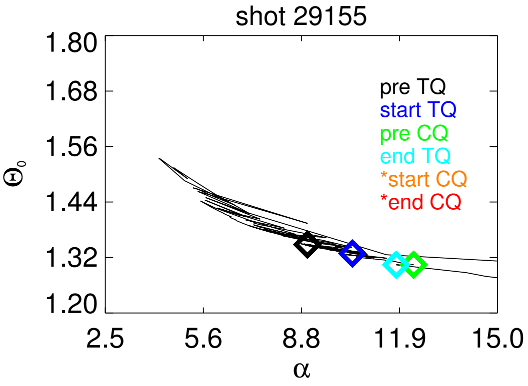

Figure 4.27: Path in the space (α,Θ_0) for the shot $\#29155$

32414 The session where this shot run was intended to study the effect of magnetic external perturbations on the plasma flow. In this shot, F and the plasma current were controlled in feedback and there was helium filling.

This shot has been chosen because of the controlled growth of the mode $(1, -6)$, which is not resonant in the plasma and thus doesn't contribute to the dynamo effect. In addiction to this, the mode is strongly locked at position 0 and stops there until the end of the discharge. Probably, the strong presence of this mode was the responsible for the loss of control on the plasma. In fact, the growth of this mode led to a sudden growth of the x rays, followed by an increase in α (and thus a flattening of the current profile) and a loss of the Θ parameter control (see figure 4.28). Moreover, the modes lock at time $113\,\mathrm{ms}$ (pre TQ) around position $30\,°$. This position is critical because here one of the saddle coils is broken, thus it is a preferred position for the locking. The thermal quench starts exactly when there is a sudden drop in the α parameter and, simultaneously, the magnetic field at border becomes positive. This change in the magnetic configuration, combined with the increase of the plasma resistivity due to the cooling of the plasma, lead to the current quench. In this shot the density has no increase but remains close to a fixed value.

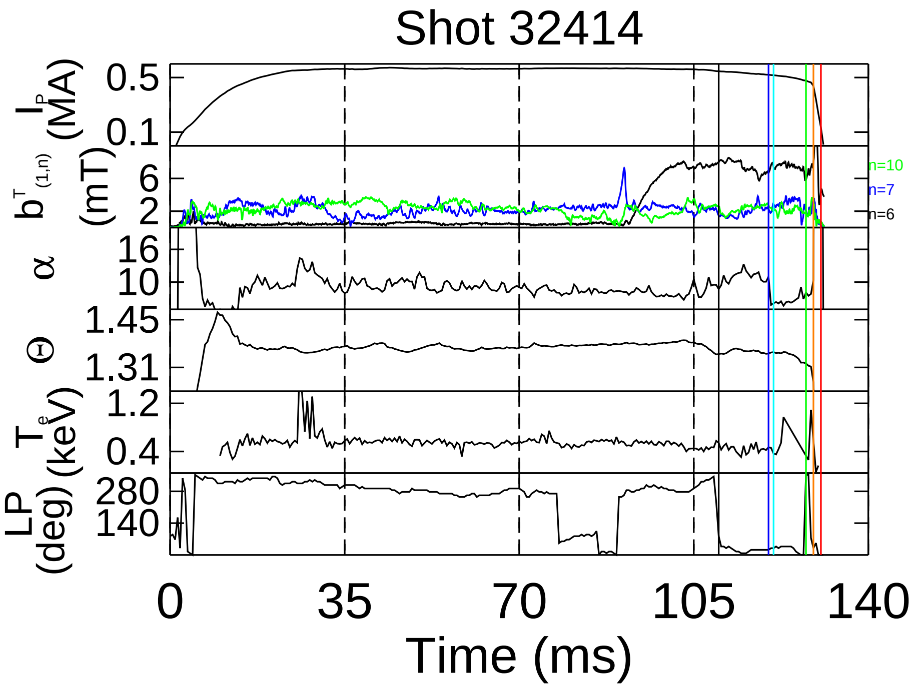

Figure 4.28: Relevant quantities for shot 32414

In this case we don't see in figure 4.29 and 4.33 the density growth that occurred in the shots analysed before. In this case a clear exit from the non-disruptive zones is hard to see, in fact from figures 4.30 to 4.32 we can see that the magnetic configuration was close to the loss of reversal at the end of the TQ and it is lost at the start of the CQ, but other considerations are hard to do. The α-Θ_0 evolution in figure 4.34 shows an alternation in the the current channel size and this can be related to the unstable mode that grew inside the plasma.

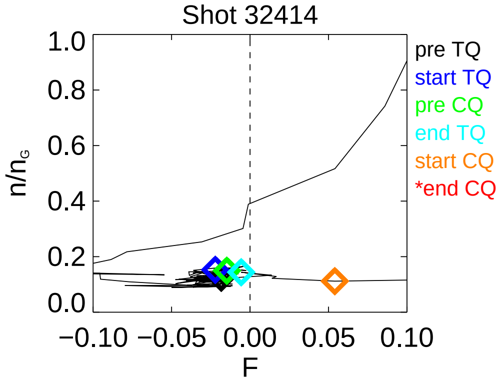

Figure 4.29: Path in the space (F,n/n_G) for the shot #32414

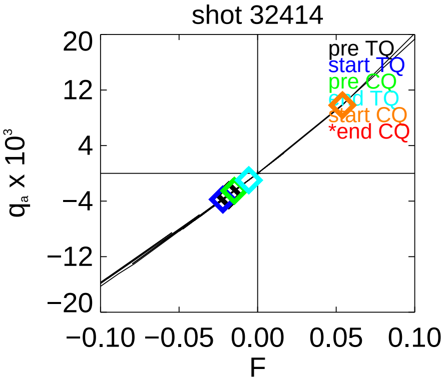

Figure 4.30: Path in the space (F,q_a) for the shot #32414

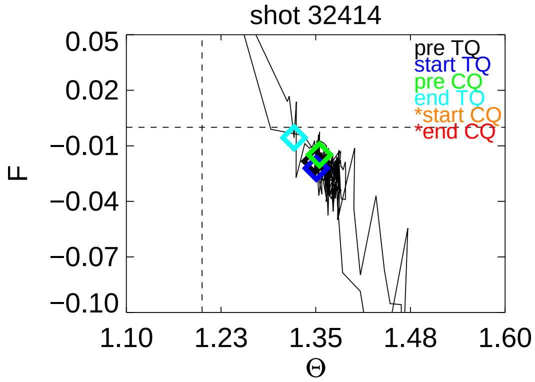

Figure 4.31: Path in the space (Θ,F) for the shot #32414

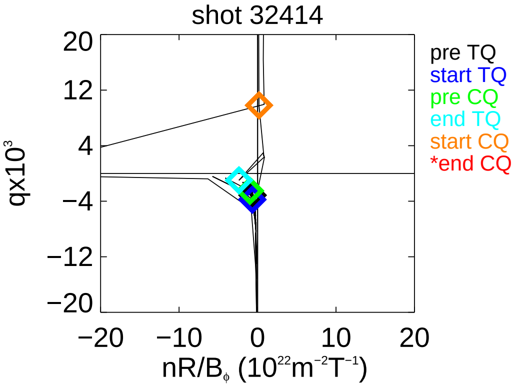

Figure 4.32: Path in the space ($\frac{nR}{B_\phi}$,q_a) for the shot #32414

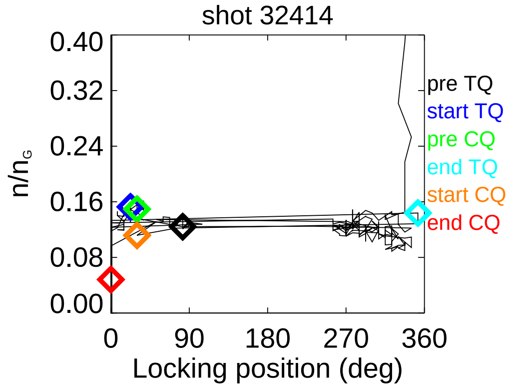

Figure 4.33: Path in the space (LP,n/n_G) for the shot $\#32414$

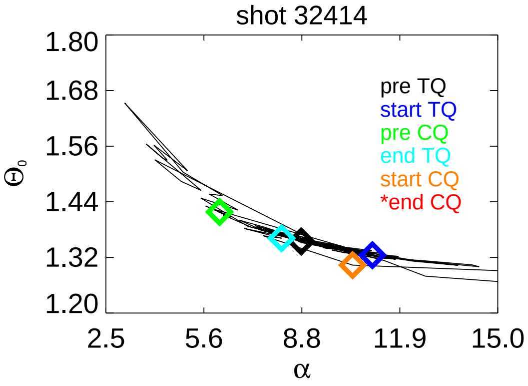

Figure 4.34: Path in the space (α,Θ_0) for the shot $\#32414$

36204 This shot belongs to a particular session used to investigate how the plasma reacts to several transitions between the states $q < 0$ and $q > 0$ (similarly $F < 0$ and $F > 0$) in a high current regime with gas injection during the $q > 0$ phases.

This discharge was highly prone to develop the QSH state but the first movement towards $q = 0$ at around $70\,\mathrm{ms}$ brought this state to suppression. During the $q < 0$ phase the QSH appeared again and there were many DREs, as figure 4.35 shows. The second time the plasma returned to the $q = 0$ state, the injection of gas caused probably an uncontrolled increase in the plasma density that induced the thermal quench. This energy loss and density growth increased the soft x-ray emission and the ohmic power, bringing the plasma shot to an end.

The density increase in this disruption has not started at the pre TQ, as can be seen in figure 4.36, but it seems that the density was well controlled up to the pre CQ time. This discharge follows a particular path in the operational spaces shown in figures 4.37, 4.38 and 4.39, in fact before the start of the CQ the trend is not going only towards the critical zones, but the parameters seem to move in stable regions before the CQ start. The exploration of regions with $q > 0$ cannot be seen from these figures. Looking in figure 4.40 the LP never seems to stop in a preferred position and in figure 4.41 we can see that the Θ_0 parameter has a range broader than the other discharges, in fact the value of 1.80 has never been reached before. The trend of α is similar to the other discharges.

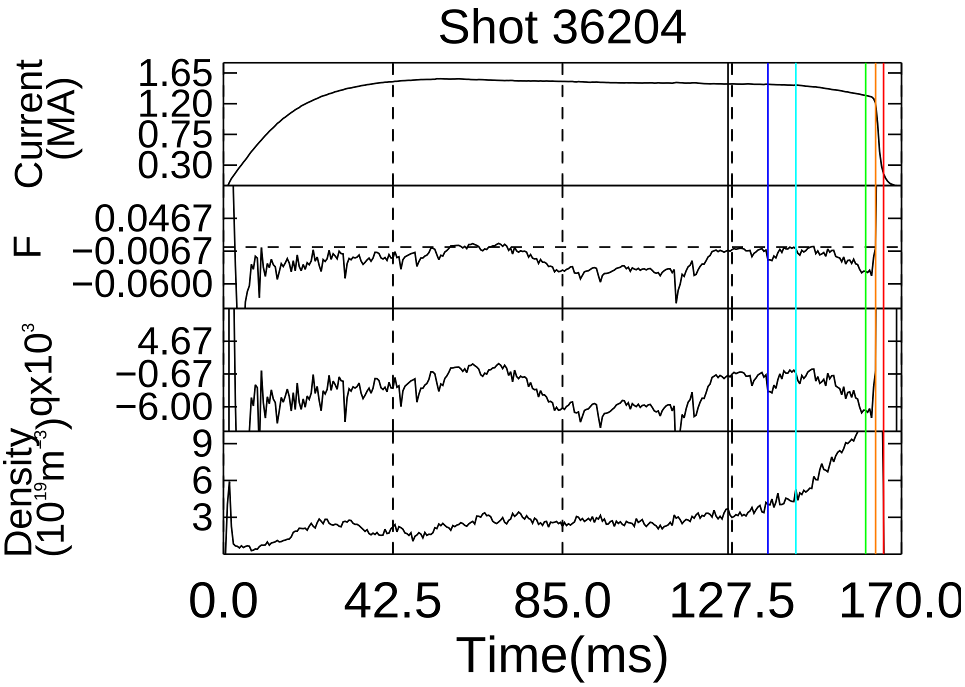

Figure 4.35: Relevant quantities for shot 36204

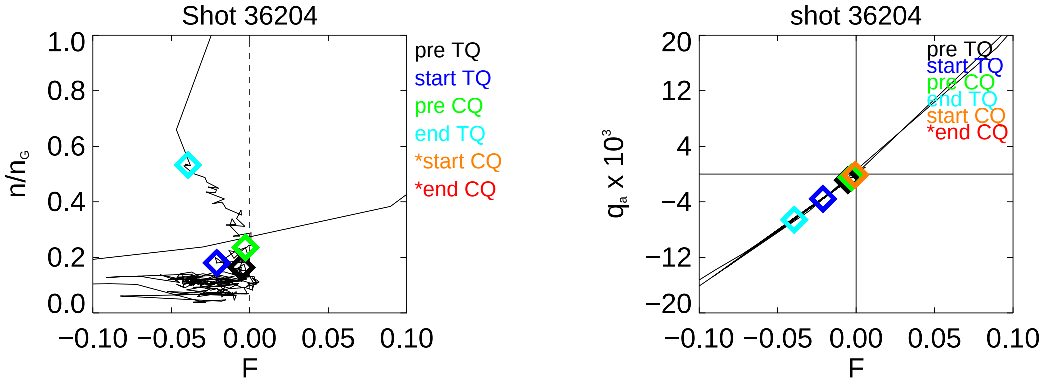

Figure 4.36: Path in the space (F,n/n_G) for the shot #36204

Figure 4.37: Path in the space (F,q_a) for the shot #36204

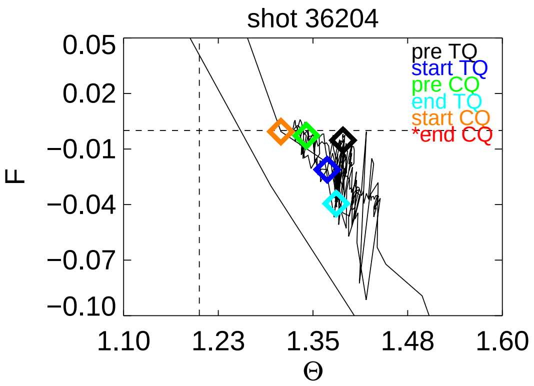

Figure 4.38: Path in the space (Θ,F) for the shot # 36204

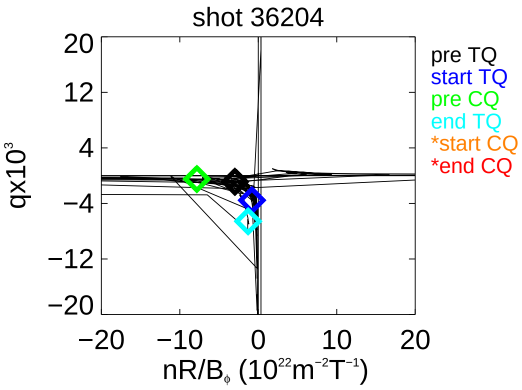

Figure 4.39: Path in the space ($\frac{nR}{B_\phi}$,q_a) for the shot # 36204

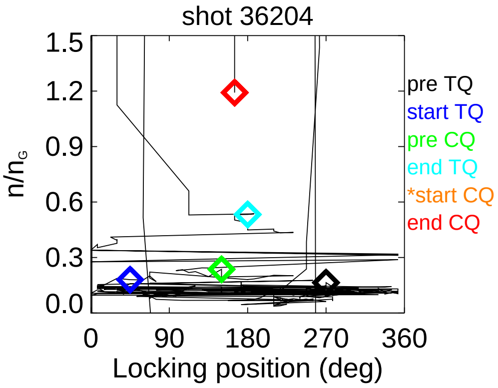

Figure 4.40: Path in the space (LP,n/n_G) for the shot # 36204

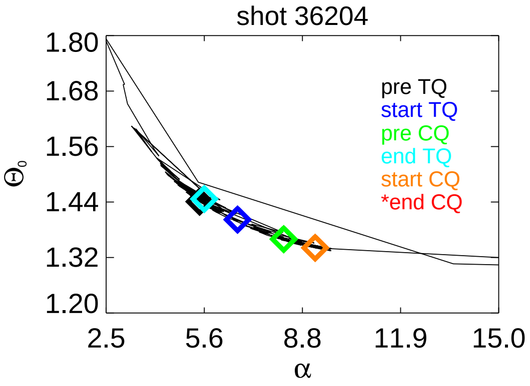

Figure 4.41: Path in the space (α,Θ_0) for the shot # 36204

36522 The operative set-up for this discharge was intended to study high currents plasmas. In detail, for this shot the F was feedback controlled, there was gas filling and two Li pellets were used during the flattop phase (at $92\,\mathrm{ms}$ and $100\,\mathrm{ms}$).

The shot had a temperature around $800\,\mathrm{eV}$ and was particularly fluctuating due to the DRE that often happened. The plasma developed a QSH state where the DREs are evident and it is important to notice that the injection of the pellets (at around $90\,\mathrm{ms}$ in figure 4.42) induced a suppression of the mode $(1,-7)$ and thus a MH state in the plasma. Around the pellet injection, it seems to be one relaxation event (the one with the growth of the $m = 0$ modes) and one $m = 1$ amplitude drop that was not linked to a dynamo action, in fact the $m = 0$ modes don't grow. After this critic event, the plasma was able to develop a QSH again and have some relaxation events but then, around $145\,\mathrm{ms}$, the modes seem to lock around position $140\,°$, there is the thermal quench, the mode $(1,-7)$ is no more able to grow up to the saturation and the density starts increasing. All this lead to an increase in the SXR, in α and in the ohmic power, until the plasma shuts down.

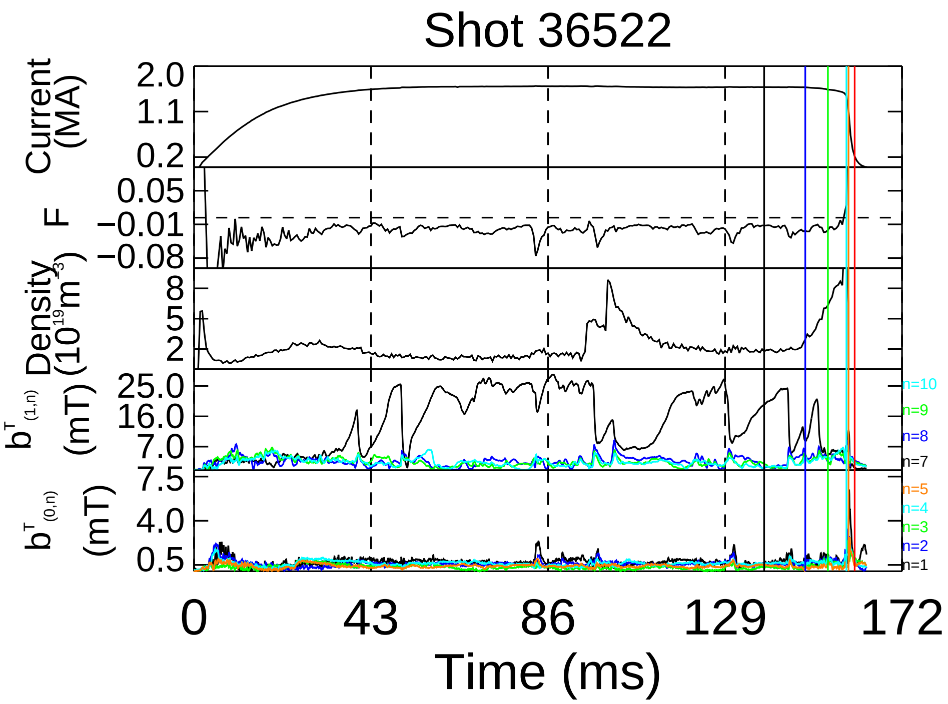

Figure 4.42: Relevant quantities for shot 36522

For this shot, the increase of the density before the lost of the reversal can be seen in figure 4.43. The field reversal is lost at the end of the thermal quench, as figures 4.44 and 4.45 show, and from figure 4.46 the amplitude of the magnetic field can be deduced: the path in this space is really close to the y-axis thus the toroidal magnetic field must have been stronger than the other cases. Despite this higher intensity of the magnetic field, it is interesting to note again that the field reversal is lost earlier with respect to the other discharges. Figure 4.47 shows that the LP is constantly moving and in figure 4.48 the current channel has a steepen increase between the start of the TQ and the pre TQ time.

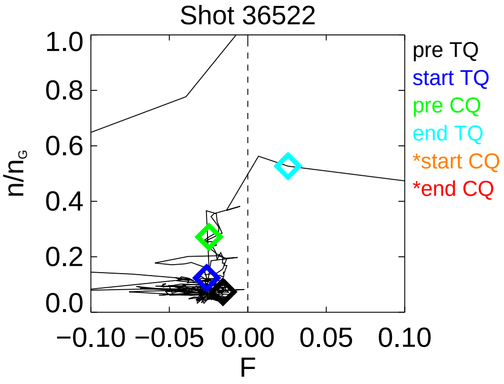

Figure 4.43: Path in the space (F,n/n_G) for the shot #36522

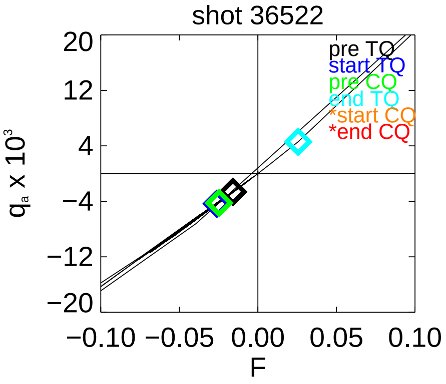

Figure 4.44: Path in the space (F,q_a) for the shot #36522

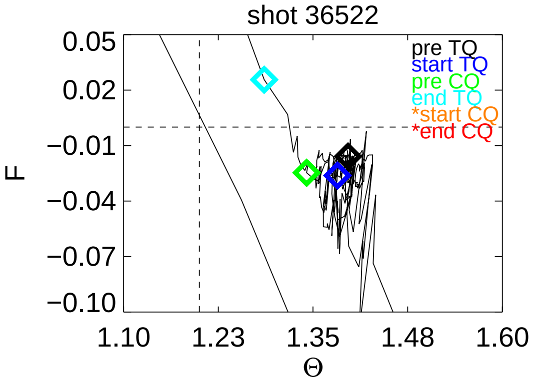

Figure 4.45: Path in the space (Θ,F) for the shot #36522

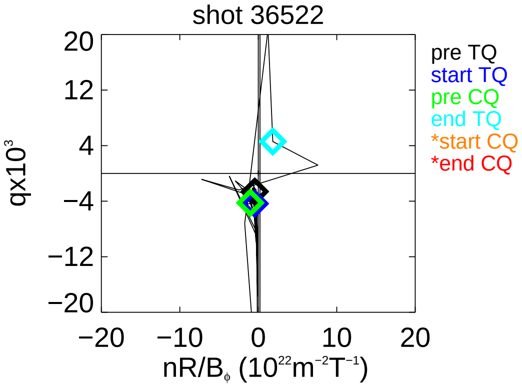

Figure 4.46: Path in the space ($\frac{nR}{B_\phi}$,q_a) for the shot #36522

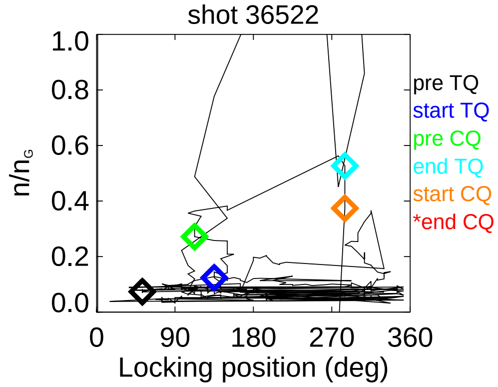

Figure 4.47: Path in the space (LP,n/n_G) for the shot $\#36522$

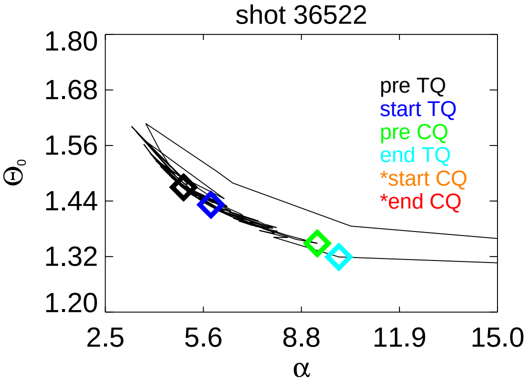

Figure 4.48: Path in the space (α,Θ_0) for the shot $\#36522$

36739 This shot is an example of a disruption caused by a bad set-up of the parameters during the ramp-up phase and by a particular discharge environment, in fact in this experimental session a graphite limiter was inserted in the chamber in order to measure the decay of thermal fluxes. For this shot, it was inserted for $10\,\mathrm{mm}$. As can be seen from figure 4.49, the plasma had been in a RFP configuration only for less than $10\,\mathrm{ms}$ before the current quench and thus there wasn't time to develop a disruption like in the cases before. In this shot, the density has always been quite high and always increasing. This uncontrolled growth is probably due to high plasma-wall interaction (probably connected to the modes locking at position $270\,°$) and it is the main responsible of the SXR emission and the plasma cooling.

Before the end of the TQ, the plasma density in figure 4.50 seems to be controlled and the LP in figure 4.54 doesn't seem to be connected with the density, but at the end of the TQ the magnetic configuration is lost, as figures 4.51 and 4.52 show. In the hugill plot 4.53, it can be seen that the range of the Murakami parameter is quite broad. From the graph in figure 4.55 we can see that the plasma current channel is always quite broad but at low values of Θ_0 and this can have induced the disruption.

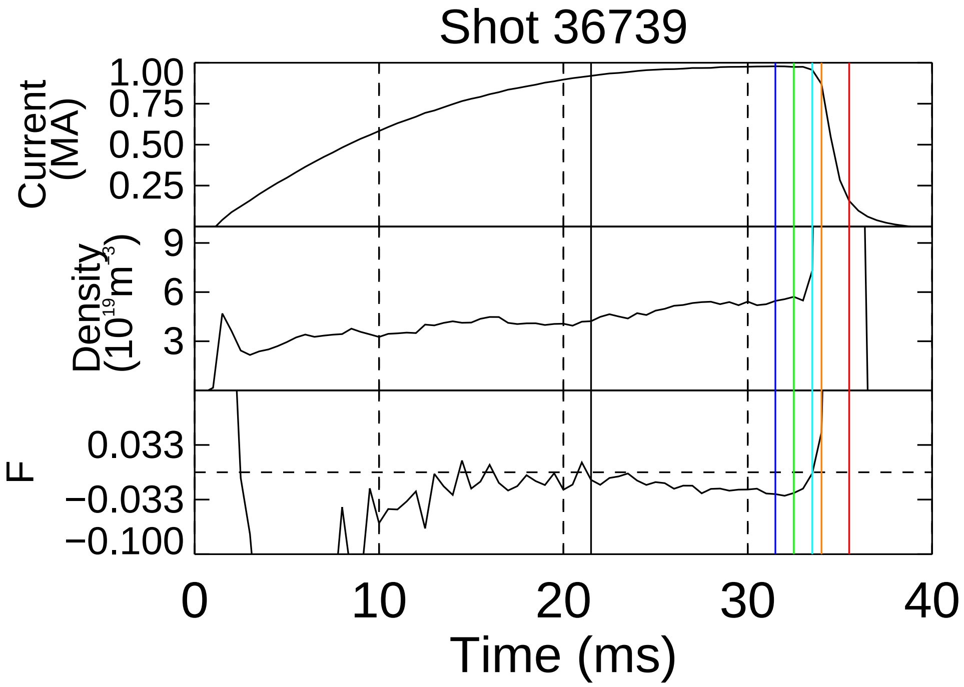

Figure 4.49: Relevant quantities for shot 36739

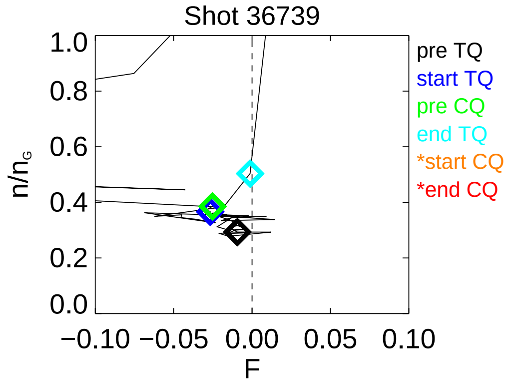

Figure 4.50: Path in the space (F,n/n_G) for the shot #36739

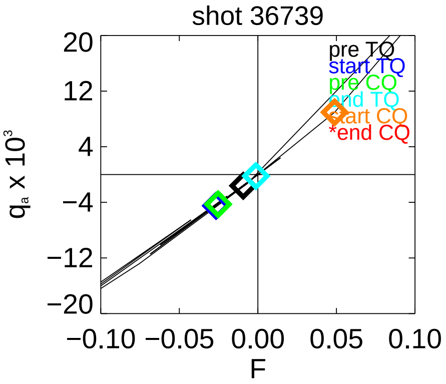

Figure 4.51: Path in the space (F,q_a) for the shot #36739

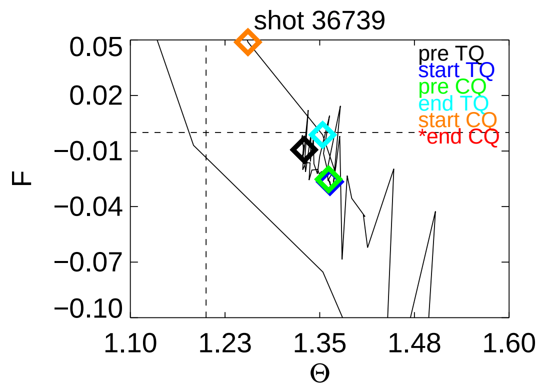

Figure 4.52: Path in the space (Θ,F) for the shot $\#36739$

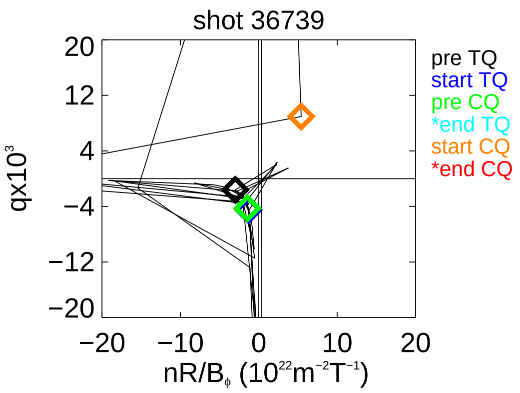

Figure 4.53: Path in the space ($\frac{nR}{B_\phi}$,q_a) for the shot $\#36739$

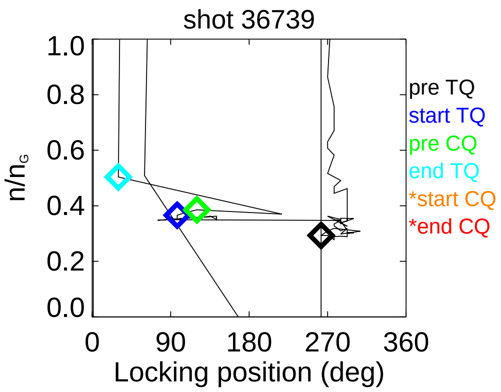

Figure 4.54: Path in the space (LP,n/n_G) for the shot $\#36739$

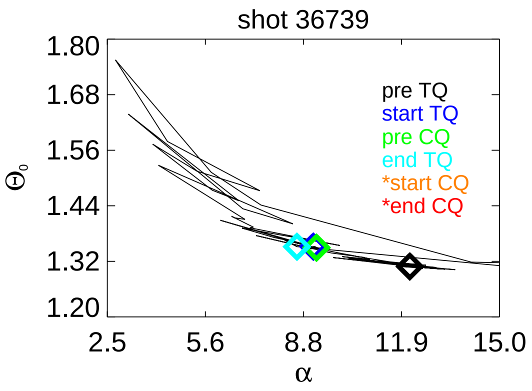

Figure 4.55: Path in the space (α,Θ_0) for the shot $\#36739$

37504 During this experimental session, the will was to study the wall conditioning (clean the wall surface in order to reduce the impurity flux from the wall) by injection of Li pellets. In the shot here considered, two pellets were injected (at $146\,\mathrm{ms}$ and $174\,\mathrm{ms}$) but they seem not to have a strong influence on the plasma density in the middle-long period. This discharge developed a QSH and many DRE occurred, with two of them that seem to be induced by the pellets injection. During all the shot, the SXR signal is strangely high. This can be caused by the shot preceding this one, in fact all the shots preceding (14 shots) have been done with Li injection and this could have had negative effects on the wall, causing impurities to influence the plasma behaviour. The last $20\,\mathrm{ms}$ the modes lock at around $120\,°$ and this occurrence could have given start to the density growth that caused the confinement loss. During the disruption here studied, the normalised density

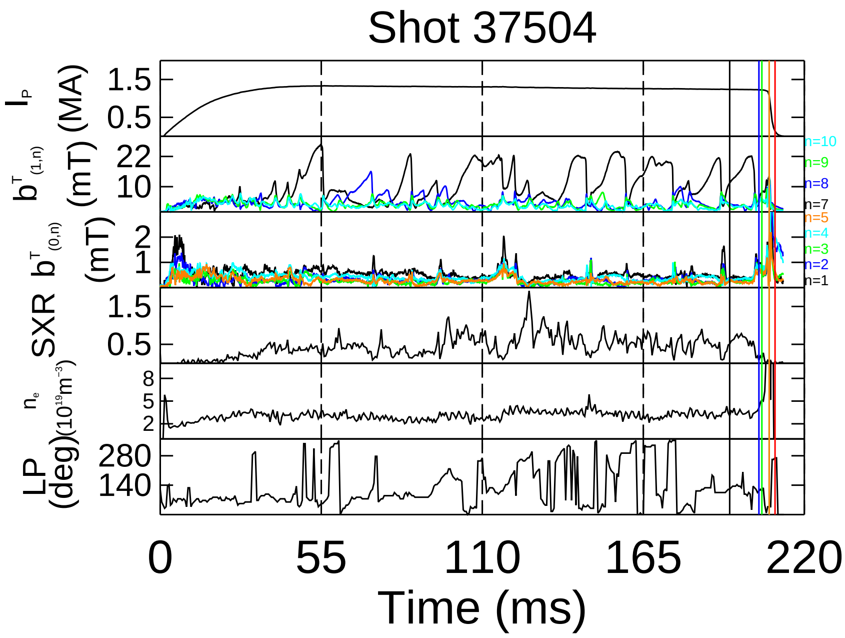

Figure 4.56: Relevant quantities for shot 37504

seems to stay in regions not harmful for the discharge (as can be seen in figure 4.57) but at the TQ start the LP stops, as already said, and the density seems to be quite connected to the locking of the modes. Figures 4.58, 4.59 and 4.60 show that the field reversal is lost at the beginning of the CQ but it can be seen that the toroidal field at border seems to reverse for brief instants. Lastly, from figure 4.62 the Θ_0 parameter is quite high for this discharge during the ramp-up phase but the strongest change in the plasma current channel size can be seen between the end TQ and the start of the CQ.

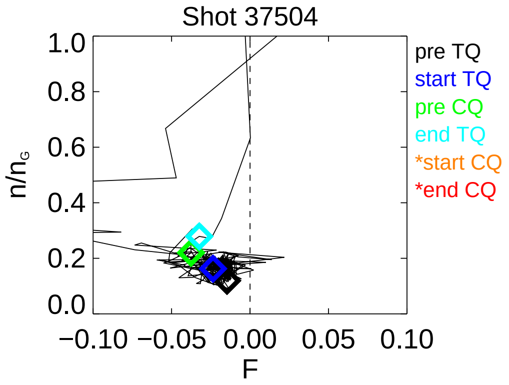

Figure 4.57: Path in the space (F,n/n_G) for the shot $\#37504$

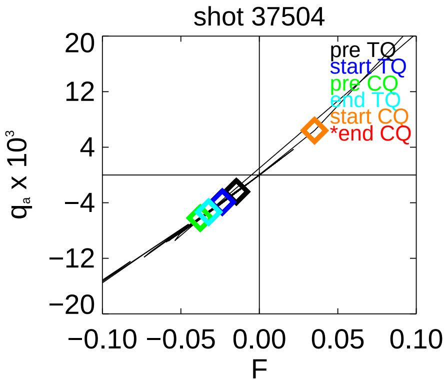

Figure 4.58: Path in the space (F,q_a) for the shot $\#37504$

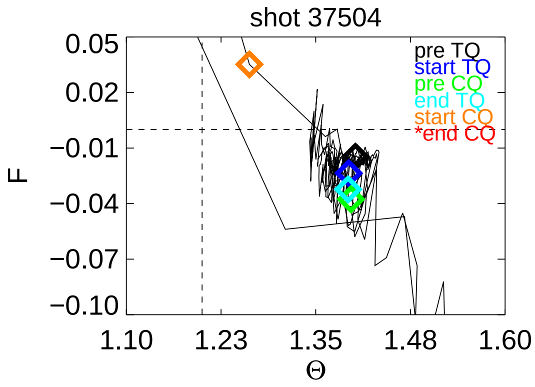

Figure 4.59: Path in the space (Θ,F) for the shot $\#37504$

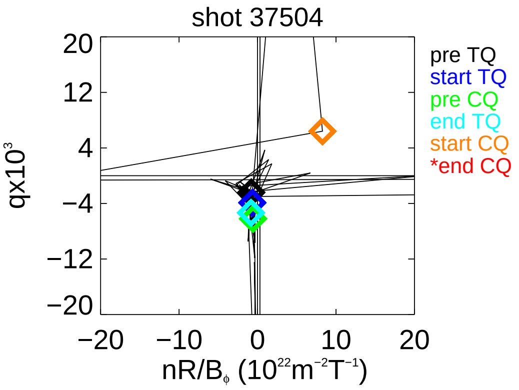

Figure 4.60: Path in the space ($\frac{nR}{B_\phi}$,q_a) for the shot $\#37504$

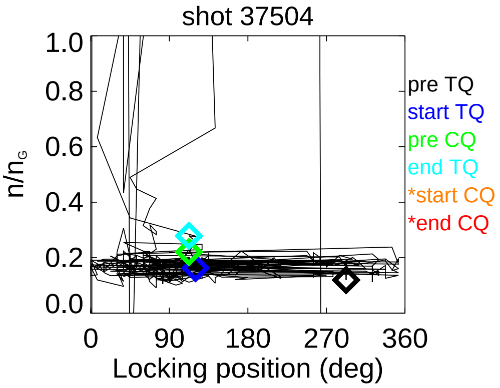

Figure 4.61: Path in the space (LP,n/n_G) for the shot $\#37504$

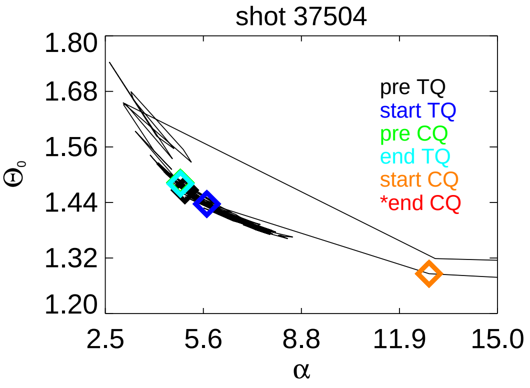

Figure 4.62: Path in the space (α,Θ_0) for the shot $\#37504$

4.5 Conclusion

In this chapter, an overview of the methods used in the creation a disruption database and the problems encountered in analysing the shots has been given, along with the description of some particular RFP discharges considered as meaningful for the phenomenology studied.

The creation of the database has been based on some relevant parameters, such as the time length of the shots, the decreasing rate of the current and the maximum poloidal voltage induced in the sensors. With this methodology, an ensemble of more than 300 shots has been selected. After finding the disruptive shots of RFX-mod, some quantities useful to describe a disruption have been presented. The shorter length of the CQ with respect to the TQ is one of the most interesting feature found since it is an opposite trend with respect to the tokamak.

The analysis of the plasma quantities such as the temperature and the density has been a challenging problem, above all for the diagnostic problems often encountered and the particular plasma dynamics that characterises a RFP. The TQ of the selected shots isn't as clear as the tokamak typical one, in fact the DREs cause high fluctuations in the plasma temperature and thus finding a well-definite quench isn't an easy task. If the temperature drop wasn't clearly detectable, the last DRE event is used for the evaluation of the TQ. The diagnostic failures and the problems connected to them have also been explained.

In the final section, eight shots have been studied in detail, aiming at finding some features they share. In particular, for all the discharges it has been found that at the beginning of the CQ the reversal of the field is lost and there are many cases where the control of the density parameter is lost before the sign change of the F parameter. During the disruption, for these cases a broadening of the current channel (that can be read in the increasing of the α parameter) is common, but for some of the cases analysed the current channel has fluctuations in size.

5

Statistical study of RFX-mod disruptions

In this chapter, statistical results from RFX-mod disruption database analysis are presented. The database is made of more than 330 disruptive RFP plasmas, selected with the procedure presented in the previous chapter. The first study focused on correlations of thermal quench and current quench times with other parameters such as the poloidal voltage and the plasma current. In the second part, an analysis on the behaviour of the magnetic modes is carried out, focusing on the mode normalised amplitudes, the spectral width and the locking strength. In the end, the same approach to the parameter spaces as the one done in the previous chapter is used in order to study the areas covered by the discharge parameters in these spaces.

5.1 Discharge general behaviour

A little note about the disruptions labelled here as **SGPR**. SGPR is the protection system of RFX-mod (explained more in detail in section 3.4) and in some discharges it operated before the current quench. It can be thought that these discharges have been *induced* by SGPR, although probably the discharge already went in a critical regime before SGPR intervention. In order to separate this kind of discharges, in this section the data are subdivided, but in the following part this separation won't be present. Each data set (the complete one, the one of the disruption induced by the SGPR and the one of the discharges not induced) is normalised to total number of the discharges.

As a first overview on the discharge behaviour, the statistics of I_{max} in figure 5.1, I_{PD}/I_{max} in figure 5.2 and of t_{end} in figure 5.3 are presented.

Initially, a statistic with the maximum current has been carried out. As it can be seen from figure 5.1, two peaks of the disruptions frequency can be found: one around $0.6\,\mathrm{M}\,ampere$ and another one around $1.3\,\mathrm{MA}$, both the peaks quite broader in amplitude. Taking into account only the SGPR discharges, there are three peaks in the disruptions frequency: one at $\sim 0.6\,\mathrm{MA}$, one at $\sim 1\,\mathrm{MA}$ and the last at around $\sim 1\,\mathrm{MA}$. The trend of all the database follow more closely the shots without the intervention of the SGPR system.

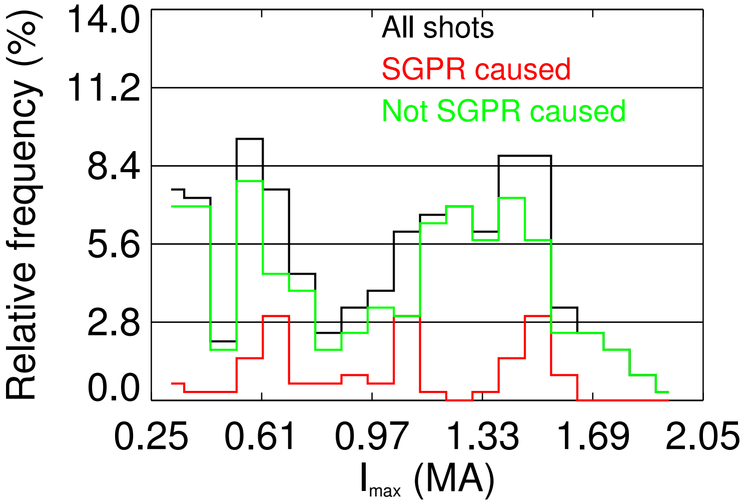

Figure 5.1: Histogram of the relative frequency of I_{max}. In the legend the meanings of the colours.

Considering now the normalised current I_{PD}/I_{max}, the minimum current I_{PD} was around $60\,\%$ of the I_{max} and the frequency of events with low I_{PD}/I_{max} current remains below or around 5 up to the value of 0.79. From this point on, there are significantly more discharges and the maximum is reached around $I_{PD} \approx 95\,\% I_{max}$, thus confirming that a disruption usually occurs well before the ramp-down phase. The same trend is seen for the discharges caused by the SGPR system and the one that occurred without its intervention.

Another interesting trend is seen in figure 5.3, where the histogram of the length of the discharge is plotted. As it can be seen, there is a high peak at around $50\,\mathrm{ms}$ (which contribution is given the most by the non-SGPR discharges). Another small peak can be placed around $110\,\mathrm{ms}$, with a small plateau up to $150\,\mathrm{ms}$. At this moment, the frequency of the discharges remains low (below $5\,\%$). An interesting peak is the one at around $320\,\mathrm{ms}$, where a higher concentration of the SGPR caused disruption can be seen.

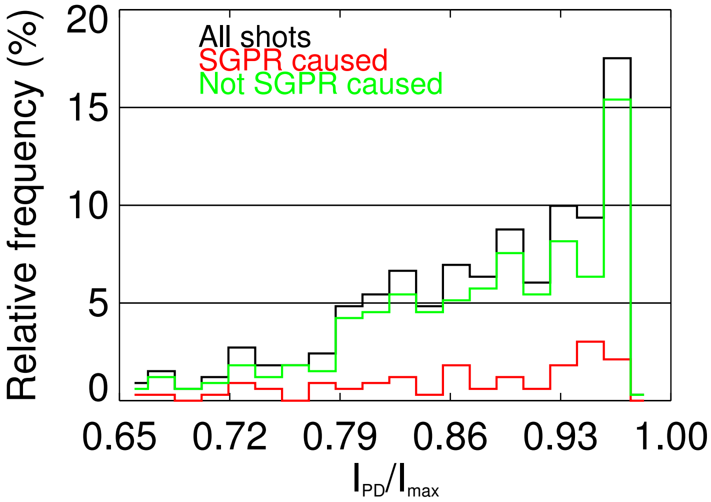

Figure 5.2: Histogram of the relative frequency of I_{PD}/I_{max}. In the legend the meanings of the colours.

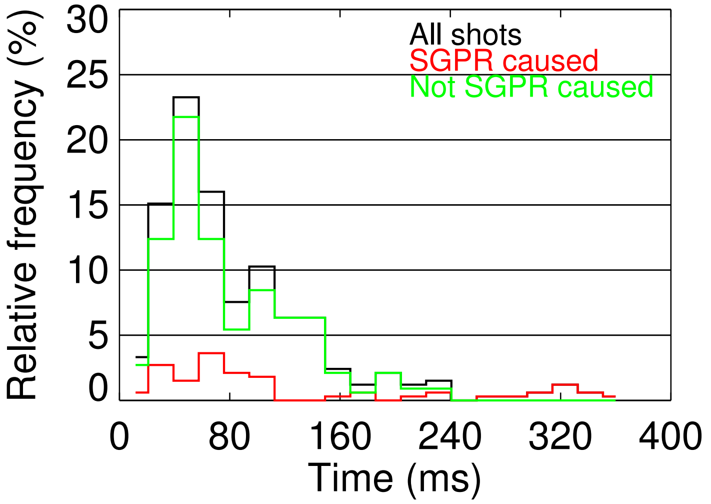

Figure 5.3: Histogram of the relative frequency of the discharge length. In the legend the meanings of the colours.

5.2 Current and thermal quench

In this section, the current quench and the thermal quench are studied and their correlation with other quantities is analysed.

In figure 5.4 the quench rate is plotted against I_{PD}. The quench rate is proportional to I_{PD} in the case of constant inductance and the majority of the shots analysed lies around the line $f(x)$ with the parameters $m = 0.32\,\mathrm{ms}^{-1}$, $q = 0\,\mathrm{MA\,ms}^{-1}$, with $f(x) = mx + q$. In the figure, in order to differentiate the various type of the discharges, the different colours discriminate the different F ranges. The symbols used are useful to do comparison with other analyses. From now on and for all the study, only the discharges that follow this trend and have the thermal quench (152 shots in total) will be used.

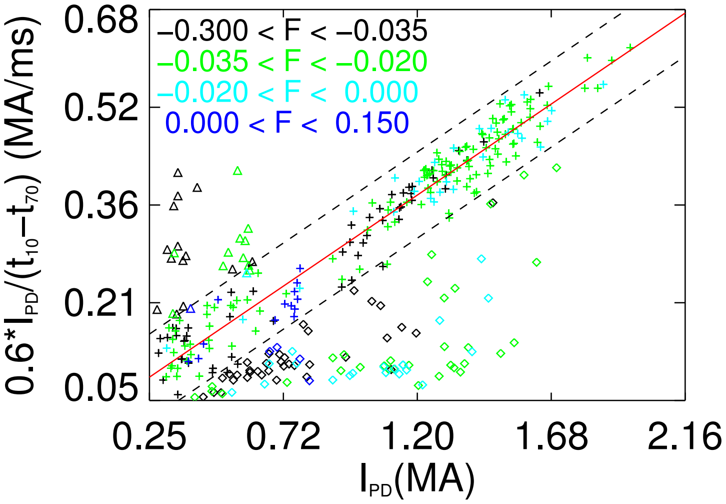

Figure 5.4: Plot of the quench parameter as a function of the pre-disruption current. The ranges of the F parameter are indicated.

The maximum poloidal voltage registered during the quench is plotted against the quench parameter in figure 5.5. A peak in the poloidal loop voltage is seen because of the variation of poloidal flux due to the loss of the toroidal current. In the case under discussion all the experimental data seem to lie in the same line.

A correlation has been found between the quench rate and the ratio I_{PD}/I_{max}. As figure 5.6 shows, it seems that for a fixed value of the abscissa the possible value in the ordinate is bounded by two curves. The upper boundary is understandable, in fact it implies a lower limit of Δt_{70-10}, which corresponds to the fact that the time the current needs to go from I_{PD} to $0\,\mathrm{A}$ is limited. Nevertheless it is interesting the dependence of this value from I_{PD}/I_{max}. The lowest value is given by a boundary

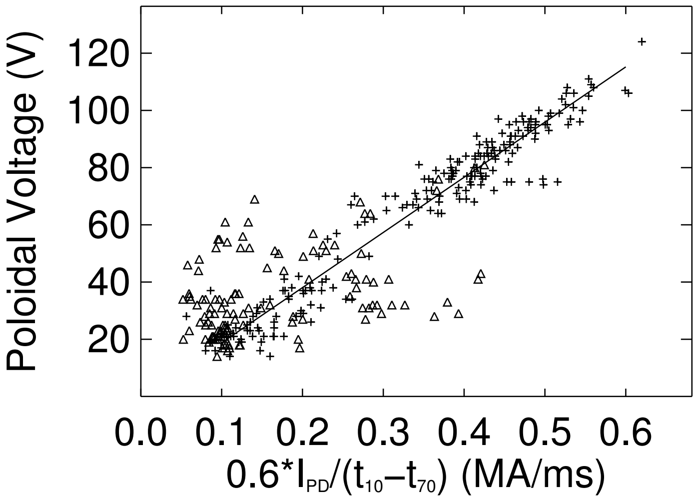

Figure 5.5: Plot of the maximum poloidal voltage registered versus the quench parameter. The symbol + represents the selected shots.

used in finding the disruptions, that is the limit on the 'slope' of the CQ expressed in section 4.1.

Generally, in the tokamak disruptions the current quench is always shorter than the thermal quench (as said in subsection 2.2.1). This has not been found for the RFP, in fact in figure 5.7 the TQ time is plotted against the CQ time and it is clear that for most of the discharges used (the ones whose TQ could be found) the trend found in the tokamak is no longer followed.

5.3 MHD modes behaviour

The mean amplitude of the MHD modes (normalised over the poloidal field at the plasma edge $B_\theta(a)$), the spectral width and the position of the locking of the shots has been analysed during the development of the disruptions. An explanation of the quantities described below can be found in subsection 1.3.3.

In the figures below, ranging from figure 5.8 to 5.11, the $m = 0$ normalised amplitude is plotted against the n number of the modes. The shots have been subdivided in current ranges because different ranges correspond to different plasma behaviours (e.g. at higher currents the QSH is easily reached). As we can see, before the start of the CQ, for each current range the modes have a normalised amplitude below 1% of the poloidal field at the edge. A peculiar dynamics of the $m = 0$ modes can be identified during the current quench. In fact, as the figures show, for all the current ranges all the modes tend to grow in amplitude, in

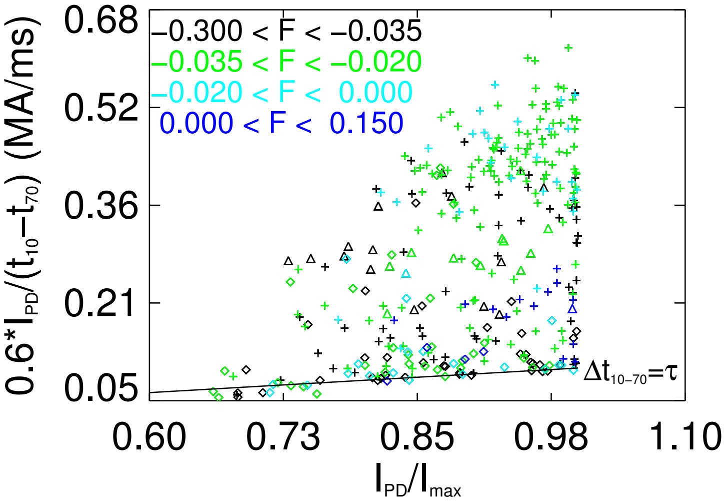

Figure 5.6: Plot of the quench parameter as a function of I_{PD}/I_{max}. The colors and symbols are the same of figure 5.4.

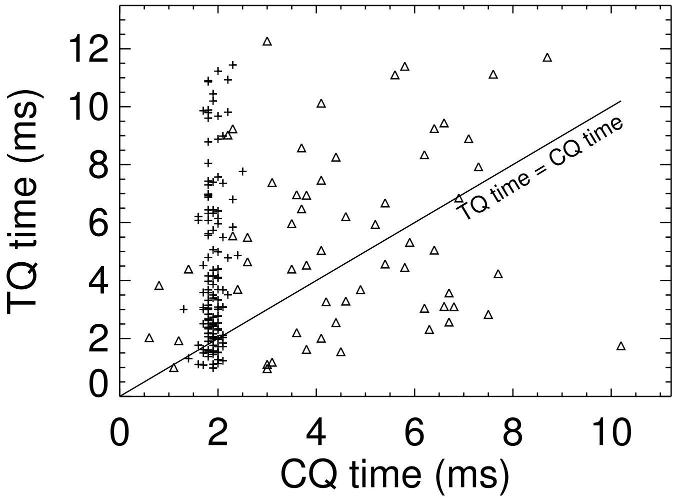

Figure 5.7: Plot of the TQ time against the CQ time. The symbol + represents the selected shots.

particular the even n modes. Only in the cases with the current ranges $0.3-0.8\,\mathrm{MA}$ and $1.2-1.6\,\mathrm{MA}$ also the $n=1$ mode grows, in the first case also in a stronger way than the $n=2$ mode. This behaviour can be explained because of the change in the magnetoplasma configuration: at the beginning an RFP was sustained, the F parameter was negative and the reversal surface was inside the plasma; during the last phase, the system configuration is an ultra-low q and the reversal surface exited the plasma. This could have changed the MHD activity of the modes and then explain the behaviour that is seen.

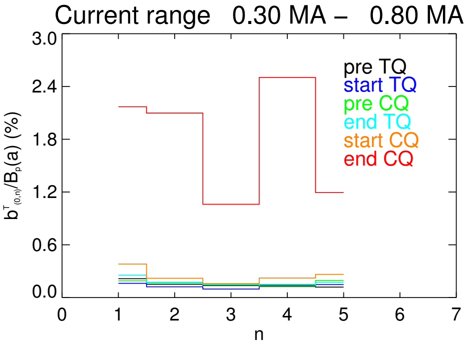

Figure 5.8: Development of the modes $m=0$ amplitude in the lowest current range.

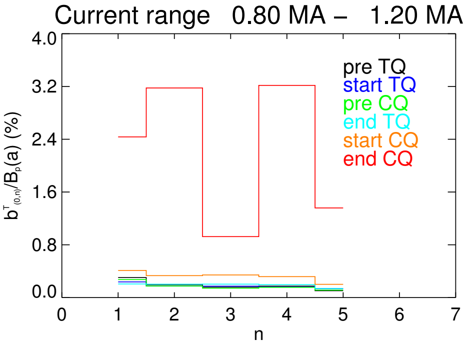

Figure 5.9: Development of the modes $m=0$ amplitude in the second current range.

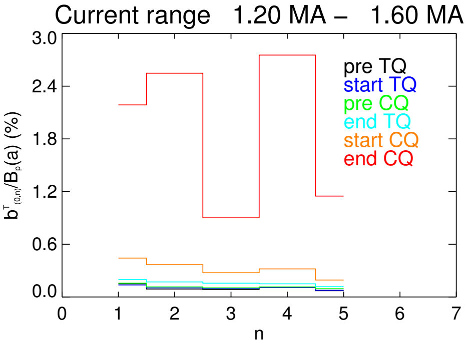

Figure 5.10: Development of the modes $m=0$ amplitude in the third current range.

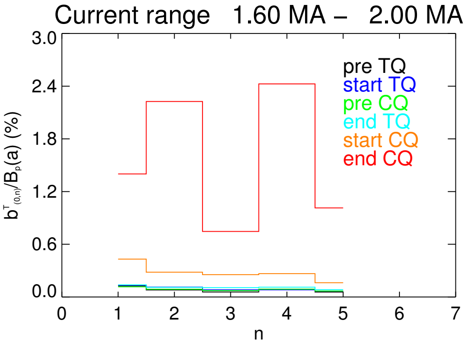

Figure 5.11: Development of the modes $m=0$ amplitude in the highest current range.

An analysis on the $m=1$ magnetic modes has also been done. In this case, the n selected for the MHD modes is in the range $-14<n<0$. The shots have been subdivided in the same current ranges as above. In the case of the

$m = 1$ modes, the MHD activity is in agreement with the theory: the non-resonant modes ($-7 < n < 0$) have small amplitude while a peak around the $n = -7$, $n = -8$ modes can be identified and then a decrease in the modes amplitude can be seen. This is particularly evident in the last two current ranges. The normalised amplitude of the modes seems to increase with the developing of the disruption and also the non resonant modes seem to participate more in the MHD activity of the plasma. This reaches a maximum at the end of the disruption, where the maximum of the modes amplitude is seen in every current range. In particular, for the range $0.3 - 0.8\,\mathrm{MA}$ the mode $n = -7$ is the dominant one at the end of the discharge, while in the other ranges the modes $n = 5, 7, 12$ seem to have the highest normalised amplitudes. The energy of the MHD spectrum (linked to the amplitude by the relation $W_{(m,n)} = \frac{b^2_{(m,n)}}{2\mu_0}$) seems to redistribute itself all over the spectrum during a disruption and this can be seen also analysing the spectral width.

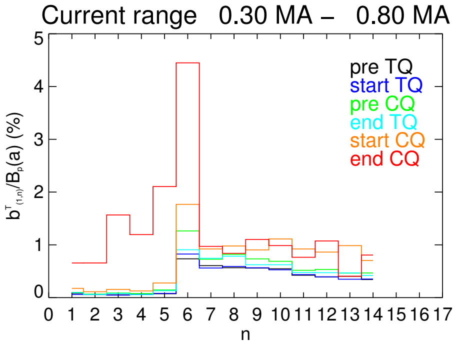

Figure 5.12: Development of the mode $m = 1$ amplitude in the lowest current range. The x-axis shows the absolute n values.

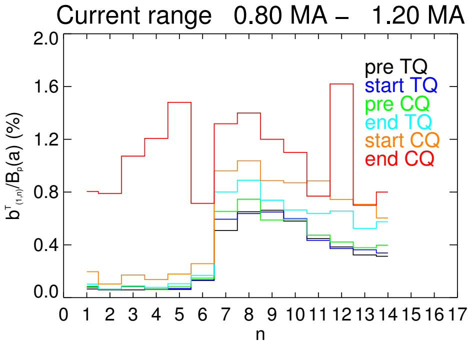

Figure 5.13: Development of the mode $m = 1$ amplitude in the second current range. The x-axis shows the absolute n values.

In the following graphics (figures 5.16 and 5.17), the spectral width as function of the current is shown at different time values. This parameter ranges from a value of ~ 1, reached at higher currents and before the TQ, to a value of ~ 8, reached also for the highest values of I_{PD} at the end of the CQ, in agreement with what has been studied for the modes amplitude. In figure 5.16, the horizontal lines show the position of the average spectral width at different times and it can be seen that the trend of the spectral width is to grow in time, except for the time of the CQ start, where the width decrease. Looking at figures from 5.18 to 5.23, we see that the spectral width is higher for lower currents and, for all the current ranges, the spectral width doesn't spread much until the TQ start occurs. At the end of the CQ, there are no shots with a QSH state.

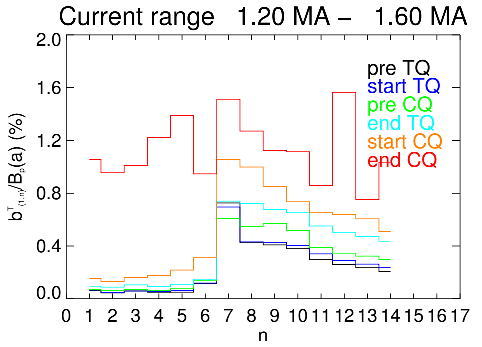

Figure 5.14: Development of the mode $m = 1$ amplitude in the third current range. The x-axis shows the absolute n values.

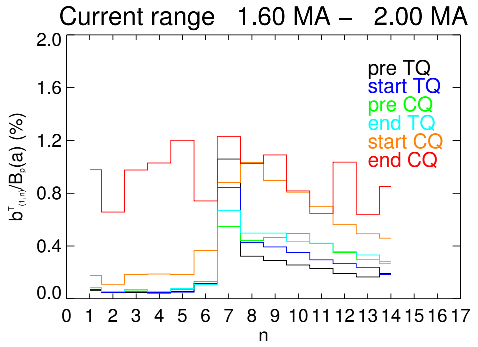

Figure 5.15: Development of the mode $m = 1$ amplitude in the highest current range. The x-axis shows the absolute n values.

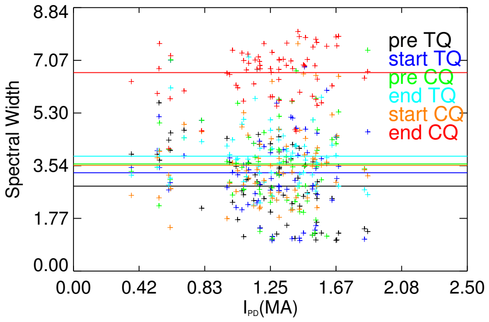

Figure 5.16: Plot of the spectral width ($m = 1$) of the selected shots at all the times considered.

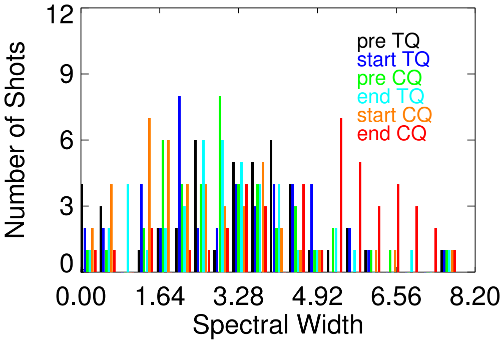

Figure 5.17: Histogram of the spectral width ($m = 1$) of the selected shots for each times considered.

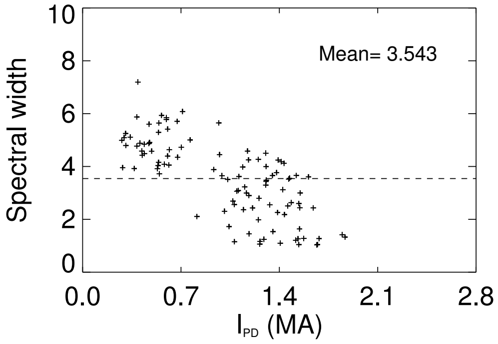

Figure 5.18: Plot of the spectral width ($m = 1$) of the selected shots at the pre TQ time

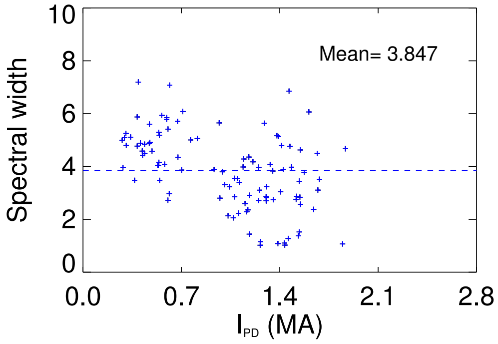

Figure 5.19: Plot of the spectral width ($m = 1$) of the selected shots at the start TQ time

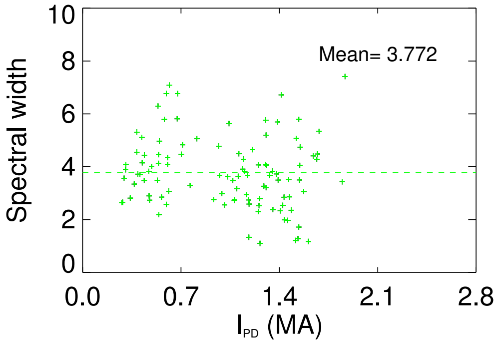

Figure 5.20: Plot of the spectral width ($m = 1$) of the selected shots at the pre CQ time

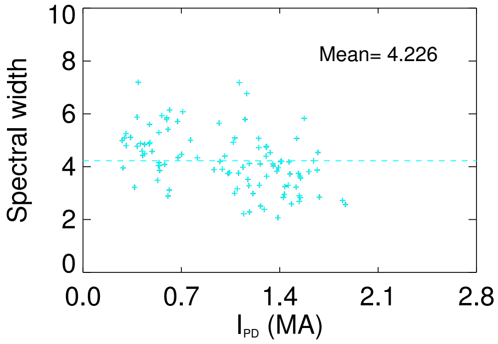

Figure 5.21: Plot of the spectral width ($m = 1$) of the selected shots at the end TQ time

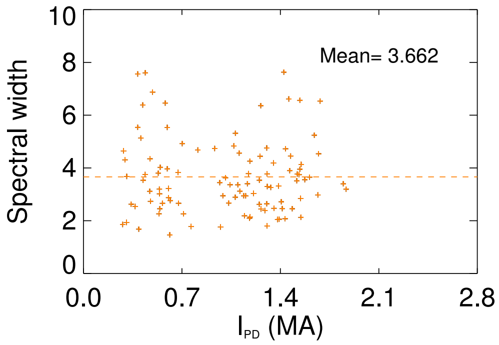

Figure 5.22: Plot of the spectral width ($m = 1$) of the selected shots at the start CQ time

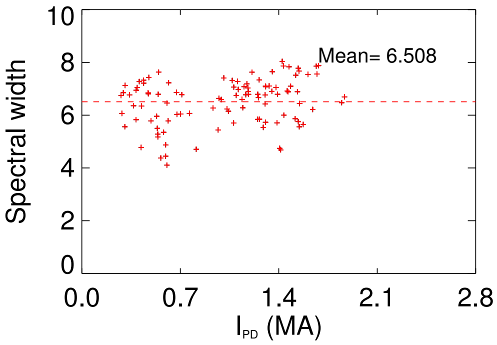

Figure 5.23: Plot of the spectral width ($m = 1$) of the selected shots at the end CQ time

The position of the LP has been studied all over the times of the discharge in figures 5.24 and 5.25. Analysing figures from 5.26 to 5.31, we see that in average the modes lock and stay locked at the same positions, with a difference of $\approx 20°$, except for the CQ where the LP drastically moves, probably thanks to the sudden growth of the modes, in particular with $m = 0$. The position of the LP is not particularly peaked except for the end CQ time, when there is a strong accumulation of the disruptions LP value at around $40°$, position where one of the saddle coils is broken and thus the control is less effective.

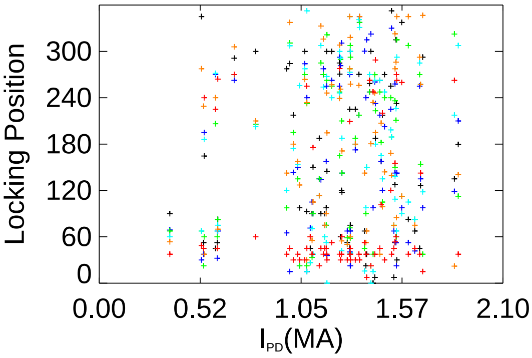

Figure 5.24: LP at all the times considered as function of the current.

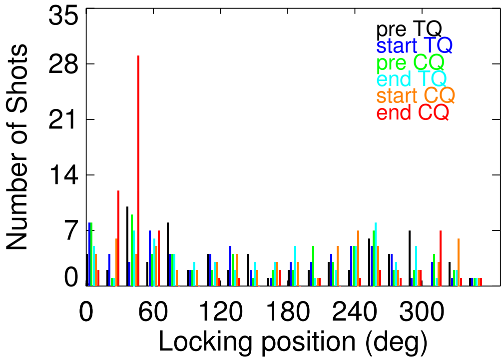

Figure 5.25: Histogram of the LP at all the times considered.

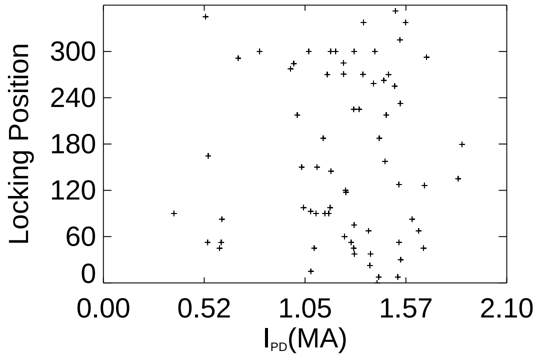

Figure 5.26: LP at the pre TQ time as function of the current.

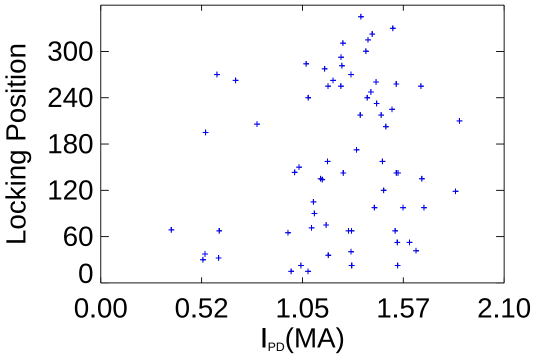

Figure 5.27: LP at the start of the TQ as function of the current.

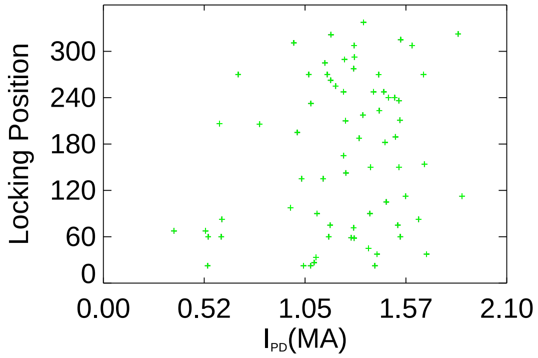

Figure 5.28: LP at the pre CQ as function of the current.

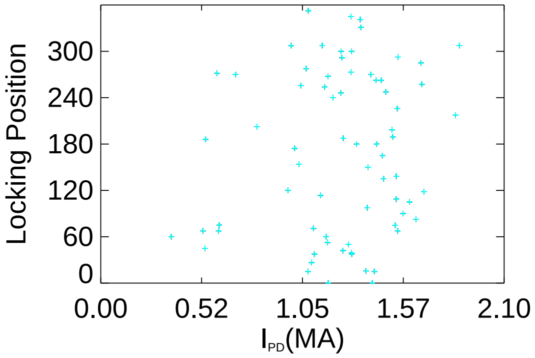

Figure 5.29: LP at the end TQ as function of the current.

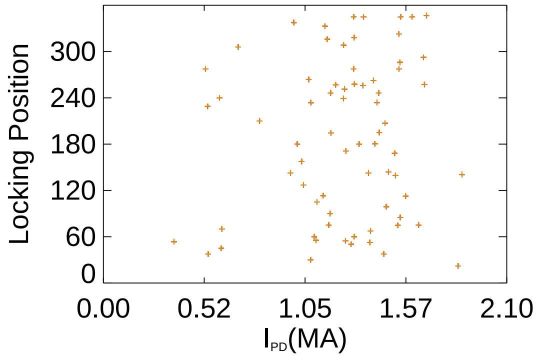

Figure 5.30: LP at the start CQ as function of the current.

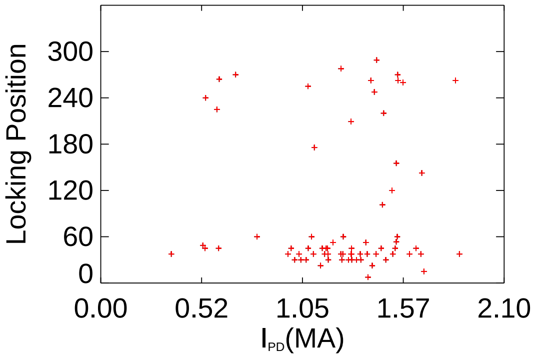

Figure 5.31: LP at the end CQ as function of the current.

5.4 Path of the discharges

In this section, the path of the discharges in various operational spaces is presented. The operational spaces are the same used in chapter 4.

5.4.1 Operational space (F,n/n_G)

In figures from 5.32 to 5.38 the path in the space (F,n/n_G) is shown. Looking at figure 5.32, it is evident that the growth of the density is much faster and more important with respect to the change of sign of the F parameter. In fact, the normalised density fast grows to values higher than 1 at the TQ start, while in average the F value keeps lower than 0 up to the CQ start. This can be an indication and a confirmation that the plasma density control is lost in the discharge far before the loss of the magnetic configuration control. In average, after the start of the TQ the density remains at the same values, as figures 5.34 to 5.38 show, but the F parameter drastically increases.

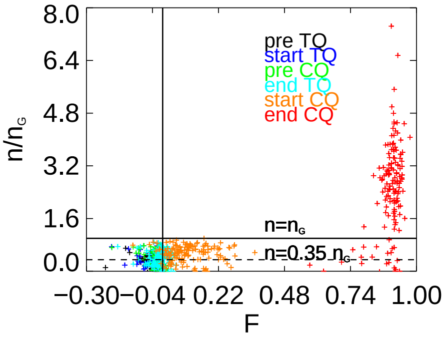

Figure 5.32: n/n_G as a function of F for all the relevant times.

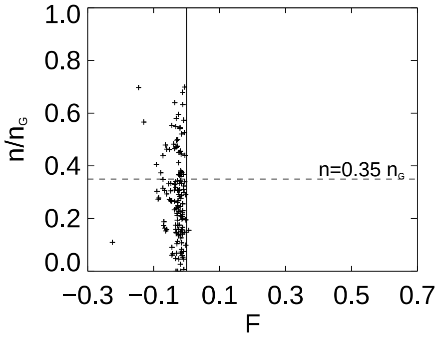

Figure 5.33: n/n_G as a function of F before the TQ.

5.4.2 Operational space (F,q_a)

After an analysis of the (F,n/n_G) space of the discharges, also the (F,q_a) space has been studied, as figures 5.39 to 5.45 show. The following relations are valid

$$F = \frac{B_\phi(a)}{\langle B_\phi \rangle} \qquad q_a = \frac{a \cdot B_\phi(a)}{R_0 \cdot B_\theta(a)} = \frac{a}{R_0}\frac{F}{\Theta} \tag{5.1}$$

thus we expect the parameter to lie in the first and third quadrant (where the two share the sign). From figure 5.39 we can see that the data points seem to lie in the

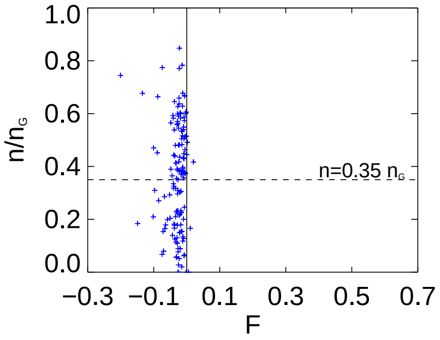

Figure 5.34: n/n_G as a function of F at the start of the TQ.

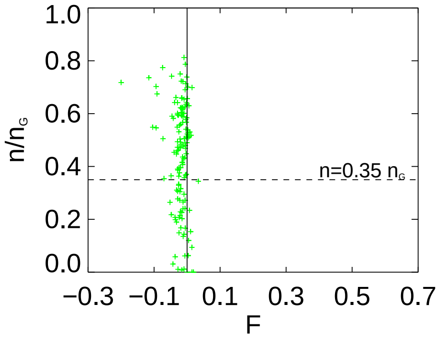

Figure 5.35: n/n_G as a function of F at the pre CQ.

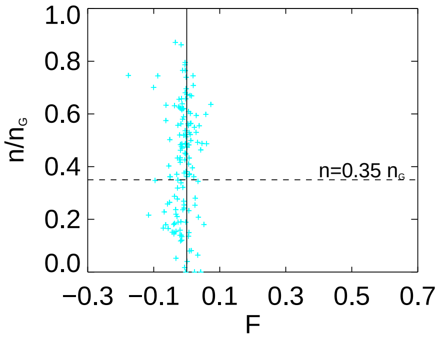

Figure 5.36: n/n_G as a function of F at the end of the TQ.

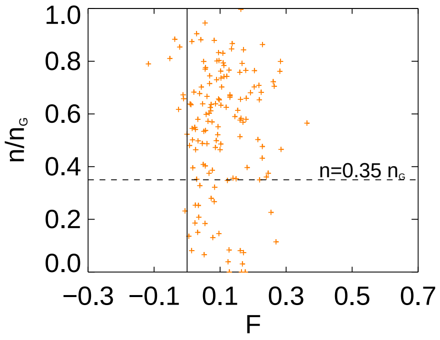

Figure 5.37: n/n_G as a function of F at the CQ start.

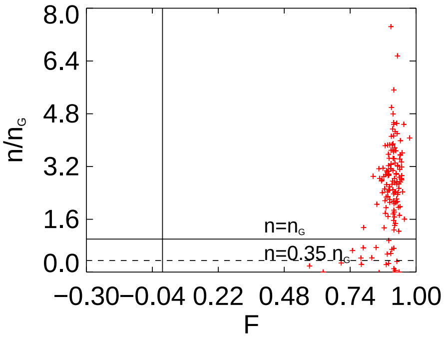

Figure 5.38: n/n_G as a function of F at the CQ end.

same line from the beginning of the disruption up to the start of the CQ. At this temporal point, as can be seen in figure 5.44, the points at higher values of F tend to deviate from the line and then, as can be seen in figure 5.45, the points follow no more a linear trend. The linear relationship between the two parameters is given by the fact that the ratio $\frac{\langle B_T \rangle}{B_\theta(a)} = \Theta^{-1}$ is almost the same for all the discharge length and, as we can see from the points disposition in figures 5.40, 5.41, 5.42 and 5.43, also for the disruptive discharges. The reversal surface starts going out from the plasma from the TQ start, also if the majority of the discharges has q_a below 0 also at the end of the TQ. Very few keep the reversal configuration up to the CQ start, but at the CQ end the RFP configuration is lost in all the cases analysed.

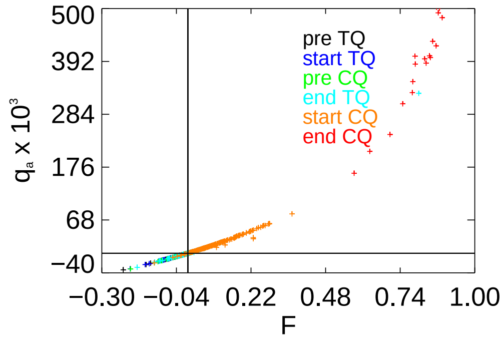

Figure 5.39: Plot in the space (F,q_a) for all the relevant times.

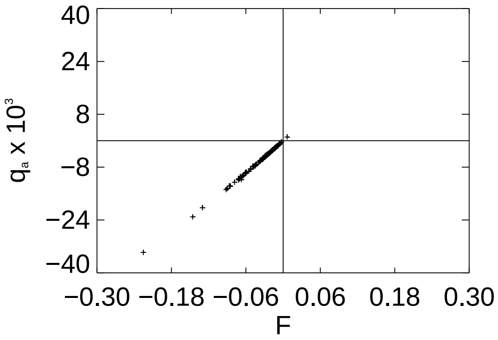

Figure 5.40: Plot in the space (F,q_a) at the pre TQ time.

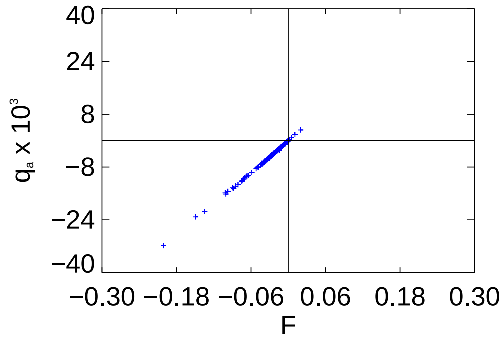

Figure 5.41: Plot in the space (F,q_a) at the TQ start.

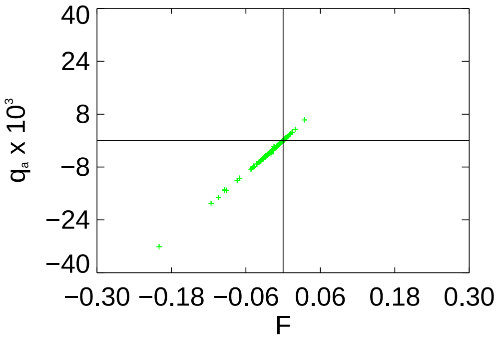

Figure 5.42: Plot in the space (F,q_a) at the pre CQ time.

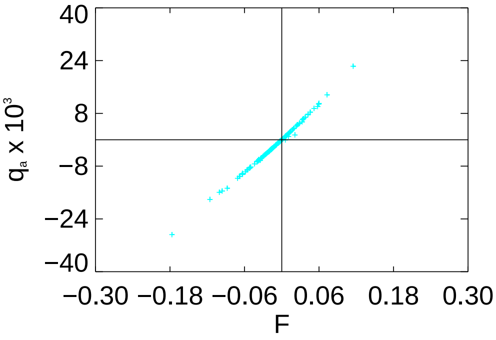

Figure 5.43: Plot in the space (F,q_a) at the TQ end.

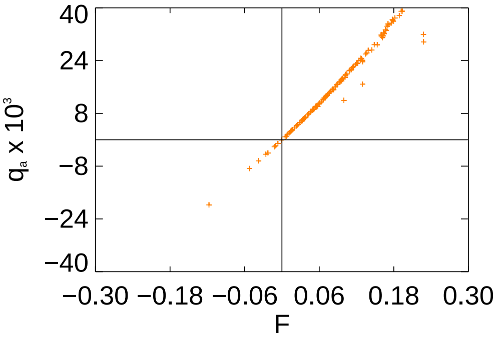

Figure 5.44: Plot in the space (F,q_a) at the start of the CQ.

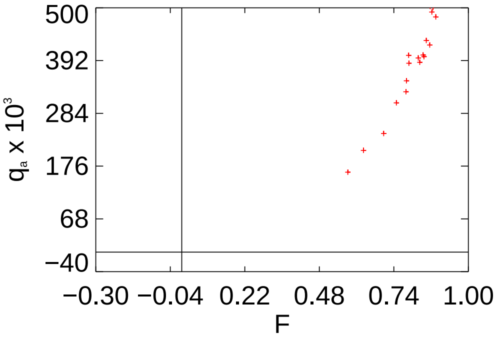

Figure 5.45: Plot in the space (F,q_a) at the end of the CQ.

5.4.3 Operational space (F,Θ)

In figures from 5.46 to 5.52, the operational space (F,Θ) is shown. During the evolution of the disruption, not all the discharges keep the same behaviour: while at the beginning (figures 5.47,5.48,5.49) the points seem to locate in a restricted area, at the end of the TQ (figure 5.50) and at the beginning of the CQ (figure 5.51) there is a broader distribution of the points. The end of the disruption can be easily located in a well defined area ($F > 0.8$, $\Theta \approx 0.32$, as can be seen in figure 5.52.

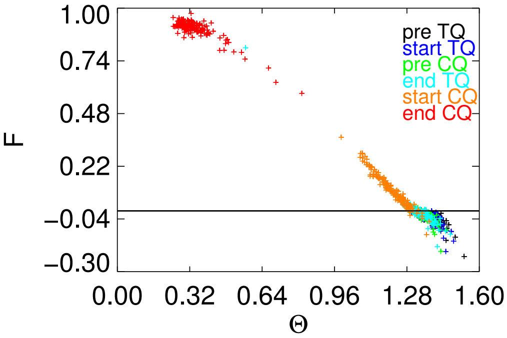

Figure 5.46: Plot of F versus Θ during all the disruption length.

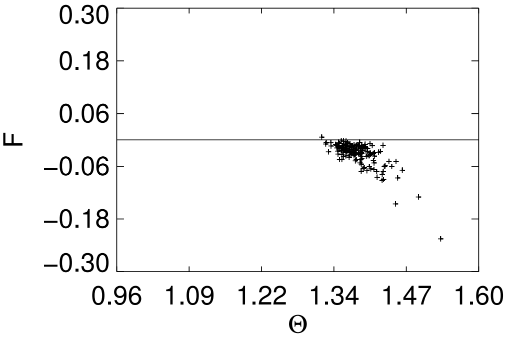

Figure 5.47: Plot of F versus Θ at the pre TQ.

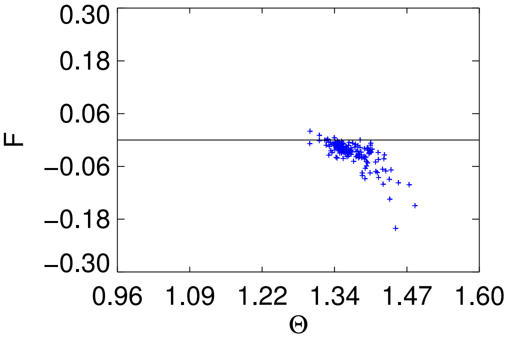

Figure 5.48: Plot of F versus Θ at the start of the TQ.

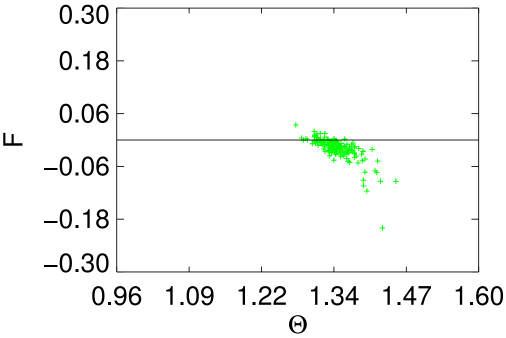

Figure 5.49: Plot of F versus Θ at the pre CQ time.

5.4.4 Operational space (q_a,$\frac{nR}{B_\phi(a)}$)

The pseudo-Hugill plot is displayed in figures 5.53 to 5.59 for the selected shots, in order to find a critical area, like the work done in the tokamaks (see 2.1 for

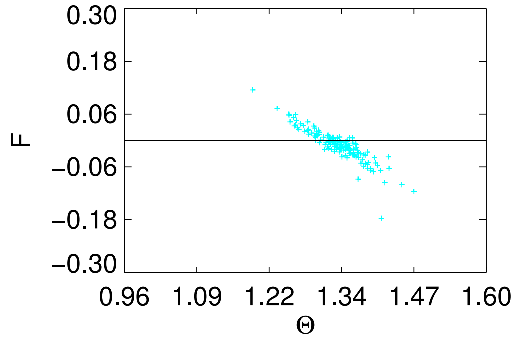

Figure 5.50: Plot of F versus Θ at the end of the CQ.

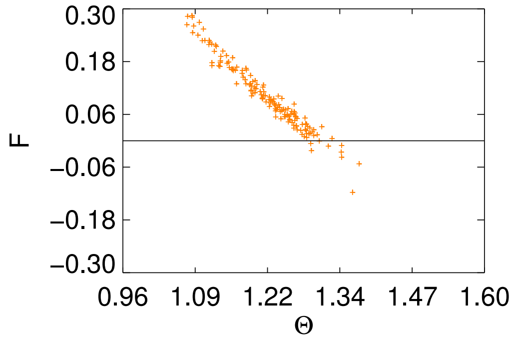

Figure 5.51: Plot of F versus Θ at the CQ start.

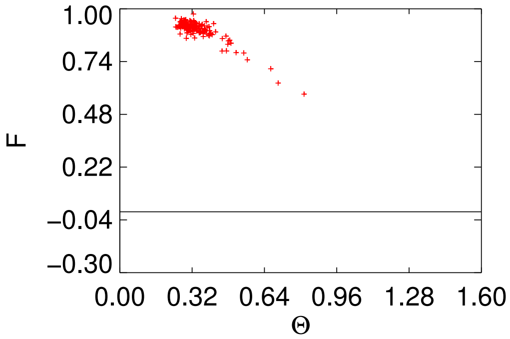

Figure 5.52: Plot of F versus Θ at the CQ end.

further informations) and the zones that, in average, were covered. As it can be seen, the points seem to display always in between an hyperbole in the first and in the third quadrant (where the Murakami parameter and q_a have the same sign, as it should be because $q_a \propto B_\phi(a)$) and the parameters of this hyperbole seems to change during the evolution of the discharge. This hyperbole is the equivalent of the horizontal line in the Hugill plot for the tokamak (figure 2.1). Except for the pre TQ time, the points tend to dispose in the third quadrant, where q_a is negative, and to spread in the space. At the end of the disruption, all the points are located in the first quadrant but are not extremely spread over the x-axis, thus they tend to have the same Murakami parameter at the end of the discharge, flattened around the 0. This can be explained by the fact that q_a highly grows when the poloidal field becomes low and this occurs at the end of the discharge.

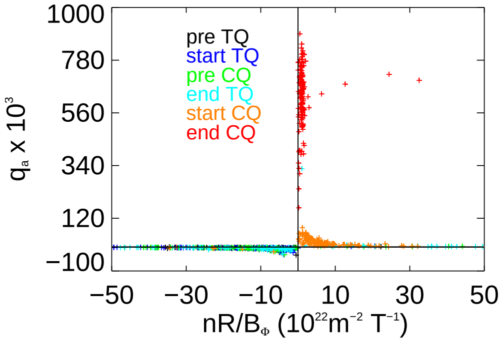

Figure 5.53: Hugill plot for the shot considered at all the times used.

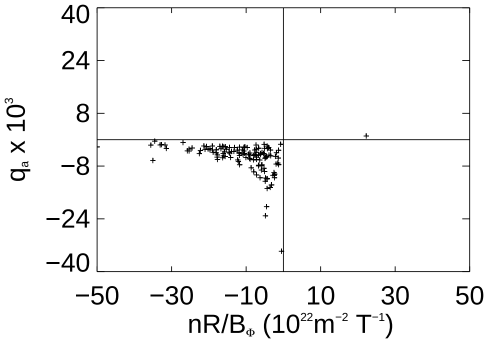

Figure 5.54: Hugill plot before the CQ.

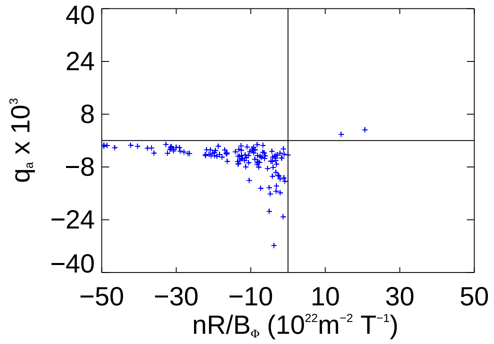

Figure 5.55: Hugill plot at the beginning of the TQ.

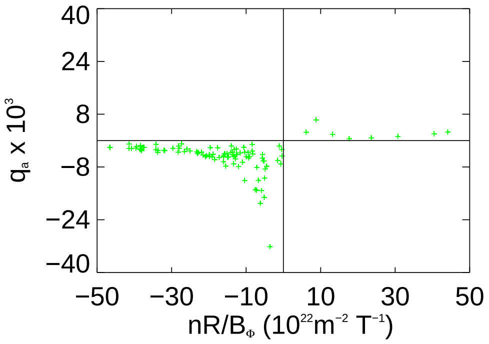

Figure 5.56: Hugill plot before the CQ.

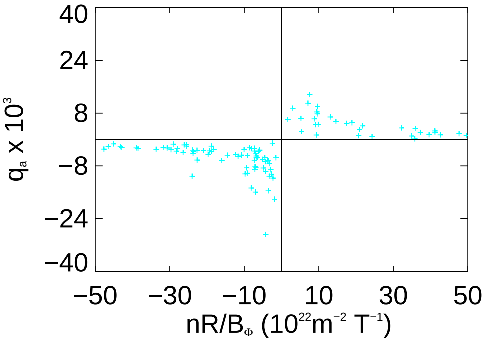

Figure 5.57: Hugill plot at the ending of the TQ.

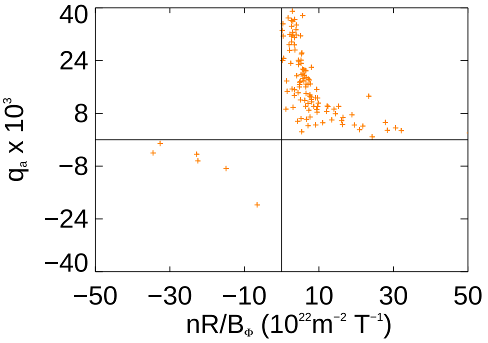

Figure 5.58: Hugill plot at the beginning of the CQ.

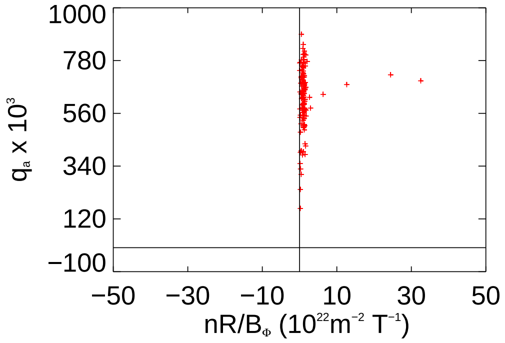

Figure 5.59: Hugill plot at the ending of the CQ.

5.4.5 Operational space (LP, n/n_G)

Now a study on the operational space (LP, n/n_G) is carried out, looking for some correlations between these two parameters. The idea of studying this space is that the locking of the modes at a particular position can create macroscopic deformations in the plasma, which can collide with the wall thus generating high heat loads and removing particles from the wall. In figure 5.60 we can see the distribution of all the points in the space. Apart from the populated regions below $72\,°$ and above $216\,°$, the points seem to equally cover the toroidal angles. In the discrete times plot, from figure 5.61 to 5.66, we see that this preferential distribution shows itself all over the disruption evolution. A particular look should be taken at the end of the CQ (figure 5.66), with the peaking at position $40\,°$, as already seen. Apart from the growth of the density from the pre TQ, during the disruptions the density seems not to vary much and thus a relation between the locking position and the normalised density is hard to see.

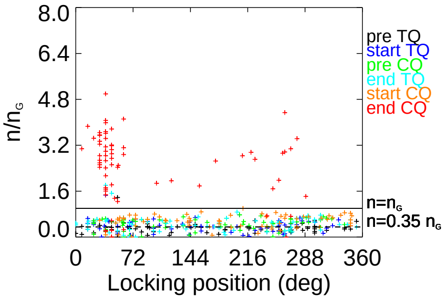

Figure 5.60: Normalised density versus LP at all the times considered.

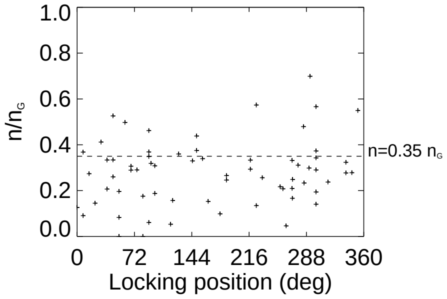

Figure 5.61: Normalised density versus LP at the pre TQ.

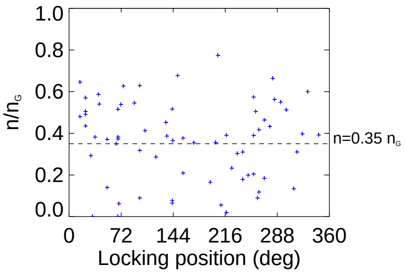

Figure 5.62: Normalised density versus LP at the TQ start.

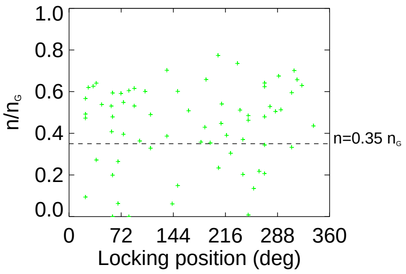

Figure 5.63: Normalised density versus LP at the pre CQ time.

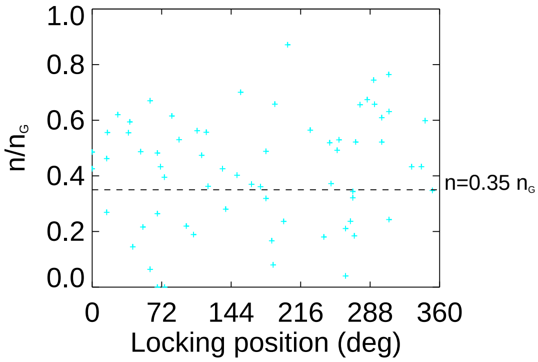

Figure 5.64: Normalised density versus LP at the end of the TQ.

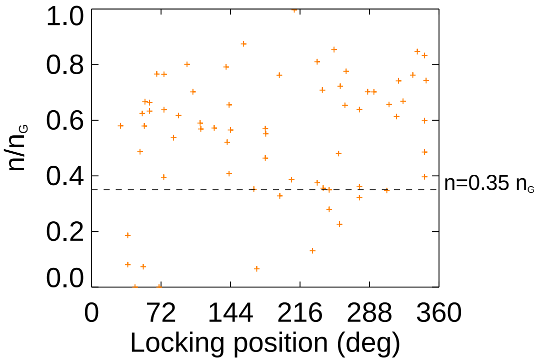

Figure 5.65: Normalised density versus LP at the CQ start.

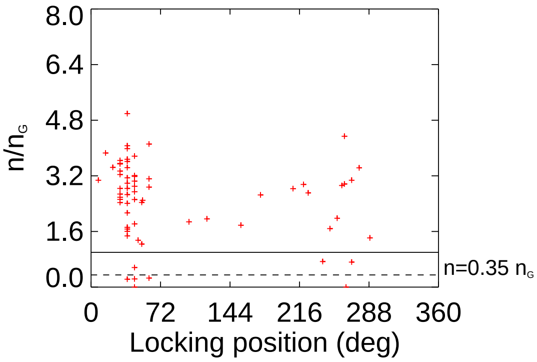

Figure 5.66: Normalised density versus LP at the CQ end.

5.4.6 Operational space (α,Θ_0)

Lastly, the operational space in terms of α and Θ_0 is displayed. As it can be seen from figures 5.67 to 5.72, the points don't seem to spread too much in this space at the beginning of the disruption (figures 5.68, 5.69, 5.70) where the α parameter is contained between the values of 4 and 16, but after the end of the TQ (starting from figure 5.71), the range of the α parameter broadens. This implies that the $\mathbf{j}$ and μ profile tends to become flatter during the development of the disruption.

It must be noted that the values are not present for the end TQ time. This is due to the fact that they were not useful, in fact the calculation of these parameters wasn't accurate and the points saturated or in the $\alpha = 100$ line or in the $\Theta_0 = 1$ line.

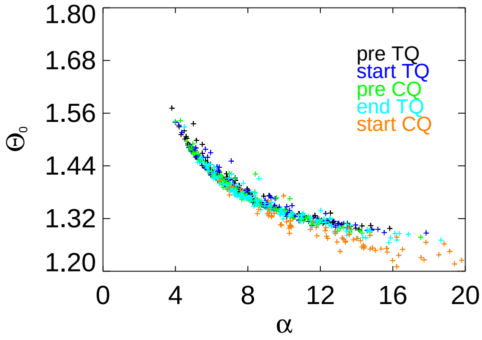

Figure 5.67: Plot in the (Θ_0,α) space for all the disruption length.

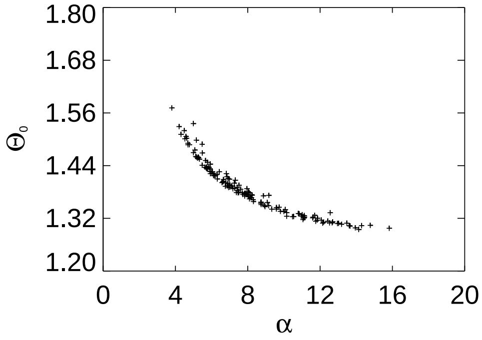

Figure 5.68: Plot in the (Θ_0,α) space before the TQ.

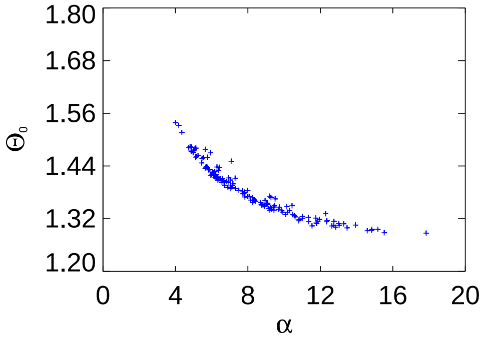

Figure 5.69: Plot in the (Θ_0,α) space at the start of the TQ.

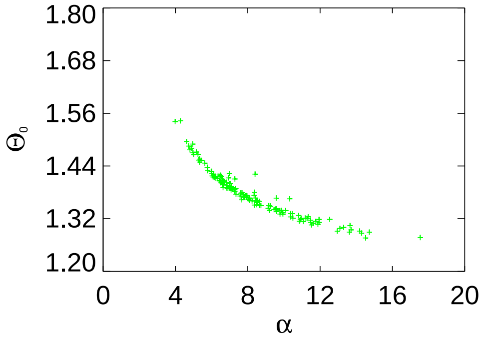

Figure 5.70: Plot in the (Θ_0,α) space before the CQ.

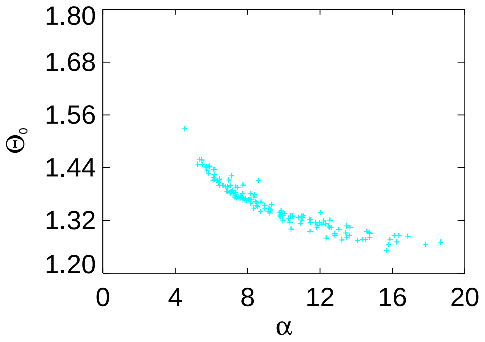

Figure 5.71: Plot in the (Θ_0,α) space at the end of the TQ.

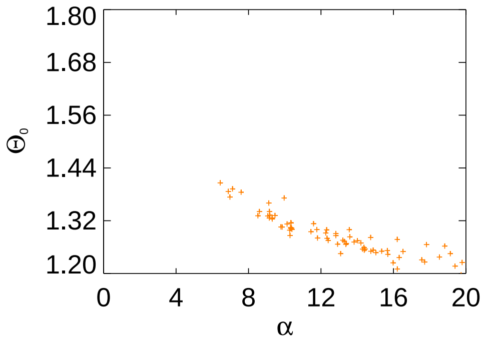

Figure 5.72: Plot in the (Θ_0,α) space at the start of the CQ.

5.5 Conclusion

In this chapter, a statistical study on the RFX-mod disruptions has been done, with particular attention to the magnetic modes behaviour and the parameters already analysed in Chapter 4.

At the beginning some statistic on the parameters presented in the previous chapter has been carried out. The frequency of the ratio I_{PD}/I_{max} and the frequency of the shot length for the database pulses has been done, finding that the discharges tend to peak over certain values.

In the second part, some correlations between different parameters have been done. The quench rate parameter has been compared to I_{PD}, finding a linear trend that confirms the fact that the inductance in the disruptive discharges is approximatively the same, also if some shots do not follow the same trend. The poloidal maximum voltage induced has been studied and compared to the quench rate, finding a linear distribution of the shots due to the constant inductance. In addition, the quench parameter has been compared to the ratio I_{PD}/I_{max} and in this study it is evident the boundaries over which the quench parameter lies. The correlation between the CQ and TQ times has been studied, finding that for the RFP the TQ time is usually shorter than the CQ time, in an opposite trend with respect to the tokamak disruptions.

The behaviour of the magnetic modes fluctuations have been studied for different current ranges and a change in the energy distribution of the modes have been found. In particular, for the $m = 0$ modes the energy increases with the discharge, reaching a maximum around the CQ end in the even modes. Also for the $m = 1$ modes a redistribution occurs during the disruption, with an increased normalised amplitude in the modes that don't contribute to the dynamo ($-7 < n < 0$) and a broadening of the magnetic spectrum all long the evolution of the phenomenon studied. Lastly the locking position of the modes has been analysed, finding that there is a preferred position of the locking only at the end of the CQ. The position is the one where an active coil is broken, thus the control of the amplitude of the modes is less effective.

In the last section the operational spaces studied for the single shots in the previous chapter have been analysed statistically. Some interesting trends that have been found, like the increasing of the density before the sign change of the F parameter and the strong change of the Θ parameter at the start of the CQ. The other trends found also in the single discharge studies have been confirmed, in particular the locking of the modes at the end of the CQ in a preferred position and the increasing of the α parameter during the disruption evolution.

6

Halo current analysis

The study of halo currents during disruptions is an interesting and challenging topic, as explained in Chapter 2. Their presence during a disruption in the tokamak is known if the plasma moves from its equilibrium position and it is useful to confirm and amplify the work done on this phenomenology in RFX, as already carried out in [56] and [57]. In the following chapter, the relation between the halo current maximum value and their poloidal distribution is investigated and, in addiction, their relation with the locking position of the modes is studied. Lastly, the relation between the halo fraction and the toroidal peaking factor is studied.

6.1 Halo measurements in RFX-mod

In the following chapter, only the voltage measurements will be considered. This is done because, by assuming a specific path in the passive structure (and consequently a resistance associated to it) it is then possible to estimate the current flowing from the plasma to the structures and vice-versa.

In figure 6.1 the signals flowing out from the sensors at a fixed toroidal position dedicated to measure the halo currents are displayed. In order to measure the poloidal distribution of the halo currents, a ring of sensors subdivided in eight sectors is used (we shall call this ensemble of sensors *discrete ring*). Since each sensor is influenced by the magnetic flux variations, also the induced currents due to the current quench are measured. In order to evaluate the contribution of the halo currents to the total measurements, the following procedure has been used: for each toroidal position, the average of the eight sensors has been evaluated and then the difference between the single measurements and the average has been used as the signal to analyse.

$$v_i(t) = V_i(t) - \sum_{i=1}^{8} \frac{V_i(t)}{8} \qquad i = 1, \ldots, 8 \tag{6.1}$$

where $v_i(i)$ is the signal used for the analysis and $V_i(t)$ the signal from the sensor. In figure 6.2 the signals $v_i(t)$ can be seen.

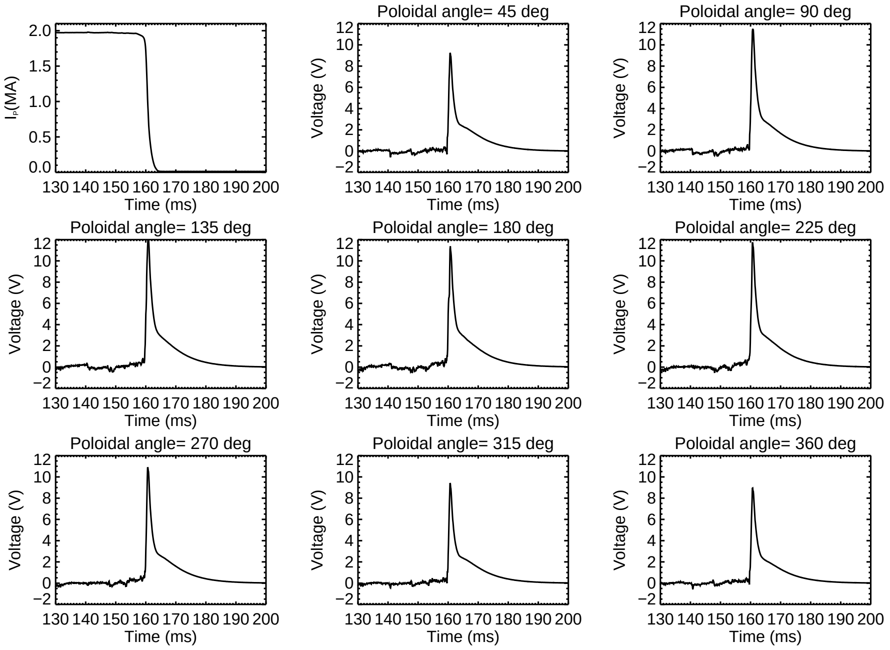

Figure 6.1: Temporal evolution of halo sensor signals. Shot 28906, toroidal position: $30\,°$

6.2 Poloidal distribution of the halo maxima

At a fixed toroidal position, it is interesting to evaluate if the halo currents tend to dispose in particular poloidal sectors, in order to see whether there are some preferred positions where the plasma intersects the wall. Since only eight sensors are available, our analysis is limited to these poloidal angles. For each shot and for each toroidal position, the absolute maximum is found and its position is determined. In figures 6.3, 6.4, 6.5 and 6.6, each data point corresponds to a shot, with the black color used for the positive maxima and the red used for the negative ones. The apparent anisotropy seen in figures 6.3 and 6.4 can be explained because of the fact that some sensors in those poloidal positions are broken, thus the preferential

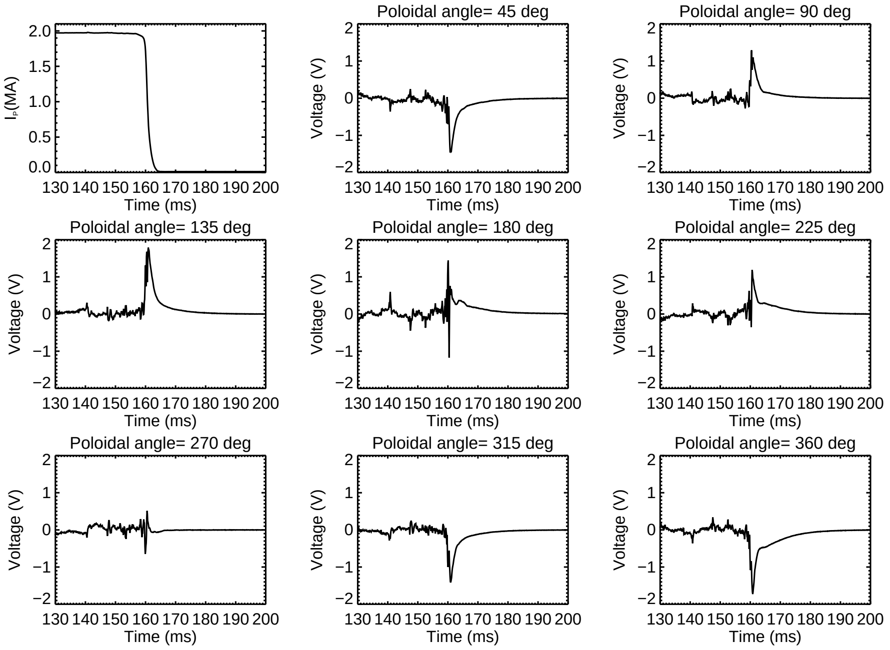

Figure 6.2: Temporal evolution of the differences between the signals and the average. Shot 28906, toroidal position: $30\,^\circ$

poloidal position has not to be considered as a particular distribution of the halo currents. All the halo currents plot below don't seem to show a preferred poloidal position.

6.3 Position of the halo maxima with respect to the LP

In this section, the position of the halo maxima is studied, compared to the relative angle of the locking. This last quantity is the difference between the toroidal position of the sensor and the LP, evaluated at the time of the maximum. In all the figures (from 6.7 to 6.10), the locking can be located at the same toroidal position (between $30\,^\circ$ and $40\,^\circ$) and from this it can be inferred that the halo currents don't have only a poloidal component, but also a toroidal one. In fact, if the current were only poloidal, the furthest toroidal positions from the locking wouldn't have an electric signal of the halo currents.

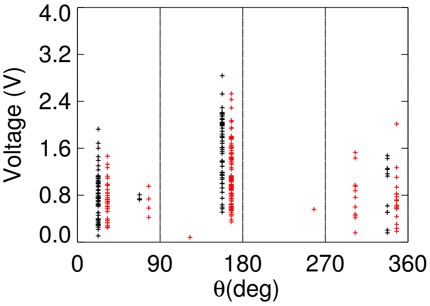

Figure 6.3: Poloidal distribution of the halo current maxima and minima at toroidal position of $25°$

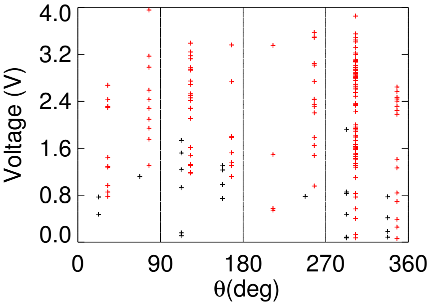

Figure 6.4: Poloidal distribution of the halo current maxima at toroidal position of $115°$

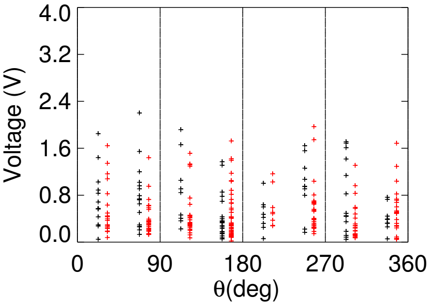

Figure 6.5: Poloidal distribution of the halo current maxima at toroidal position of $145°$

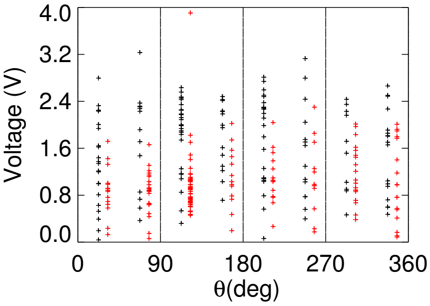

Figure 6.6: Poloidal distribution of the halo current maxima at toroidal position of $205°$

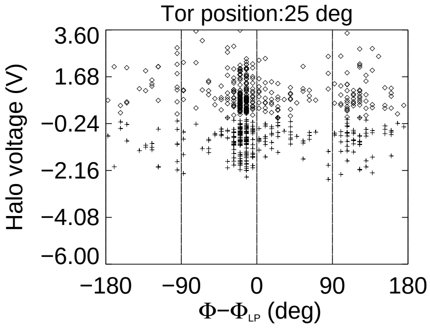

Figure 6.7: Relative angle of the halo current maxima with respect to the LP at toroidal position of $25°$

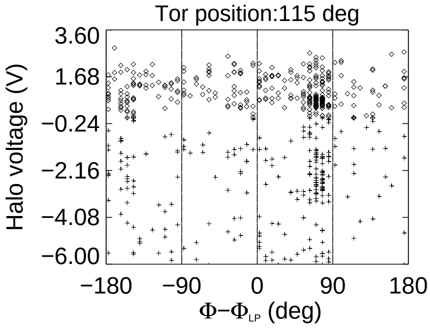

Figure 6.8: Relative angle of the halo current maxima with respect to the LP at toroidal position of $115°$

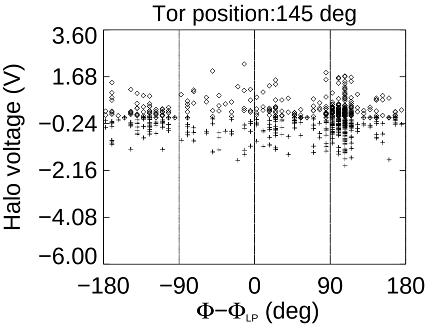

Figure 6.9: Relative angle of the halo current maxima with respect to the LP at toroidal position of 145°

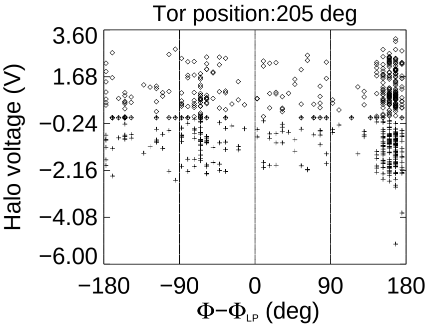

Figure 6.10: Relative angle of the halo current maxima with respect to the LP at toroidal position of 205°

6.4 Toroidal peaking factor and halo fraction

Two quantities that are interesting in the study of the halo currents are the halo fraction and the toroidal peaking factor. As an example over the studies of the halo currents, [55] is taken. The halo fraction ($\mathrm{f_{halo}}$) is the portion of the plasma current being converted to the halo currents. It is calculated as follows:

$$\mathrm{f_{halo}} = \frac{\max I_{halo}(i,j)}{\mathrm{I_{PD}}} \tag{6.2}$$

where I_{halo} is the halo current flowing in the sensor labelled by position (i, j). A strong assumption has been made in calculating this current: it was assumed that the current path was only in the poloidal direction and only in the sensor. This assumption is not necessarily always verified, in fact we have seen from the section before that the current path can have also a toroidal component. Nevertheless, the results presented are a good approximation of the behaviour of the halo currents. The toroidal peaking factor (TPF) is an indication of the toroidal distribution of the halo currents. This is an interesting aspect to consider, in fact an asymmetry in the toroidal current can result in asymmetric mechanical stresses and thus in possible harm for the device. It is defined as follows:

$$\mathrm{TPF} = 1 + \frac{\max_j(I_{halo}(t,j) - \frac{1}{n}\sum_{i=1}^{n} I_{halo}(t,j))}{\frac{1}{n}\sum_{i=1}^{n} I_{halo}(t,j)} \tag{6.3}$$

where $I_{halo}(t, j)$ is the current at the time of the maximum (here indicated as t) at the toroidal position j.

As figure 6.11 shows, the data points in the (f_{halo},TPF) space lie in between an hyperbole in the form $y = 0.15/x$ but the large majority of the points lies in a smaller area, within the hyperbole $y = 0.05/x$. In the plot, the TPF is shown for each poloidal position in different colours and it can be seen that the halo fraction of a single discharge doesn't vary much with the poloidal angle.

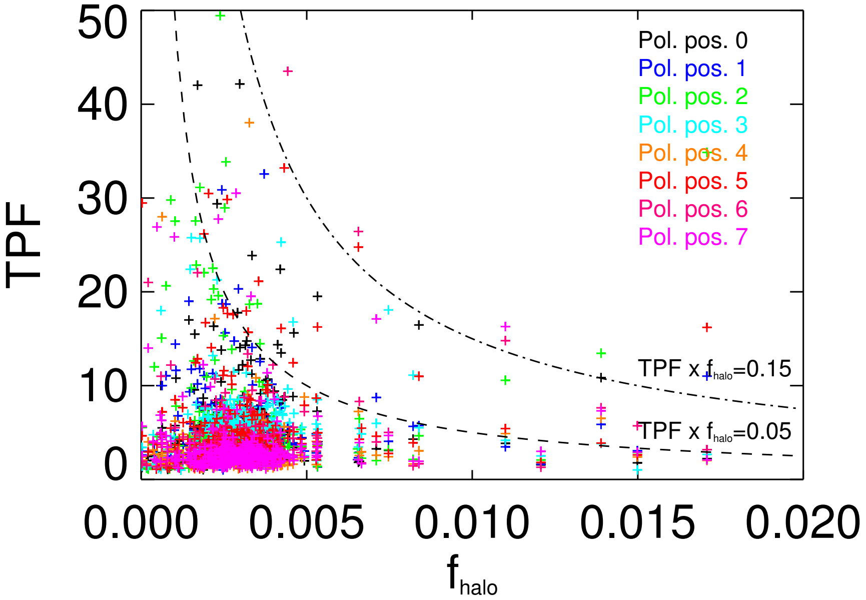

Figure 6.11: Plot of the Toroidal Peaking Factor (TPF) versus the halo fraction f_{halo} for the RFX-mod RFP discharges.

6.5 Conclusion

In this chapter, a preliminary study on the halo currents in RFX-mod has been carried out.

An asymmetry in the poloidal distribution of the halo maxima has not been seen, although some data weren't available due to the lack of some measurements in the toroidal positions $25\,°$ and $115\,°$.

In the second part, the correlation between the halo maxima position and the LP has been evaluated and the results suggest that the halo currents don't flow only in the poloidal position, but also in the toroidal one, since the four toroidal position are in agreement with each other in the high accumulation of the data around the LP.

In the last section, a study of $\mathrm{f_{halo}}$ and the TPF has been carried out and, for the cases studied, it seems that the experimental points lie within an hyperbole and thus a limit in the value $\mathrm{f_{halo}} \times \mathrm{TPF}$ is recovered, as in the tokamak case.

Conclusions and future developments

In this thesis, the operational limits and the disruptions of the Reversed Field Pinch configuration have been for the first time systematically analysed. Disruptions in such type of devices have been seen previously but never studied as in the tokamak configuration, although some similarities between this phenomenology and the RFP dynamics can be recognised.

A methodology to identify RFP disruptions over the large shot database has been developed. The disruption is characterised by a sudden loss of the current and the rapidity over which this current quench occurs has been used to determine whether a shot was disruptive. Filtering the shots was necessary and it has been done using several discharge parameters. In order to avoid the inclusion of the tokamak discharges, a lower limit has been used for the maximum current: the tokamak discharges have a maximum current around $200\,\mathrm{kA}$, thus the RFP disruptions found have a current higher than $300\,\mathrm{kA}$ in a way to be sure to avoid the tokamak pulses. Another filter used was a lower limit on the poloidal voltage induced in the sensors during the quench of the current, in fact the lower this value is, the slower the current quench is. Using this methodology, a total of more than 300 disruptive shots has been found.

The main parameters used in the disruption characterisation have been presented: the quench rate is a measure of the derivative of the current during the quench and the higher this value is the stronger the disruption has been. The time over which the thermal energy is lost has been measured. A quantity that is often used in the characterisation of a tokamak disruption is the current before the quench, and for this analysis it has also been manually evaluated for each shot. A set of six time instants for each discharge has been found, in order to do a comparison between the discharge at different times that corresponds to different plasma conditions.

The problems encountered in doing an automatic analysis have also been presented. A disruption is a fast and sudden critic event that produces high thermal loads and mechanical stresses. These effects can be a problem, in particular for the temperature and the density diagnostics. The former detects the soft x-rays radiation of the plasma and during a disruption this light can be extremely intense and cause saturation, while the latter is highly sensible to the mechanical alignment that can be lost due to the mechanical stresses on the vessel, and this loss causes fringe jumps and hence meaningless density measurements. In addiction, for some shot ranges the diagnostics were unavailable and thus the data couldn't be retrieved. Apart from these diagnostic problems, sometimes there were some behaviours of the plasma that made the thermal quench impossible to define. All these problems have been taken in consideration during the data analysis, that has been done manually for the determination of the thermal quench.

A study of some shots selected as references for the RFP disruptions have been studied before going further with the statistical analysis. This operation was necessary in order to understand whether the parameters analysed are useful for the study of RFP disruptions. These shots have been chosen for their peculiar features, like the current ranges, the MHD instabilities developed before the disruption and the velocity over which a disruption was born and spoiled the confinement. The main plasma parameters have been observed during their temporal evolution and some operational spaces have been investigated in order to find if there are some ranges harmful for the discharge. Some common trends have been seen among the discharges: the density tends to rise before the beginning of the disruption, the reversal of the field is usually lost at the beginning of the current quench and the α parameter, related to the size of the current channel, tends to increase during the development of the disruption. The trends seen in the various discharges confirm that the parameters selected are useful for the characterisation of RFP disruptions.

A statistical study on the database obtained has been done, looking for some common behaviour all over the RFP disruptive shots. For this first part, the discharges were subdivided in two groups: the ones with the intervention of the protection system of RFX-mod and the ones without it. The frequency of the maximum plasma current was peaked around two points: $0.6\,\mathrm{MA}$ and $1.3\,\mathrm{MA}$ The frequency of the ratio between the current before the disruption and the maximum plasma current has been studied, finding that below the value of $60\,\%\,I_{max}$ no disruptions occurs and a peaking of the shots around the value of $90\,\%\,I_{max}$ is found for the two discharge sets used. Similarly, the frequency of the shot time length has been evaluated, finding that the majority of the shots had a disruption between $20\,\mathrm{ms}$ and $150\,\mathrm{ms}$ (largely before the maximum length for a RFX-mod shot, which is around

$500\,\mathrm{ms}$ at maximum) and a small number of discharges interrupted at around $320\,\mathrm{ms}$.

Some correlations between the current quench parameter, the thermal quench parameter and the poloidal voltage have been studied. Analysing the quench rate as function of I_{PD}, the selected shots displayed for the majority over a line. The same trend is seen in the correlation between the poloidal voltage induced and the quench rate. For this work, the shots that followed a different trend(thus have a different inductance) have been excluded from the analysis. The quench parameter has been studied against the ratio I_{PD}/I_{max}, finding an upper and a lower limit in the data plot, which imply an upper and a lower limit in the time of the current quench: the first has been set during the database creation, the last is a consequence of the fact that the current can't quench in times excessively short. An interesting trend has been found in the correlation between the thermal quench time and the current quench time: the former is usually longer than the latter, in opposition with the trend found for the tokamak.

The behaviour of the magnetic mode fluctuations has been analysed over the development of the disruption for different current ranges. Both for the $m = 0$ and $m = 1$ modes, the amplitude increases with the development of the disruption. Considering the modes with toroidal number $m = 0$, the highest normalised amplitude belong to the fluctuations with even n number, while in the case of $m = 1$ the modes with poloidal number $-6 < n < 0$ tend to increase, reaching the normalised amplitudes of the $n = -7$ mode, the one most present in the dynamo action. During the evolution of the disruption, the spectral width of the $m = 1$ fluctuations constantly increases. No relevant trend is seen comparing the position of the locking modes with I_{PD}, but at the end of the thermal quench a preferred position of the locking modes is found, near the toroidal angle where the active control system has a broken coil and thus it is less effective.

The operational spaces used for the study of the single discharges are used also for the statistical study. For the database used, the RFP configuration is lost at the beginning of the current quench for almost the totality of the database pulses. Before the loss of the reversal, the density usually increases up to 0.8 the Greenwald density. The Θ parameter is seen to remain in the same range explored before the start of the current quench but then a large variation occurs and this is confirmed both by the (F,Θ) operational space and the (q_a,F) space, where the linear dependence between the two quantities is lost at the beginning of the current quench for the highest values of F. The pseudo-Hugill plot of the discharges shows that the parameters lie within an hyperbole (representing the density limit) and at the end of the current quench the edge toroidal magnetic field is so high that all the values accumulates on the positive side of the y-axis. A strong increase in the density as a function of the modes locking position has not been found. Lastly, the trend seen in the (α,Θ_0) operational space confirms that the plasma current channel usually tends to enlarge with the evolution of the disruption.

A study on the RFX-mod halo currents caused by a disruption has been carried out. The poloidal maximum positions has been studied in order to find whether some poloidal positions are preferred, but the maxima seem to dispose uniformly in the poloidal space. The halo currents seem to follow also a toroidal path inside the vessel, because the position of the mode locking can be retrieved by all the toroidal positions where the halo currents were measured, thus they should have also gone in a toroidal way. Lastly, the toroidal peaking factor and the halo fractions have been analysed, finding bigger peaking factors compared to the tokamak usual values but a similar limit in the product of these two parameters.

This thesis opens the way for many complementary studies that can be done in the field of RFP disruptions. First of all, the causes that lead to the increase of the density or to the loss of the thermal content should be found, in order to create a set of operational limits similar to the ones for the tokamak. Found this set of operational limits, some methods to avoid or mitigate the disruptions can be developed.

An interesting physical aspect that can be studied is the dynamics of the relaxation event that leads to a disruption and the differences with the relaxation events necessary for the RFP self-sustainment.

Given the high flexibility of the RFX-mod device, comparisons between RFP disruptions and tokamak disruptions can be done and this could evidence the differences and similarities between these two phenomena in the different configurations. The relaxation and reconnection events that characterise the RFP disruption could be compared to the relaxation that happens in a tokamak disruption, thus helping a deeper understanding of the physics behind this phenomenon.

Bibliography

[1] J. Freidberg, *Plasma Physics and Fusion Energy*, Cambridge University Press (2007)

[2] J.A. Wesson, *Tokamaks*, Clarendon Press-Oxford (2004)

[3] `http://fusionwiki.ciemat.es/wiki/Main_Page`

[4] M. Kikuchi, K. Lackner and M. Tran (edited by), *Fusion Physics*, IAEA (2012)

[5] M.D.Kruskal et al., *Hydromagnetic Instability in a Stellarator*, Phys.Fluids **1**(1958)

[6] V.D.Shafranov, *The stability of a cylindrical gaseous conductor in a magnetic field*, At. Energy **1** (1956)

[7] I.B. Bernstein et al., *An Energy Principle for Hydromagnetic Stability Problems*, Proc. Roy. Soc. London, A **244**, issue 1236 (1958)

[8] S. Ortolani, D. D. Schnack, *Maghetohydrodynamics of plasma relaxation*, World Scientific Publishing (1993)

[9] L. Woltjer, *A theorem on force-free magnetic fields*, Proc. Natl. Acad. Sci. USA **44**, p.489 (1958)

[10] J. P. Freidberg, *Ideal Magnetohydrodynamics*, Plenum Press, New York (1987)

[11] J.B. Taylor, *Relaxation and magnetic reconnection in plasmas*, Rev. of Modern Physics **58** (1986)

[12] H. Zohm, *Magnetohydrodynamic Stability of Tokamaks*, Wiley (2014)

[13] T. Bolzonella, D. Terranova, *Magnetic fluctuation spectra and non-linear MHD mode interaction in RFX*, Plasma Phys. Control. Fusion **44** (2002) 2569–2581

[14] M. Valisa et al, *Locked modes induced plasma-wall interactions in RFX*, J. Nucl. Mater. **988**, (1997) 241–243

[15] P. Zanca, S. Martini, *Reconstruction of the plasma surface in a RFP in the presence of non-axisymmetric perturbations*, Plasma Phys. Control. Fusion **41** (1999) 1251–75

[16] V. Antoni et al., *MHD stability analysis of force-free reversed field pinch configurations*, Nucl. Fusion **26** (1986)

[17] R. Lorenzini et al., *Self-organized helical equilibria as a new paradigm for ohmically heated fusion plasmas*, Nature Physics **5**, 570-574 (2009)

[18] D. F. Escande et al., *Quasi-Single-Helicity Reversed-Field-Pinch Plasmas*, Phys. Rev. Lett. **85**, issue 1662 (2000)

[19] P. Martin et al., *Quasi-single helicity states in the reversed field pinch: Beyond the standard paradigm*, Physics of plasmas **7** (2000)

[20] Y. L. Ho, G. G. Craddock, *Non-linear dynamics of field maintenance and quasi-periodic relaxation in reversed field pinches*, Physics of Fluids B **3** (1991)

[21] M. Zuin et al., *Current sheets during spontaneous reconnection in a current-carrying fusion plasma*, Plasma Phys. Control. Fusion **51** (2009)

[22] C. Piron, *Study of magnetic reconnection events in fusion plasmas*, Thesis for the Master degree in Physics, University of Padova (2011)

[23] P. Sonato et al., *Machine modification for active MHD control in RFX*, Fusion Engineering and Design **66 - 68** (2003) 161-168

[24] `http://www.igi.cnr.it/`

[25] M. Greenwald et al., *A new look at density limits in tokamaks*, Nuclear Fusion **28** (1988) 2199–2207

[26] M. Greenwald, *Density limits in toroidal plasmas*, Plasma Phys. and Control. Fusion **44** (2002) R27–R80

[27] J. Wesson, *The science of JET* (2006)

[28] F. Troyon et al., *MHD limits to plasma confinement*, Plasma Phys. Controlled Fusion, **26** (1A) (1984)

[29] F. Troyon, R. Gruber, *A semi-empirical scaling law for the p limit in tokamaks*, Physics Letters **29** (1985)

[30] B. B. Kadomtsev, *Magnetic field line reconnection*, Rep. Prog. Phys. **50** (1987)

[31] ITER Physics Basis, Nucl. Fusion **39** (1999) 2137

[32] T. Hender et al., *Progress on the ITER Physics Basis: Chapter 3*, Nuclear Fusion **47** (2007) S128–S202

[33] C. Reux, *Etude d'une methode d'amortissement des disruptions d'un plasma de tokamak*, Plasma Physics Ecole Polytechnique X (2010)

[34] A. Thornton, *The impact of transient mitigation schemes on the MAST edge plasma*, University of York (2011)

[35] L.R. Baylor, *Disruption Mitigation System Design for ITER*,Theory and Simulation of Disruptions Workshop, (2014)

[36] S. Mirnov et al., *Phenomenology of major and minor disruptions in high beta deuterium and tritium tokamak fusion test reactor plasma*, Physics Of Plasmas **5**(1998) 3950–3960

[37] P. Zanca et al., *Feedback control model of the* $m = 2$, $n = 1$ *resistive wall mode in a circular plasma*, Plasma Phys. Controlled Fusion **54** (2012)

[38] J.A. Wesson, *Hydromagnetic stability of tokamaks*, Nucl. Fusion **18** (1978) 87–131

[39] P.C. de Vries et al., *Survey of disruption causes at JET*, Nucl. Fusion **51** (2011)

[40] G. Pautassio et al., *Disruption causes in ASDEX Upgrade*, 41^{st} EPS Conference on Plasma Physics

[41] B. Esposito et al. *Disruption control on FTU and ASDEX upgrade with ECRH* Nuclear Fusion, **49** (2009)

[42] R. Bartiromo et al., *Analysis of the high density limits in the RFX high current regimes*, 2000 Proc. 27th EPS Conf. on Controlled Fusion and Plasma Physics (Budapest, 2000) vol. **24B** (ECA) 1380–1383

[43] G. Spizzo et al., *Density limit studies in the tokamak and the reversed-field pinch*, Nucl. Fusion **55**(2015)

[44] P. Martin et al., *Soft x-ray and bolometric tomography in RFX*, Rev. Sci. Instrum. **68** (2) (1997)

[45] A. Murari et al., *An optimized multifoil soft x-ray spectrometer for the determination of the electron temperature with high time resolution*, Rev. Sci. Instrum. **70**, No. 1 (1999)

[46] A. Alfier, R. Pasqualotto, *New Thomson scattering diagnostic on RFX-mod*, Rev. of Sci. Instr. **78** (2007)

[47] T. P. Donaldson, *Theory of foil-absorption techniques for plasma x-ray continuum measurements*, Plasma Phys., **20** (1978)

[48] P. Innocente et al., *Development of the RFX* CO_2 *interferometer for extended edge resolution*, Rev. Sci. Instrum., **61** (10) (1990)

[49] P. Innocente et al., *Upgrade of the RFX* CO_2 *interferometer using in-vessel optics for extended edge resolution*, Rev. Sci. Instrum., **68** (1) (1997)

[50] D. Gregoratto et al., *Behaviour of electron density profiles and particle transport analysis in the RFX reversed field pinch*, Nucl. Fus., **38** (1998)

[51] N. Pomaro, F. Basso, *Transducers and signal conditioners of the RFX new magnetic measurement system*, Fusion Engineering and Design **74** (2005) 721–726

[52] P. Fiorentin, N. Pomaro, *Design of a new electromagnetic diagnostic for RFX*, Fusion Engineering and Design **66** (2003) 871-876

[53] A.V. Oppenheim, R.W. Schafer, *Digital Signal Processing*, Englewood Cliffts, Prentice Hall, New Jersey, (1975)

[54] S.P. Gerhardt et al., *Characterization of the plasma current quench during disruptions in the National Spherical Torus Experiment*, Nucl. Fusion **49** (2009)

[55] G. F. Counsell et al., *On the magnitude and distribution of halo currents during disruptions on MAST*, Plasma Phys. Control. Fusion **49** (2007) 435–446

[56] R. Bartiromo et al., *In vessel magnetic field measurements in RFX*, ICPP& 25th Conf. on Contr. FUsion and Plasma Physics, Praha, ECA **22C** (1998) 770-773

[57] P. Sonato et al., *Investigation of plasma facing components and vacuum vessel in RFX*, Journal of Nuclear Materials **241-243** (1997) 982-987